2020

Rational catalyst design for N2 reduction under ambient conditions: Strategies towards enhanced conversion efficiency

Lei Shi
Edith Cowan University

Yu Yin
Edith Cowan University

Shaobin Wang

Hongqi Sun
Edith Cowan University

Review

Rational Catalyst Design for N$_2$ Reduction under Ambient Conditions: Strategies toward Enhanced Conversion Efficiency

Lei Shi,* Yu Yin, Shaobin Wang, and Hongqi Sun*

Read Online

ACCESS | Metrics & More | Article Recommendations

ABSTRACT: Ammonia (NH$_3$), one of the basic chemicals in most fertilizers and a promising carbon-free energy storage carrier, is typically synthesized via the Haber−Bosch process with high energy consumption and massive emission of greenhouse gases. The photo/electrocatalytic nitrogen reduction reaction (NRR) under ambient conditions has attracted increasing interests recently, providing alternative routes to realize green NH$_3$ synthesis. Despite rapid advances achieved in this most attractive research field, the unsatisfactory conversion efficiency including a low NH$_3$ yield rate, and limited Faradaic efficiency or apparent quantum efficiency still remains as a great challenge. The NRR performance is intrinsically related to the electronic and surface structure of catalysts. Rational design and preparation of advanced catalysts are indispensable to improve the performance (e.g., activity and selectivity) of NRR. In this Review, various strategies for the development of desirable catalysts are comprehensively summarized, mainly containing the defect engineering, structural manipulation, crystallographic tailoring, and interface regulation. State-of-the-art heterogeneous NRR catalysts, prevailing theories and underlying catalytic mechanisms, together with current issues, critical challenges, and perspectives are discussed. It is highly expected that this Review will promote the understanding of recent advances in this area and stimulate greater interests for designing promising NRR catalysts in future.

KEYWORDS: nitrogen reduction, ammonia synthesis, catalyst design, electrocatalysis, photocatalysis
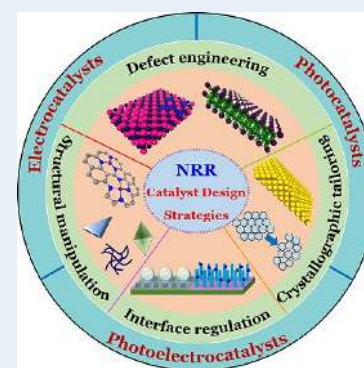
1. INTRODUCTION

Ammonia (NH$_3$) is one of the basic chemicals widely used in the agriculture, and in the chemical industry as an upstream reagent for producing value-added chemicals.[1] As a replacement of hydrogen (H$_2$), NH$_3$ containing 17.6 wt % H is also considered as an important hydrogen carrier that can be easily stored and transported compared with gaseous H$_2$. Particularly, serving as a carbon-free energy storage intermediate, the complete burning of NH$_3$ generates nitrogen (N$_2$) and water (H$_2$O), leading to no emission of harmful gases, like carbon monoxide (CO) and greenhouse gases, for instance, carbon dioxide (CO$_2$), into the atmosphere.

In nature, biological N$_2$ fixation occurs under ambient conditions (temperature and pressure) with the assistance of nitrogenase enzymes in certain bacteria. As key catalytic centers, the cofactors like FeMo, FeFe, and FeV in the enzymes are responsible for binding, activating, and reducing N$_2$, by consuming the energy from the adenosine triphosphate molecules.[2,3] Enlightened by this attractive process, several molecular catalysts have been reported to conduct N$_2$ reduction via multiple proton/electron-involved procedures.[4,5] However, the ultralow yield rate in the natural process could not satisfy the actual demands. Moreover, the poor stability and recycling issues of nitrogenase enzymes and molecular catalysts also restrict their large-scale applications.

Currently, the industrial production of NH$_3$ is mainly realized with the Haber−Bosch process, at high temperatures (300−600 °C) and pressures (150−300 atm).[6] This process accounts for 1−2% of the total global energy consumption. In addition to the heavy energy inputs, the used H$_2$ is primarily stemmed from the natural gas reforming, discharging millions of tons of CO$_2$ each year. Considering these energy and environment costs, it is desirable to develop alternative processes to achieve highly efficient N$_2$ reduction for NH$_3$ synthesis.[7]

In the past few years, emerging photo/electrocatalytic reduction processes have received enormous interests to directly synthesize NH$_3$ from N$_2$ and H$_2$O at ambient conditions.[8,9] These fascinating catalytic procedures possess many advantages, for example, mild reaction conditions, simple infrastructures, less environmental pollutions, and renewable energy consumptions from solar energy or electrical energy provided by solar cells and wind turbines.
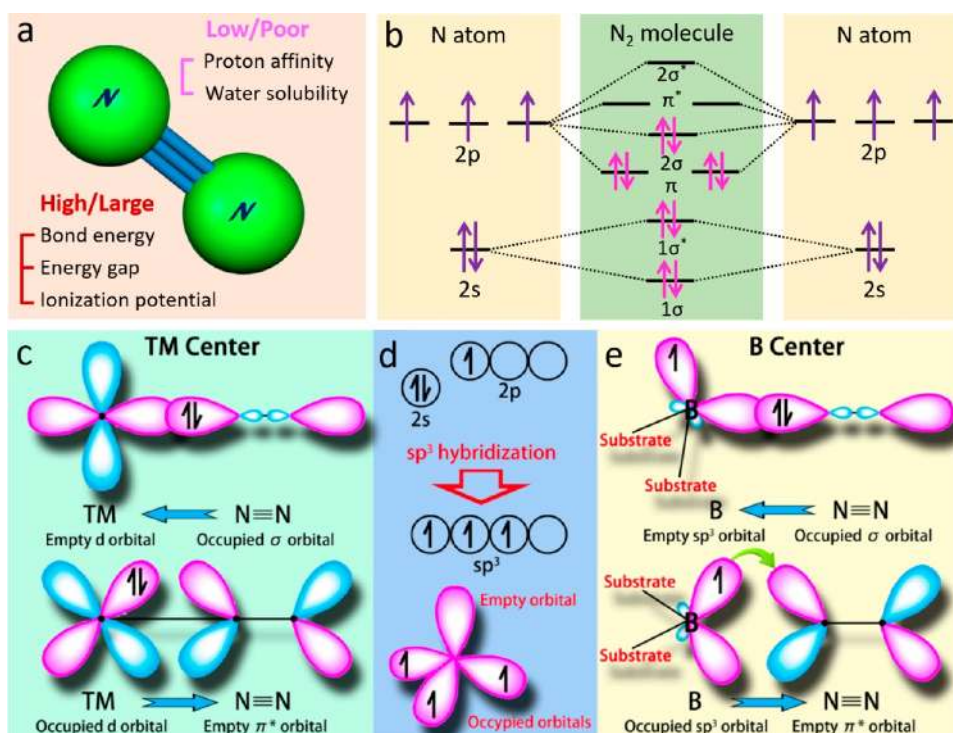
Figure 1. (a) Molecular structure of N_2. (b) Schematics of N atomic orbitals and N_2 molecular orbitals. (c) Simplified schematic of N_2 bonding to TMs. (d) Electronic configuration of pure B atom and B atom with sp^3 hybridization. (e) N_2 binding motifs to the B atom on the substrate. Reproduced with permission from ref 12. Copyright 2018 American Chemical Society.

Table 1. Applied Potentials of Hydrogenation Reactions Related to the NRR[a]

	reaction equilibrium	$E°$/V
R1	$N_2 + 6H^+ + 6e^- \leftrightarrow 2NH_3$	+0.55 vs NHE (pH 0)
R2	$2H^+ + 2e^- \leftrightarrow H_2$	0 vs SHE (pH 0)
R3	$N_2 + 6H_2O + 6e^- \leftrightarrow 2NH_3 + 6OH^-$	−0.736 vs SHE (pH 14)
R4	$2H_2O + 2e^- \leftrightarrow H_2 + 2OH^-$	−0.828 vs SHE (pH 14)
R5	$N_2 + e^- \leftrightarrow N_2^-$	−4.20 vs NHE or −3.37 vs RHE (pH 14)
R6	$N_2 + H^+ + e^- \leftrightarrow N_2H$	−3.20 vs RHE
R7	$N_2 + 2H^+ + 2e^- \leftrightarrow N_2H_2$	−1.10 vs RHE
R8	$N_2 + 4H^+ + 4e^- \leftrightarrow N_2H_4$	−0.36 vs RHE

[a]NHE: normal hydrogen electrode; SHE: standard hydrogen electrode; RHE: reversible hydrogen electrode.

2. PRINCIPLES AND CHALLENGES IN NITROGEN REDUCTION REACTION (NRR)

2.1. Thermodynamics of NRR. The N_2 molecule consists of two linearly combined N atoms (Figure 1a). Each N atom has a pair of electrons located in the 2s orbital with the opposite spin direction and three lone-pair electrons dispersed in 2p orbitals with same spin direction (Figure 1b). After the hybridization of atomic orbitals, new bonding orbitals (σ and π orbitals) and antibonding orbitals (σ^* and π^* orbitals) are generated, with the shared electrons in π and 2σ orbitals to form a highly intensive triple bond (N≡N). Attributed to the intrinsically inert properties of N_2, its cleavage and reduction at ambient conditions are confronted with several challenges. For example, (i) the N_2 molecule has a high bond energy of 941 kJ mol^{-1}, and the thermodynamically strong cleavage energy (410 kJ mol^{-1}) of the first bond demonstrates the critical challenge in the N≡N dissociation; (ii) the first-H addition process with N_2 is endothermic ($\Delta H^0 = 37.6$ kJ mol^{-1}), revealing that direct protonation process is forbidden in the thermodynamics; (iii)

the negative electron affinity (−1.9 eV), as well as a high ionization potential (15.85 eV) of N_2 molecule reduces its reactivity; and (iv) even in view of kinetics, the large energy gap (∼10.82 eV) between its highest occupied molecular orbital (HOMO) and lowest unoccupied molecular orbital (LUMO) is not favorable for electron transfer.[10,11]

The primary challenges in the catalytic NRR can be further disclosed from the thermodynamic constraints arising from the intermediates. The hydrogenation processes involved in the NRR and the related equilibrium potentials are provided in Table 1.[13,14] Obviously, these unfavorable potentials for the intermediate reactions clarify the thermodynamic difficulty for N_2 hydrogenation.

2.2. N_2 Molecule Chemisorption and Activation. It is well-known that the chemisorption of N_2 molecules onto the active centers and the subsequent activation with receiving electron from the catalysts are considered as prerequisite steps for NRR. Traditional transition metals (TMs, e.g., Fe, Mo, and Ti) have been theoretically predicted to strongly interact with
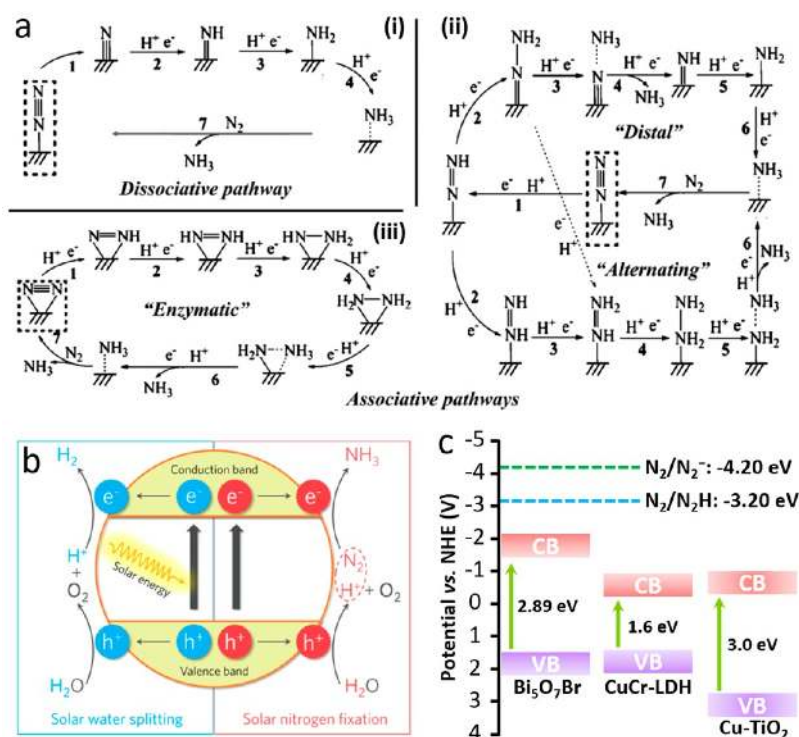
Figure 2. Figure 2. (a) Schematic illustrations of the dissociative and associative pathways (including distal, alternating, and enzymatic pathways) for NRR. Reproduced with permission from ref 11. Copyright 2018 Wiley-VCH Verlag GmbH & Co. KGaA, Weinheim. (b) Schematic diagram of the photocatalytic H_2O splitting and NH_3 synthesis. Reproduced with permission from ref 21. Copyright 2017 American Chemical Society. (c) Electronic energy-level diagram of typical photocatalysts, e.g., Bi_5O_7Br,[22] CuCr-LDH,[23] and Cu-TiO_2,[24] employed for the photocatalytic NH_3 synthesis.

N_2 via the formation of N—metal bonds, thanks to their advantageous coupling of empty and occupied d orbitals.[15,16] The empty d orbitals in the TMs could receive the lone-pair electrons of N_2, and the separated electrons in TM atoms would be donated into the antibinding orbital (π back-donation), forming an "acceptance-donation" route for the electron transfer to weaken the N≡N bond (Figure 1c).[12] As for the main-group compounds, the combination of empty and filled orbitals is generally absent to form bonds of σ and π symmetry, leading to the difficult π back-bonding. Interestingly, the nonmetal B-based molecular catalyst showed a strong interaction with N_2 following a similar "acceptance-donation" route.[17] The empty sp^2-orbitals of B atoms received the σ-orbital electrons of N_2, while the occupied p-orbitals donated the electrons back into the unoccupied π^*-orbitals of N_2. Moreover, the B atom with sp^3 hybridization also contained half occupied and empty orbitals, holding a great potential for N_2 reduction (Figure 1d). Once the B atoms were decorated into graphitic carbon nitride (g-C_3N_4) via the formation of two N—B bonds, one occupied and one empty sp^3 were generated for a strong interaction with N_2 molecules (Figure 1e). These investigations have shed light on the development of promising NRR catalysts (e.g., TM- or p-block nonmetal based catalysts) with high affinity toward N_2.

2.3. Electrocatalytic Pathways and Challenges.

Following the initial N_2 chemisorption and activation steps, the subsequent reactions involve multiple complicated electron transfer and hydrogenation procedures. Generally, the proposed pathways for electrocatalytic NRR are classified into two categories: the dissociative and associative pathways (Figure 2a).[11] According to the dissociative mechanism
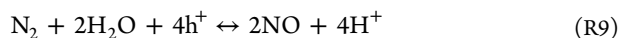
(pathway i), the N≡N bonds are broken first, and isolated N atoms on the catalyst surface will be converted into NH_3 via the hydrogenation reaction. The industrial Haber—Bosch reaction usually follows the dissociative pathway, and that is why harsh conditions are required to drive this process. As for the associative pathways (pathway ii), it can be further divided into alternating pathway and distal pathway on account of the distinct hydrogenation sequences. For the associative alternating pathway, the two N atoms react with protons simultaneously, which might result in the formation of byproducts (e.g., N_2H_4). In the distal pathway, the terminal N atoms preferentially participate in the hydrogenation reaction, and the addition of protons at the surface N atoms occurs once the remote NH_3 molecule is released. Following this pathway, only NH_3 is produced, and no other byproducts will be observed. In addition, there is another associative pathway, that is, the enzymatic pathway (pathway iii), during which both N atoms are anchored on the catalyst surface with a side-on mode.

Recently, an emerging pathway following the Mars—van Krevelen (MvK) mechanism was proposed for transition metal nitrides (TMNs, e.g., VN, ZrN, and NbN).[18−20] Different from the routine pathways, lattice N atoms on the surface of TMNs are first hydrogenated to produce NH_3, leaving N vacancies behind. These N vacancies are subsequently refilled by the dissolved N_2, triggering the generation of second NH_3 molecule with the reduction of surface N atom. In contrast to these dissociative and associative pathways, N_2 activation on TMNs via the MvK mechanism requires relatively smaller overpotentials, contributing to a favorable NH_3 generation.

As depicted in Table 1, not only in acid (R1 and R2) but also in basic solutions (R3 and R4), the equilibrium potentials for electrocatalytic NRR are comparable to those of hydrogen evolution reactions (HER). However, NRR is a multiple proton/electron participated process (e.g., 6-electron transfer in R1 and R3) and involves several kinds of intermediates, making it kinetically difficult. As a consequence, most of the electrons and protons would preferably participate in HER. The much negative equilibrium potential in R5 for the first electron transfer shows a huge energy barrier, severely hampering the overall reaction rates. Meanwhile, the high-energy transition state in R6 for the formation of N_2H confirms the difficulty in the first-H addition. In view of smaller redox potentials for the two-electron and four-electron reduction processes (R7 and R8), the subsequent hydrogenation steps are easier comparing with the first-H atom. Theoretically, the process of electrocatalytic NRR is feasible provided with a proper external voltage. Nevertheless, the fundamental challenge is the lack of suitable catalysts with sufficient active sites for the efficient N_2 reduction. The competitive HER is usually predominant on the catalyst surface, leading to the extremely limited NH_3 yield rates with low Faradaic efficiencies (FEs).

2.4. Photocatalytic Pathways and Challenges. For the photocatalytic NRR processes, the associative manner (pathway ii, Figure 2a) including distal and alternating pathways has been widely accepted.[25] Under the irradiation of a light source, the photocatalysts trap energy to create photoinduced electron−hole (e−h) pairs (Figure 2b).[21] Then, electrons are migrated to the conduction band (CB), and the holes are left within the valence band (VB). Afterward, the photoexcited electrons and holes are transferred to active sites on the catalyst surface for the catalytic reactions. In the VB, the holes are participated in the oxidation reaction, using electron donors (e.g., H_2O) to produce proton and O_2. Simultaneously, the NH_3 is generated via the reduction reaction utilizing the trapped protons and adsorbed N_2 in the CB. In principle, to realize such a NRR route, the CB and VB positions of designed photocatalysts should be much more negative and positive than the potentials for N_2 hydrogenation and O_2 evolution, respectively.

In addition to the aforementioned N_2 reduction process, it should be noted that the emerging N_2 oxidation reaction (NOR) driven by the light irradiation has also received enormous attention.[26,27] Utilizing the photoexcited holes, N_2 is first oxidized to NO with H_2O (R9). Meanwhile, O_2 consumes the photogenerated electrons and is subsequently reduced to H_2O (R10). Finally, NO interacts with O_2 and H_2O and is further oxidized to the nitrate (NO_3^-, R11).[28]

$$N_2 + 2H_2O + 4h^+ \leftrightarrow 2NO + 4H^+ \tag{R9}$$

$$O_2 + 4H^+ + 4e^- \leftrightarrow 2H_2O \tag{R10}$$

$$4NO + 3O_2 + 2H_2O \leftrightarrow 4HNO_3 \tag{R11}$$

For the produced NO_3^-, some recent pioneering studies have confirmed the feasibility of its photocatalytic conversion to NH_3. Following the probable routes (R12 and R13), the photoinduced holes are consumed with the electron donors (e.g., HCOOH), resulting in a high selectivity in NH_3 production (up to ~97%).[29,30] Considering these promising routes, it is highly anticipated to offer an alternative strategy for the efficient photocatalytic NH_3 production.

$$HCOOH + 2h^+ \leftrightarrow CO_2 + 2H^+ \tag{R12}$$

$$NO_3^- + 9H^+ + 8e^- \leftrightarrow NH_3 + 3H_2O \tag{R13}$$
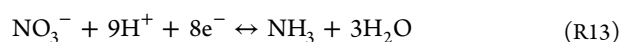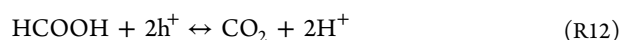
Actually, in the diverse N-containing species participated photocatalytic reactions, there is still uncertainty on the complicated reduction/oxidation routes, as well as the possible interconverted procedures and side reactions. Probably, both reductive/oxidative products (e.g., NH_3 and NO_3^-) could be observed simultaneously within the system. To this end, further exploration and understanding in the fundamental reaction mechanisms are urgently required.

As the primary focus in this Review, photocatalytic N_2 reduction process is still confronted with several challenges, which are remained to be addressed to achieve a satisfactory conversion efficiency. (i) N_2 activation: For most typical photocatalysts (e.g., Bi_5O_7Br, CuCr-LDH nanosheets (NSs) and Cu-TiO_2 NSs, Figure 2c),[22−24] their CB potentials (e.g., −1.43 eV for Bi_5O_7Br, −0.2 eV for CuCr-LDH NSs, −0.25 eV for Cu-TiO_2 NSs) are more positive than reduction potentials for the intermediate reactions, making them difficult for forming solvated electrons or direct N_2 fixation. Generally, there are two kinds of thermodynamic considerations, e.g., the thermodynamics of half- and global-reactions, and surface reactions and photon-induced processes, respectively.[31] The former is catalyst independent, while the latter is catalyst dependent. Despite the low probability in the electron transfer to N_2 following these one-electron participated steps (e.g., N_2 + e^- $\leftrightarrow$ N_2^-, − 4.20 V vs NHE and N_2 + H^+ + e^- $\leftrightarrow$ N_2H, − 3.20 V vs NHE, pH 0), these promising catalysts demonstrated the feasibility in photocatalytic NRR experimentally. Utilizing versatile active sites on the photocatalysts, an alternative route was established for triggering the chemisorption and activation of N_2 molecules, finally realizing the NH_3 synthesis with the successive transfer of electrons and protons. Although still with limited conversion efficiencies in contrast to that of industrial processes, these investigations demonstrate that an excellent N_2 adsorption and activation ability of designed photocatalysts plays a critical role in highly efficient photocatalytic NRR. (ii) e−h recombination: Once e−h pairs are formed under irradiations, the carriers would recombine with their counter-parts of opposite charge trapped on the catalyst surface (surface recombination), or the recombination of two carriers occurs in the bulk of the photocatalysts (volume recombination).[32] Both recombination processes are detrimental to the efficiency of the photocatalytic reaction. Thus, to enhance the solar conversion efficiency for photocatalytic NRR, it is requisite to suppress such e−h recombination and to achieve a longer lifetime of charge carriers. (iii) H_2O splitting reaction: Since solar H_2O splitting and N_2 reduction occur simultaneously within the system, it is imperative to enhance the N_2 reduction rate while suppressing the H_2O splitting. Typically, designed photocatalysts should specially adsorb N_2 molecules, while reserve necessary active sites for H_2O splitting to supply desired protons. (iv) Visible light response: While satisfying the critical preconditions toward efficient N_2 activation, it is desirable to develop promising photocatalysts with excellent response ability toward visible light. For instance, as a classical photocatalyst, TiO_2 with an unfavorable band gap of ~3.2 eV could merely be activated by UV or near-UV radiation, severely hampering its solar spectrum-utilization efficiency. (v) NH_3 oxidation. Because of the presence of photoinduced holes or reactive oxygen-containing species, the generated NH_3

would be further oxidized to NO_2^-/NO_3^-, which is detrimental for the NH_3 production and performance assessment of photocatalysts. Thus, developing catalysts with preferable N_2 adsorption capacity, or designing proper photocatalytic reactors to effectively remove these oxidative species is the probable route to circumvent this issue.

Coupling with the electrocatalytic and photocatalytic N_2 reduction pathways, an emerging route of photoelectrocatalytic NRR has attracted great attention recently.[33,34] Essentially, the photoelectrocatalysis involves a photocatalytic process in the presence of an external bias, which has been widely utilized in water splitting and CO_2 reduction reaction (CRR).[35−37] Benefiting from the merits from both photocatalysis and electrocatalysis, the reduction−oxidation abilities of photo-excited electron−holes are significantly enhanced to drive the reaction forward. In view of its comparable behaviors with electrocatalytic and photocatalytic NRR, the photoelectrocatalytic NRR pathway suffers similar challenges as mentioned previously, such as proton competition and N_2 activation.

To effectively address these challenges in NRR encountered in the photo/electrocatalysis, tremendous efforts have been dedicated to promoting the catalytic performance of NRR, mainly focusing on two aspects. On the one hand, the NRR conversion efficiency could be significantly improved via rational catalyst design, such as introducing versatile vacancies, exposing active crystal facets, fabricating a specific structure, and constructing a heterointerface.[38−40] For example, it was revealed that oxygen vacancies (OVs) played a critical role in N_2 reduction, through an effective improvement in N_2 chemisorption and stabilization of some reaction intermediates.[41] On the other hand, additional strategies, including tuning the electrolytes, enhancing N_2 mass transfer/reducing H_2O transport, designing a specific plasma electrolytic system, or utilizing lithium-mediated N_2 fixation, have been widely employed.[42−47] In this regard, a hydrophobic and high N_2-solubility (0.28 mg g^{-1}) ionic liquid was introduced as an alternative electrolyte for electrocatalytic N_2 reduction.[48] Benefiting from the significantly enhanced interaction with N_2 molecules and obvious suppression of HER, an impressive electrochemical NH_3 synthesis with a FE of ∼60% was achieved. Nevertheless, despite this high performance, the complex synthesis procedure and high cost of ionic liquid would definitely hinder its wide applications in practice.

Given the rapid development in this hot research area in the past few years, it is necessary to update timely progress for various strategies employed for overcoming critical challenges of the low conversion efficiency in NH_3 synthesis. Recently, several reviews on electrocatalytic or photocatalytic N_2 reduction processes have been reported, mainly regarding the reaction mechanisms and processes, different components and types of catalysts, as well as some discussions on cell configurations.[49−52] Some reviews are partially focused on the preparation strategies for electrocatalysts, or one aspect of defect engineering for designing desirable catalysts.[53−55] Few reviews have been reported on the comprehensive design strategies for the construction of promising catalysts, for instance, electrocatalysts, photocatalysts, and photoelectrocatalyts as well. Therefore, it is extremely urgent to summarize and discuss the research advances in this aspect, unveiling the underlying factors for guiding the synthesis of high-performance catalysts.

In this work, we systematically review the state-of-the-art research advancements to tackle the efficiency challenges in NRR, in the perspective of different strategies for rational catalyst design, including defect engineering, structural manipulation, crystallographic tailoring, and interface regulation, as depicted in Figure 3. On the basis of interdisciplinary
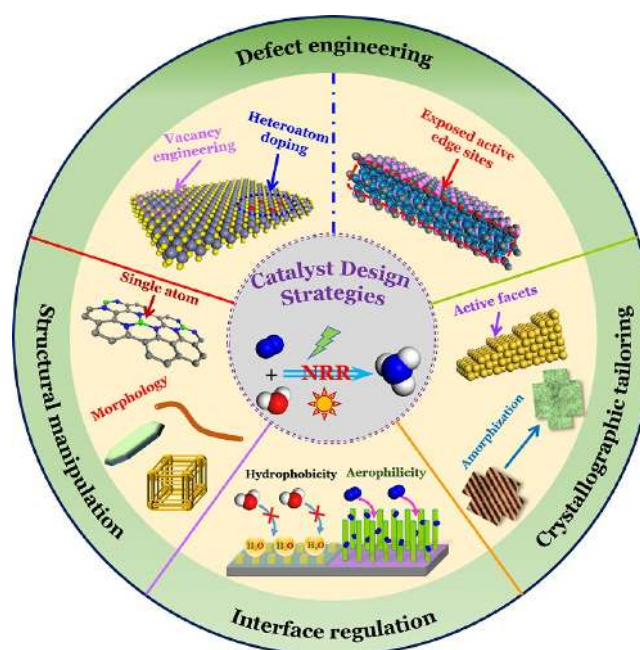

Figure 3. Schematic illustration of various design strategies for high-performance NRR catalysts.

knowledge of nanotechnology, material science, and chemistry, the precise manipulation toward catalysts at different dimensions varying from atom-scale (e.g., defect engineering), nanoscale (e.g., crystallographic tailoring) to microscale (e.g., interface regulation) is achieved with the proposed strategies. Finally, critical challenges and future perspectives in the research field are provided.

3. DEFECT ENGINEERING

3.1. Vacancies. Via introducing different vacancies into the catalysts, for example, O vacancies (OVs), N vacancies (NVs), and S vacancies (SVs), the vacancy engineering is considered as one of the most effective defect strategies to improve their catalytic behaviors in the NRR.[56] It has been revealed that the presence of various vacancies can effectively regulate the intrinsic properties including the electronic structure, charge transport, and surface adsorption capacity.[57,58] Accordingly, these vacancies behave as dominant adsorption and active sites for heterogeneous catalysis, lowering the activation energy barriers and facilitating the catalytic reactions. Furthermore, surface OVs and NVs with typical defect states are capable of trapping the photoinduced electrons or holes, inhibiting the e−h recombination process and promoting the migration of charge carriers to the adsorbates.[59]

3.1.1. Oxygen Vacancies (OVs). Possessing abundant localized electrons, OVs are extensively employed in efficient adsorption and activation of various molecules, such as O_2 and CO_2.[60−62] Enlightened by these reports, the tremendous potentials of OVs enriched catalysts toward accelerated N_2 adsorption and activation have been explored recently.[63−66] For instance, Zhang et al. reported an efficient visible-light NRR at OVs on the exposed BiOBr (001) facets (BOB-001-
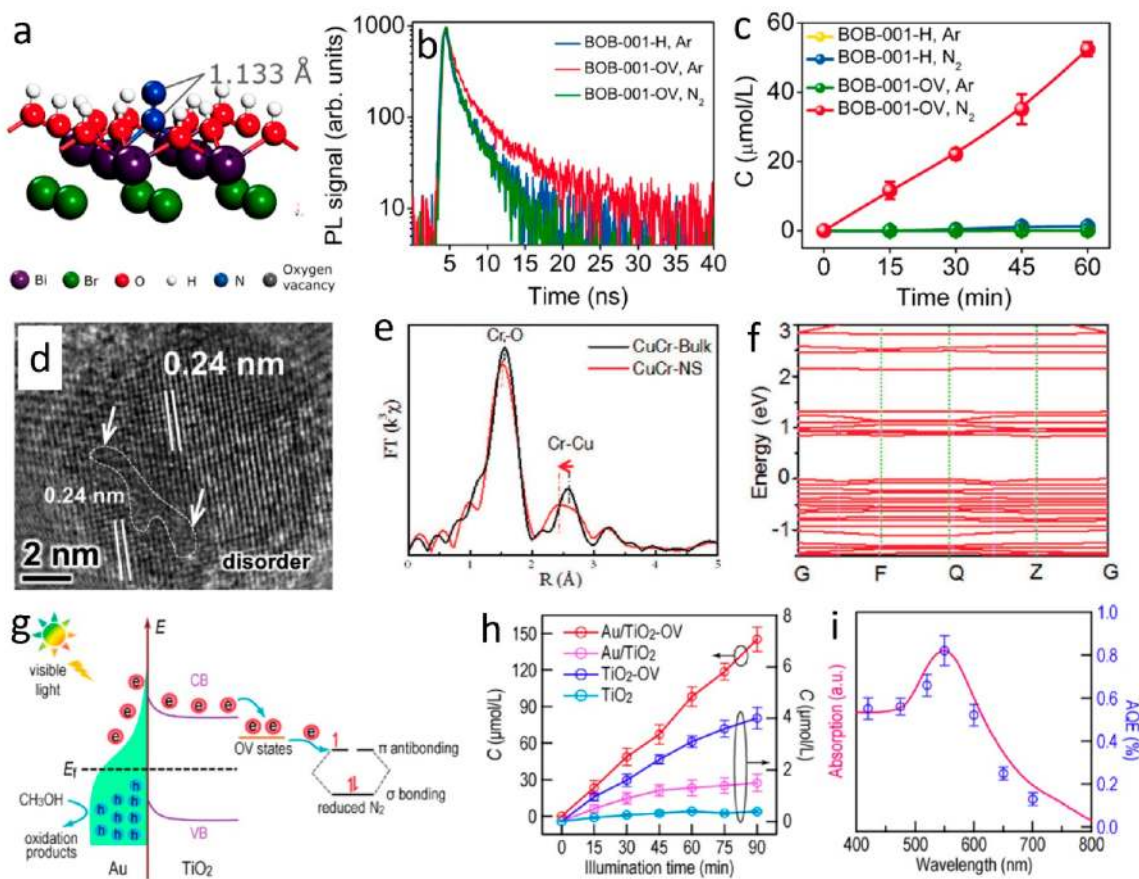
Figure 4. (a) Adsorption geometry of N_2 at OVs on BiOBr (001) surface. (b) Steady-state PL decay spectra and (c) NH_3 yields of the prepared photocatalysts. Reproduced with permission from ref 67. Copyright 2015 American Chemical Society. (d) HRTEM image of CuCr-NS. Dotted section: the structural distortions. (e) Cr K-edge extended X-ray absorption fine structure (EXAFS) spectra of CuCr-Bulk and CuCr-NS. (f) Band structure for CuCr-LDH with OVs and compressive strains. Reproduced with permission from ref 23. Copyright 2017 Wiley-VCH Verlag GmbH & Co. KGaA, Weinheim. (g) Schematic illustration of the photocatalytic N_2 reduction on Au/TiO_2-OV. (h) NH_3 yields of different photocatalysts. (i) Absorption and AQE of NH_3 production on Au/TiO_2-OV. Reproduced with permission from ref 69. Copyright 2018 American Chemical Society.

OV).[67] Via coordinating with the partially reduced and OV-connected Bi atoms, N_2 was adsorbed on OVs with an end-on bound structure. Back transfer of charges from OVs to adsorbed N_2 resulted in the N≡N activation, elongating the bond length from 1.078 to 1.133 Å (Figure 4a). Serving as electron trapping sites, the presence of OVs significantly promoted the interfacial charge transfer and increased the lifetime of charge carriers ($\tau = 2.15$ ns, Figure 4b), which was over 2 times longer than that of the photocatalyst without OVs ($\tau = 1.06$ ns, BOB-001-H). As expected, the designed catalyst with abundant OVs showed remarkably enhanced NH_3 production (Figure 4c), and a fixation rate of 104.2 μmol h^{-1} g^{-1} was observed under visible light. Despite the attractive advantages in N_2 fixation, most bismuth oxyhalides (BiOX, X = Cl, Br, and I) are susceptible to photocorrosion, and the surface OVs usually lose the catalytic activities due to easy oxidization. Therefore, to realize sustainable photocatalytic NRR procedures, designing highly stable photocatalysts with abundant OVs is indispensable. To address this issue, Chen and Ye et al. reported a novel NRR photocatalyst of Bi_5O_7Br nanotubes with reproducible surface OVs, high specific area of $\sim$96 m^2 g^{-1}, and compatible absorption edge.[22] On the one hand, a greatly improved stability of bismuth-enriched bismuth oxyhalides was secured via increasing the Bi/Br ratio,

compared with the traditional BiOX. On the other hand, the light-switching OVs were first created with partial O atoms escaping from the surface of Bi_5O_7Br nanotubes under visible light irradiations. After the NRR, these OVs were refilled by capturing O atoms from H_2O, eventually recovering to the initial stable state. Accordingly, a high NH_3 production rate of 1.38 mmol h^{-1} g^{-1} was achieved, with a superior apparent quantum efficiency (AQE) over 2.3% at 420 nm. Particularly, no noticeable loss in catalytic activity after 4 cycles, as well as subtle changes in crystalline structure and morphology after the reaction, confirmed a high stability of the designed photocatalyst. In another work, it was manifested that the presence of grain boundaries (GBs) in WO_3 could induce plentiful operando OVs under light irradiations, thus significantly promoting photocatalytic activity and stability toward N_2 reduction.[68] Given the concentration of OVs relying on the density of GBs, nanoporous WO_3 annealed at 600 °C (WO_3-600) with abundant GBs exhibited an optimal NH_3 production rate of 230 μmol h^{-1} g^{-1} without any sacrificial agents ($\sim$17-fold that of WO_3 without GBs). Attributed to a much better tolerance of the operando OVs toward H_2O/O_2, an impressive stability with $\sim$100% catalytic activity was maintained after 10 successive cycles. These pioneering studies provide insights into the generation of operando OVs, opening
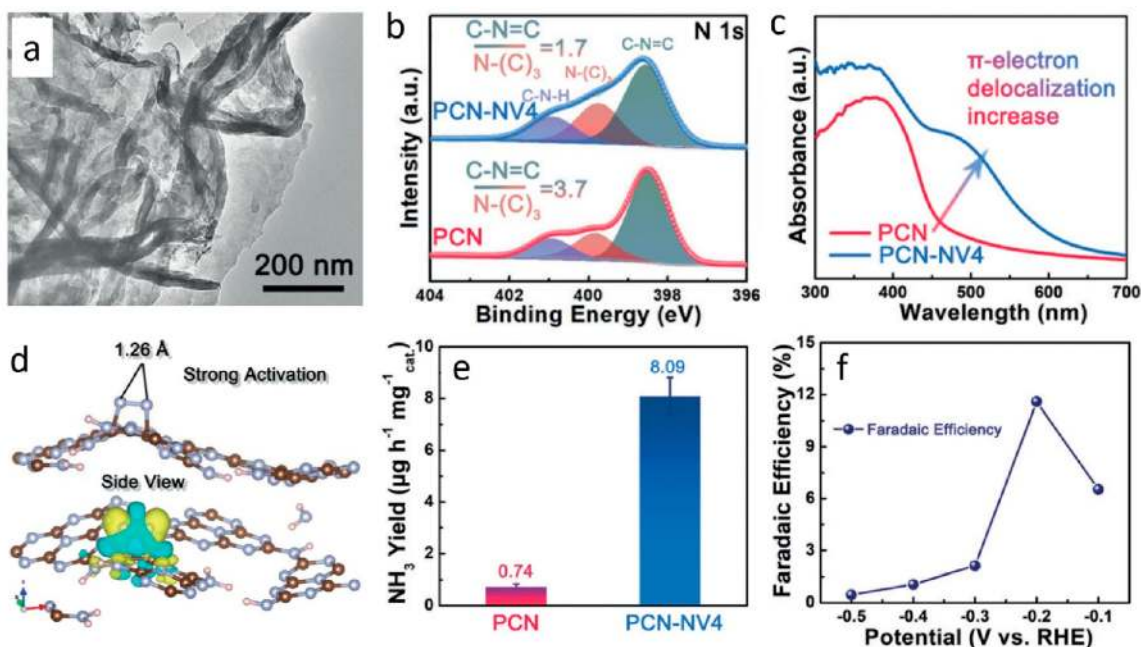
Figure 5. (a) TEM image of PCN-NV4. (b) N 1s X-ray photoelectron spectroscopy (XPS) spectra and (c) UV–vis diffuse reflection spectra of PCN and PCN-NV4. (d) The difference in charge density of N_2-adsorbed PCN engineered with NVs. (e) NH_3 production rates of PCN and PCN-NV4. (f) FEs of PCN-NV4 at different applied potentials. Reproduced with permission from ref 78. Copyright 2018 Wiley-VCH Verlag GmbH & Co. KGaA, Weinheim.

new avenues to design highly active and stable catalysts for NRR.

Intrinsically possessing sufficient surface defects such as OVs, 2D ultrathin layered-double-hydroxides (LDHs) have emerged as attractive catalysts or catalyst supports for a wide variety of heterogeneous catalysis.[70] The defect concentration increases with the thickness of 2D LDHs approaching atom-scales, creating abundant active sites that can not only facilitate reactant adsorption but also enhance visible-light absorption via reducing the bandgap. For instance, through decreasing the thickness of ZnAl-LDH NSs to ~2.7 nm, sufficient OVs accompanying with Zn^+−OVs complexes were generated as trapping sites for the accelerated adsorption of CO_2 and H_2O, improving the charge separation and significantly enhancing the performance in the photocatalytic CRR.[71] Inspired by these studies, a series of $M^{II}M^{III}$-LDH photocatalysts (M^{II} = Mg, Zn, Ni, Cu; M^{III} = Al, Cr) were fabricated and tested for NRR via tuning their compositions and morphologies.[23] Taking the CuCr-LDH with the remarkably high activity as an example, it possessed an ultrathin nanosheet morphology (CuCr-NS) with a thickness of ~2.5 nm. The introduction of Cu^{2+} strategically engineered OVs on the edge/surface of the CuCr-NS, inducing the structural distortions and resulting in slight lattice disorder and dislocations (Figure 4d). Playing important roles in the adsorption and activation of N_2, similar distortions were widely observed in other NRR catalysts (e.g., S-enriched MoS_2 nanoflower).[72] Meanwhile, the shorter distance (1.989 Å) of first Cr−O shell in CuCr-NS (1.990 Å in CuCr-Bulk, Figure 4e), as well as a reduced second Cr−Cu distance from 3.060 Å (CuCr-Bulk) to 3.056 Å (CuCr-NS), demonstrated a structural compression in the *ab*-plane of CuCr-NS. As revealed in DFT simulations, the presence of OVs and concomitant compressive strains imparted extensive defect levels within the bandgap (Figure 4f). These additionally generated energy states acted as trapping sites for

photoinduced electrons, thus remarkably facilitating the electron transfer from CuCr-NS to N_2 molecules. Accordingly, an obviously enhanced NH_3 formation was realized on CuCr-NS using H_2O as a proton source, resulting in a high yield of 57.1 μmol h^{-1} g^{-1} under the irradiation of visible light.

For practical applications, easily available and robust photocatalysts that could efficiently promote water oxidation and N_2 reduction are highly in demand. As an attempt, a notable work focusing on the classical commercial photo-catalyst of TiO_2 with OVs for NH_3 synthesis was performed by Shiraishi et al.[73] Exposed on the surface of TiO_2, active Ti^{3+} species on the OVs facilitated the N_2 adsorption through the electron donation and further dissociation of the N≡N bond. Undergoing the photocatalytic cycle of Ti^{3+} (initial species) → Ti^{4+} (Ti^{4+}-azo and Ti^{4+}-azo′) → Ti^{3+} (intermediate species) → Ti^{4+} (Ti^{4+}-hydrazo and Ti^{4+}-amine) → Ti^{3+} (initial species), these active surface Ti^{3+} sites were regenerated, realizing an efficient NH_3 production. Although exhibiting a low solar-to-chemical conversion (SCC) efficiency of 0.02%, the introduction of the low cost, highly stable, and noble-metal free TiO_2 potentially shed new light on the artificial NH_3 photosynthesis. Enlightened by this work, Wang and Jiang et al. further developed the photocatalyst of Au nanocrystals decorated on ultrathin TiO_2 NSs with abundant OVs (Au/TiO_2−OV) and demonstrated a photodriven NRR in the "working-in-tandem" manner (Figure 4g).[69] On the one hand, N_2 was adsorbed on the OVs of TiO_2 NSs, utilizing the electron transfer between the OV-induced Ti^{3+} and N_2. On the other hand, triggered by the localized surface plasmon resonance (LSPR) effect on the Au nanocrystals, generated hot electrons were injected into the CB of TiO_2 NSs and subsequently used for reducing activated N_2 molecules to NH_3. On account of the synergetic effect, proposed Au/TiO_2−OV showed a greatly boosted performance as compared to that of other catalysts under the irradiations of visible light (Figure
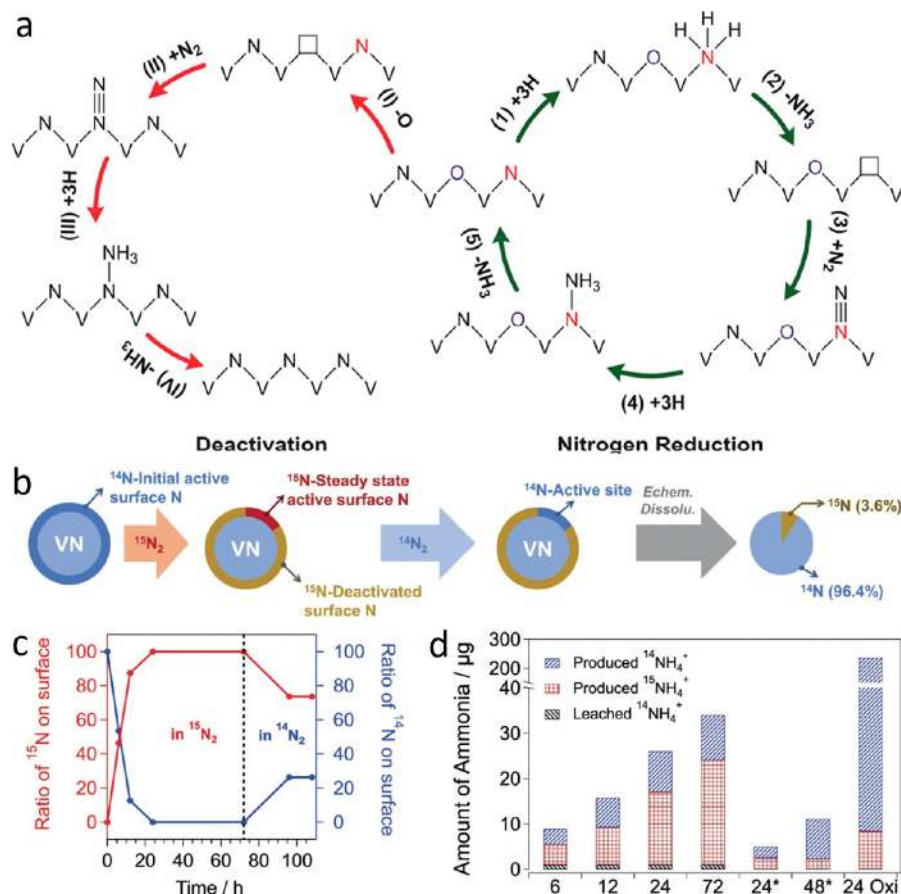
Figure 6. (a) N_2 reduction pathway on VNO following the MvK mechanism (right circle) and the deactivation mechanism (left circle) on catalyst. Reproduced with permission from ref 82. Copyright 2018 American Chemical Society. (b) Scheme of the isotopic exchange strategy on VNO. (c) Isotopic composition of active N sites vs reaction time. (d) Detected amounts of $^{14}NH_4^+$ and $^{15}NH_4^+$ in the NRR. Reproduced with permission from ref 83. Copyright 2019 Wiley-VCH Verlag GmbH & Co. KGaA, Weinheim.

4h). The observed NH_3 formation rate was 78.6 μmol h^{-1} g^{-1} (~98- and 35-fold those of Au/TiO$_2$ and TiO$_2$−OV), and the highest AQE of 0.82% was achieved at 550 nm (Figure 4i). Considering the indispensable role of OVs in the photocatalytic N_2 reduction, it is highly desirable to develop reliable synthetic strategies to realize precise modulation and control of OV concentrations in photocatalysts. Through a facile copper doping approach, Zhang et al. demonstrated a new pathway for optimizing the OV concentrations on ultrathin TiO$_2$ NSs.[24] The substitution of Ti^{4+} (0.64 Å) with larger Cu^{2+} (0.73 Å) generated abundant OVs stemmed from the Jahn−Teller distortions, as well as the concomitant lattice distortion and compressive strain. Ascribed to these positive factors, accelerated N_2 adsorption and favorable hydrogenation step of $N_2^* \rightarrow N_2H^*$ were achieved on the TiO$_2$−OV-Strain, resulting in a higher adsorption energy (−0.37 eV) while lower reaction energy (0.365 eV) than those of TiO$_2$−OV (adsorption energy: − 0.25 eV, reaction energy: 0.893 eV) and TiO$_2$−Pure (adsorption energy: − 0.17 eV, reaction energy: 2.115 eV). As a consequence, the designed catalyst exhibited an excellent photocatalytic activity in a wide solar absorption range, affording NH_3 yield rates of 78.9 μmol h^{-1} g^{-1} under full solar illumination, 1.54 μmol h^{-1} g^{-1} (quantum yield of 0.08%) and 0.72 μmol h^{-1} g^{-1} (quantum yield of 0.05%) under 600 and 700 nm irradiations, respectively.

3.1.2. Nitrogen Vacancies (NVs). Inspired by the impressive properties of OVs, the NVs have also received enormous

interests in the NRR recently.[74] Possessing a similar structure and size with the N atom, NVs-enriched catalysts can be regarded as the N_2-imprinted polymer, which could be adopted as N_2-selective adsorbents and activators.[75] Besides, it is known that the defective NVs can capture photoinduced electrons and hinder the recombination of e−h pairs. Carbon nitride is widely selected as the common matrix to introduce NVs, on account of its high N contents and typically layered structure that can supply sufficient and uniformly distributed NVs.[76,77] Recently, Yu and Chen et al. synthesized NVs-enriched polymeric carbon nitride (PCN-NV) via recalcination treatment of PCN in an Ar atmosphere.[78] Treating with an optimal recalcination time of 4 h, the catalyst (denoted as PCN-NV4) retained the 2D sheet-like morphology and possessed a transparent thin-layer structure (Figure 5a). Compared with a high ratio of C−N═C/N−(C)$_3$ of pristine PCN (3.7), the drastically decreased value to 1.7 manifested that the engineered NVs were preferentially located at N$_{2C}$ sites (Figure 5b). The introduction of NVs significantly enhanced π-electron delocalization (Figure 5c) and further redistributed additional electrons to adjacent C atoms. These electrons were transported to the adsorbed N_2 via a back-donation process, achieving a strong N_2 activation. Accordingly, the N≡N bonds were intensively weakened with the bond length increasing from 1.0975 Å in free N_2 to 1.26 Å (Figure 5d). The engineered PCN-NV4 remarkably enhanced the NH_3 yield

rate to 8.09 μg h^{-1} mg^{-1} (over 10-fold of PCN, Figure 5e), with a high FE of 11.59% at −0.2 V vs RHE (Figure 5f).

Moreover, the NVs-containing g-C$_3$N$_4$ also demonstrated its feasibility in the photocatalytic N$_2$ fixation, and various sacrificial electron donors (e.g., CH$_3$OH) were widely introduced to boost the conversion efficiency. In addition to acting as the hole scavenger, CH$_3$OH possessed a high solubility of N$_2$ and played the role as the proton supplier in NRR, contributing to a high NH$_3$ evolution rate of 3.632 mmol h^{-1} g^{-1} with an impressive AQE of 21.5% (∼420 nm) on the K$^+$ grafted g-C$_3$N$_4$.[79] Despite this prominent performance, it is highly desirable to conduct photocatalytic N$_2$ reduction directly using H$_2$O instead of CH$_3$OH as the proton supplier. To this end, an ideal photocatalyst should meet the requirements toward efficient H$_2$O oxidation and N$_2$ reduction simultaneously. In view of this point, a novel mesoporous photocatalyst of P-doped carbon nitride containing NVs was proposed for the NH$_3$ production from N$_2$ and H$_2$O by visible light irradiations.[80] With doped P behaving as sites for H$_2$O oxidation and NVs facilitating N$_2$ reduction, a satisfactory SCC efficiency of 0.1% was observed on the bifunctional catalyst. Coupling with two strategies of vacancy engineering and heteroatom doping (to be discussed in Section 3.2), this work offered a promising paradigm for the design and fabrication of highly efficient catalysts for artificial photosynthesis of NH$_3$.

In addition to these pretreated NVs on the catalysts, the self-formed NVs on the TMNs following the MvK mechanism have been experimentally demonstrated to be active in efficient NH$_3$ production recently.[81] As a paradigm, Xu and co-workers synthesized the VN nanoparticles via the urea-assisted pathway and performed a systematic investigation of catalytic mechanisms in the N$_2$ reduction.[82] Identified with the ex situ XPS and operando X-ray absorption spectroscopy (XAS), the VN$_{0.7}$O$_{0.45}$ (VNO) instead of the VN was confirmed as the active species. The surface N atom adjacent to the O atom first interacted with adsorbed H atoms, producing the NH$_3$ and leaving the N vacancy on the catalyst surface (right circle in Figure 6a). The subsequent capture of N$_2$ on the vacancy triggered next reduction cycle, and a mixture of ^{14}NH$_4^+$ and ^{15}NH$_4^+$ was produced in ^{15}N$_2$ stream. However, the unstable O atoms in the VNO were easily removable especially at more negative potentials, leading to the generation of surface OVs (left circle in Figure 6a). As further revealed in DFT calculations, N possessed a stronger binding strength toward the vacancy than that of O, resulting in the formation of the inactive VN phase. Operating at an appropriate potential of −0.1 V, the NH$_3$ yield rate of 330 pmol s^{-1} cm^{-2} with a FE of 6.0% was acquired within 1 h, and a steady-state evolution rate of 110 pmol s^{-1} cm^{-2} was maintained up to 116 h. Despite a higher NH$_3$ generation rate of 500 pmol s^{-1} cm^{-2} (FE of 6.5%) was achieved at a lower potential (e.g., − 0.2 V) within first 1 h, a severe activity loss (over 95%) was observed after 2 h, mainly ascribed to the rapid removal of O atoms and deactivation of the catalyst. To unveil the density of initial and steady-state active sites of NVO, the authors further developed an innovative exchange strategy through alternately substituting surface active N sites in ^{15}N/^{14}N sources (Figure 6b).[83] Under the ^{15}N$_2$ atmosphere, the produced ^{14}NH$_4^+$ plateaued at ∼10 μg after 24 h, while the amount of ^{15}NH$_4^+$ gradually increased to 23 μg over 72 h (Figure 6c,d). As estimated, only ∼4.2% active N of the total N in the catalyst participated in NRR. While further treating the spent catalysts in the ^{14}N$_2$ stream, a low ^{15}NH$_4^+$ amount of 2.5 μg indicated

that merely ∼25% of the active sites were available in the steady state (Figure 6d). These important discoveries not only open new horizons in designing high-performance TMN-based catalysts (e.g., via increasing the amount and stability of surface O atoms), but also provide a strong pathway to identify the intrinsic active sites on the catalysts.

3.1.3. Sulfur Vacancies (SVs). As the important nonmetal element in nitrogenases, the S element is confirmed to play a significant role in biological N$_2$ reduction. Besides, considering its comparable chemical properties with O, increasing attention has been dedicated to engineering SVs into the S-containing catalysts and exploring their potentials in the NRR. Lately, Li et al. demonstrated that SVs formed in the multicomponent ternary metal sulfide of ZnSnCdS exhibited an enhancement effect on N$_2$ photofixation.[84] In addition to the improvement in the adsorption and activation of N$_2$ molecules, the presence of SVs promoted the charge transfer from the metal sulfide to N$_2$, thus tremendously improving the N$_2$ photoreduction efficiency. As another classical S-containing material, 2D-layered MoS$_2$ with unique electronic, optical, and mechanical properties has attracted enormous attention in the catalytic fields.[85,86] The amount of SVs in MoS$_2$ can be significantly improved via regulating its layers to the ultrathin form or atomic thickness. For this purpose, Wang et al. prepared ultrathin MoS$_2$ NSs (3−5 layers of S−Mo−S) with a sonicating treatment and achieved a large amount of SVs with stoichiometry Mo/S ratio of 1:1.75.[87] Owing to the abundant SVs in the ultrathin MoS$_2$, the captured N$_2$ molecules on SVs were activated with donating electrons from the bonding orbitals, and receiving electrons to the three antibonding orbitals. Upon the light irradiation, the photo-induced charged excitons located at Mo atoms interacted with adsorbed N$_2$ molecules, resulting in the trion induced multielectron reduction process. Compared with bulk MoS$_2$ with subtle N$_2$ reduction activity, the ultrathin MoS$_2$ NSs showed an obviously enhanced NH$_3$ synthesis rate of 325 μmol h^{-1} g^{-1}. Apart from the function for N$_2$ activation, SVs on MoS$_2$ could act as efficient H-providers to directly transfer *H to nearby bound N$_2$, opening a new route for N$_2$ reduction.[88] More importantly, the H$^+$ reduction kinetics could be tuned with different MoS$_2$ polymorphs (1T- and 2H-MoS$_2$). In contrast with the "metallic" type 1T-MoS$_2$, the semiconducting property of 2H-MoS$_2$ endowed a lower CB level below H$^+$/H$_2$ redox potential, exhibiting an effective suppression toward HER. Coupling with amorphous Ru clusters as N$_2$ binding sites, a novel catalyst of Ru/2H-MoS$_2$ was designed for achieving a highly active and selective NRR. Hydrogenated SVs (*^{SV}H) transferred *H to N$_2$ bound on the Ru (*^{Ru}N$_2$) following the *^{Ru}N$_2$ + *^{SV}H ↔ *^{Ru}N$_2$H, with the regeneration of SVs for further proton reduction procedures. On the basis of this ingenious catalyst design, the NH$_3$ formation rate of 114 pmol s^{-1} cm^{-2} with a high FE of 17.6% was obtained at 50 °C.

In virtue of rich physicochemical properties created on versatile vacancies, it will inspire growing research interests for designing qualified catalysts for NRR applications via vacancy engineering. Despite these achievements, the research in this area is still challenged with some critical issues and thus filled with opportunities. To exactly elucidate the underlying factors of vacancies that determine catalytic behaviors, the first challenge is to select and establish advanced techniques and approaches to reveal the existence, position, and concentration of the vacancies. Second, most of the reported catalysts are
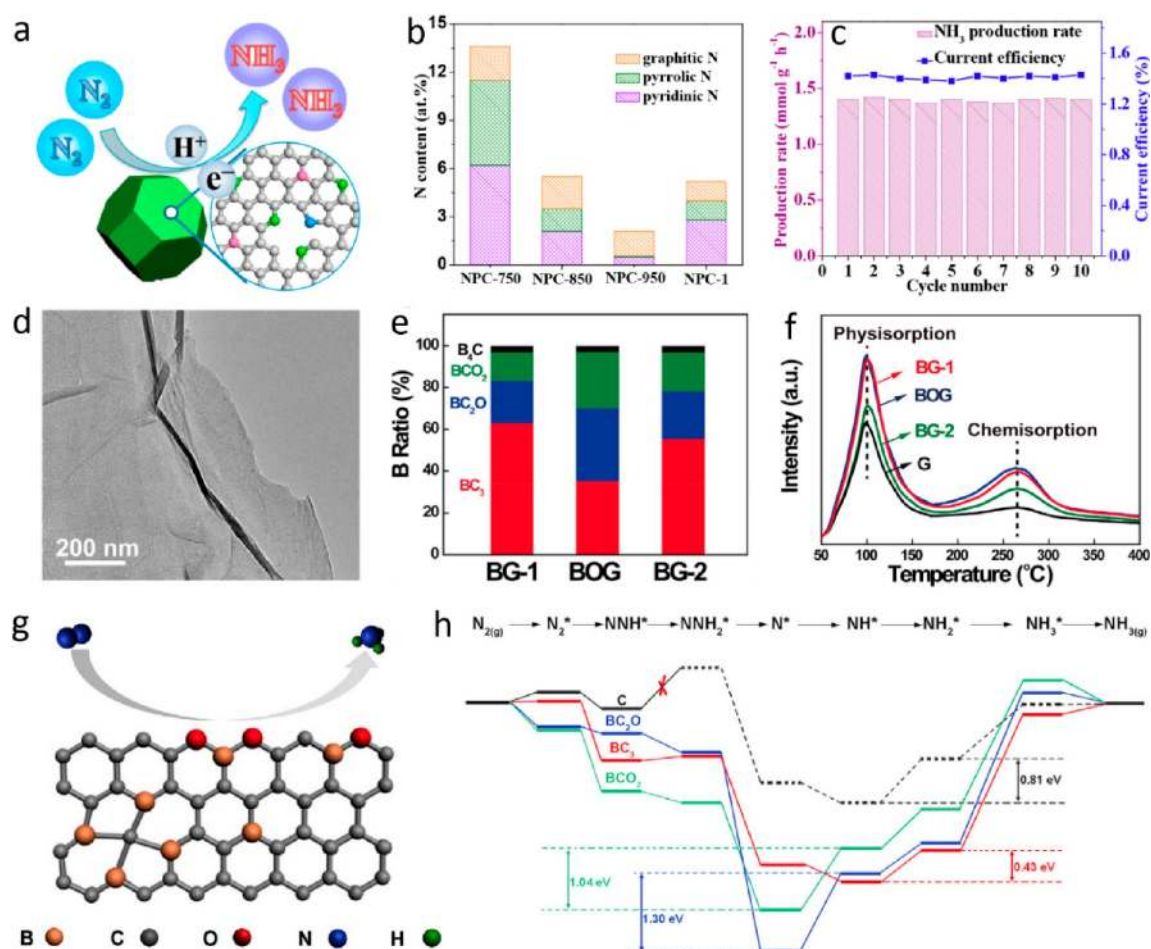
Figure 7. (a) Schematic illustration of N_2 reduction on NPC. (b) Contents of different N species. (c) NH_3 production rates and FEs recorded in 10 consecutive tests. Reproduced with permission from ref 103. Copyright 2018 American Chemical Society. (d) TEM image of BG-1. (e) Percentages of various B types in the BG samples. (f) N_2 temperature-programmed desorption curves of graphene (G) and three BG samples. (g) Schematic of NRR on the BG. (h) Free-energy diagrams of NRR on different B−C structures. Reproduced with permission from ref 107. Copyright 2018 Elsevier.

engineered with OVs and NVs. The introduction and application of other types of vacancies are still limited. To expand the varieties of vacancies enriched catalysts, novel vacancies (such as P, S, and C), as well as dual- or multivacancies are deserved to be explored in future and reliable approaches to manipulate the desired vacancies onto catalysts are urgently required. Third, to clarify the vacancy-mediated reaction pathways, it is highly imperative to monitor the reaction intermediates during catalytic processes, using in situ/operando characterization methods. For example, in situ scanning tunneling microscopy (STM) was recently applied for exploring the electrocatalytic dynamics on OVs enriched TiO_2-(110) surface in HER.[89] Finally, it is important to unveil the critical factors to maintain a high stability of vacancies, considering that the surface OVs/NVs are easily deactivated by refilling the O/N atoms. To address this issue, partially filling these vacancies with nonmetal dopants was demonstrated to dramatically improve the stability.[90,91] As a paradigm, the cycling stability of g-C_3N_4 in electrocatalytic NRR was significantly boosted through filling the NVs with S dopants.[91] All of these aspects are crucial in the further advancement of designing promising NRR catalysts.

3.2. Heteroatom Doping. Doping with a heteroatom is regarded as another effective approach to tailor electronic structures, manipulate surface features, and modify the chemical composition of catalysts.[92] Generally, there are two kinds of heteroatom doping: nonmetal and metal doping. For example, via inducing charge and spin densities on C atoms near dopants, the nonmetal doping with B, N, S, Cl, and P toward carbon materials can not only regulate the adsorption/desorption behaviors of the reactants, intermediates and products on the catalyst surface but also favor the electron transfer.[93−95] As a consequence, numerous active sites are created and significantly enhanced catalytic activity is observed. For the type of metal doping, various dopants of TMs (e.g., Cu, Fe, Co, and Ni) have been extensively investigated for enhancing the catalytic activities of photocatalysts.[96,97] It was found that doping with metal ions would lead to the red shift of the photoresponse. Moreover, in view of the impurity energy levels produced within band gaps of photocatalysts, metal doping could reduce the e−h recombination and thus enhance the transfer of charge carriers.

3.2.1. Nonmetal Doping. Owing to the large specific area and abundant pores providing sufficient binding sites and fast mass-transfer routes, N-doped porous carbon (NPC) is extensively used in supercapacitor, battery, and CO_2 capture.[98−100] Notably, N doping modifies the electronic structure and induces the defect formation and charge
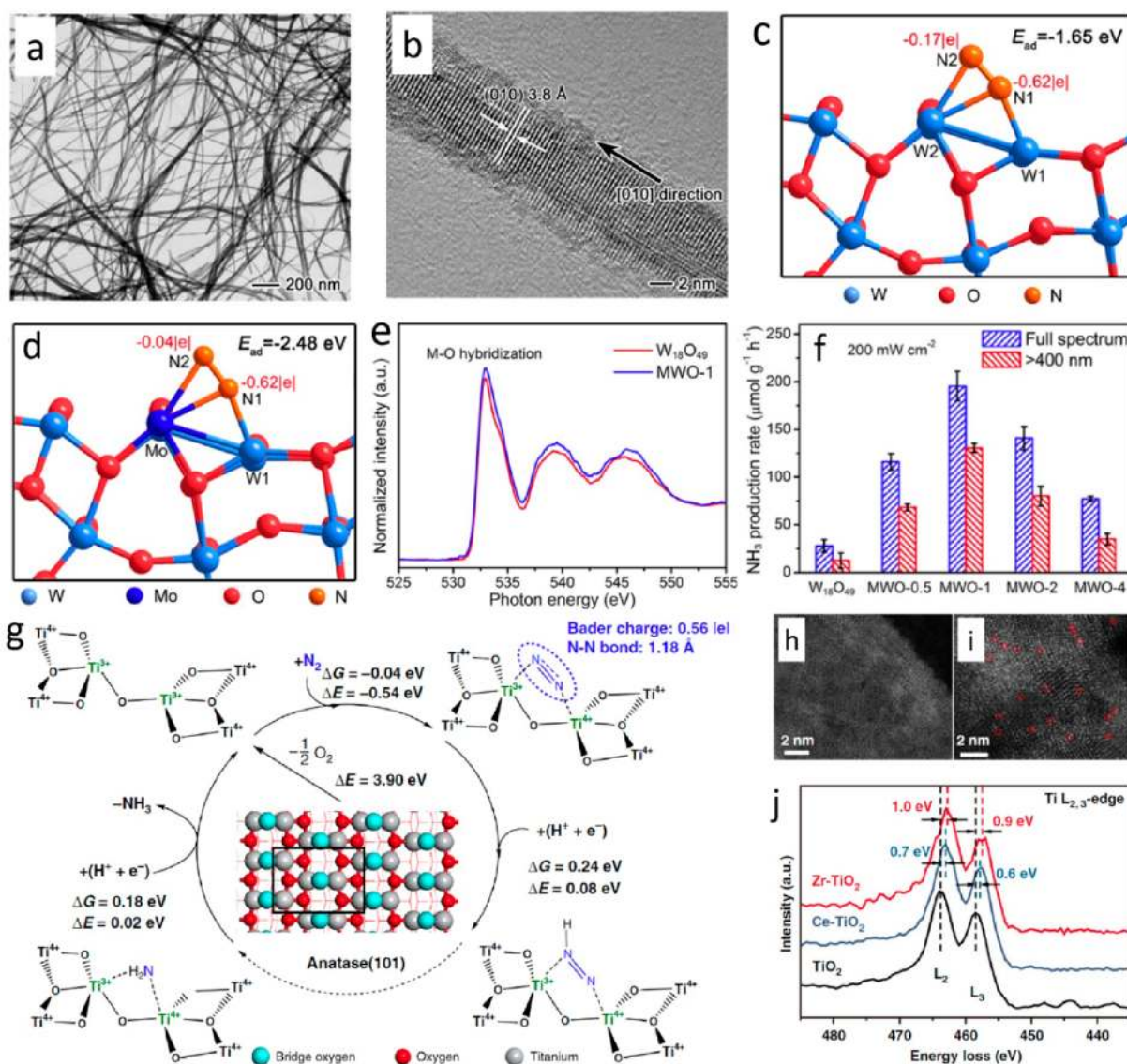
Figure 8. (a) TEM, and (b) HRTEM images of MWO-1 nanowires. Optimized N_2 adsorption configurations with corresponding charge distributions on (c) defect-rich $W_{18}O_{49}$ and (d) Mo-doped $W_{18}O_{49}$. (e) O K-edge XAS spectra of MWO-1 and $W_{18}O_{49}$. (f) NH_3 production rates of various photocatalysts. Reproduced with permission from ref 119. Copyright 2018 American Chemical Society. (g) DFT calculations for N_2 reduction on the adjacent bi-Ti^{3+} on anatase (101) surfaces with OVs. High-angle annular dark-field scanning transmission electron microscopy (HAADF-STEM) images of (h) TiO_2 and (i) $Zr-TiO_2$. (j) Electron energy loss spectroscopy (EELS) profiles of the Ti-$L_{2,3}$ edge of the $Zr-TiO_2$ catalyst. Reproduced with permission from ref 120. Copyright 2019 Springer Nature.

polarization, resulting in enhanced adsorption and catalytic activity as demonstrated in the O_2 reduction reaction (ORR) and NRR.[101,102] Derived from the pyrolysis of zeolitic imidazolate framework-8 (ZIF-8), a cost-effective NPC electrocatalyst was first reported for NH_3 production (Figure 7a).[103] Composed of Zn as metal nodes and 2-methylimidazole as organic linkers, ZIF-8 is widely applied as a carbon precursor for the preparation of NPC, leaving N-doped carbon skeletons with homogeneous pores for the beneficial diffusion of the reactants during catalysis.[104] Prepared NPC possessed a high amount of N and controllable N species (pyridinic, pyrrolic, and graphitic N) at different calcination temperatures (Figure 7b), in which pyridinic/pyrrolic N were demonstrated as active centers for N_2 chemical adsorption and N≡N cleavage. Undergoing a preferable pathway of *N≡N → *NH=NH → *NH_2–NH_2 → 2NH_3, a maximum FE of

1.42% with stable NH_3 yield rate of 1.40 mmol h^{-1} g^{-1} was obtained on NPC calcinated at 750 °C (−0.9 V vs RHE, Figure 7c). In similar studies, pyridinic-N in the NPC was confirmed as critical sites to facilitate the N_2 adsorption and dissociation of N≡N bonds, thus contributing to the significantly enhanced NH_3 production.[105,106] These explorations provide new insights into the catalyst design with desired N content and type, which would contribute to an efficient NRR under ambient conditions.

Apart from the N doping, the doping with B element would induce electron deficiency in carbon materials, resulting in substantially improved electrocatalytic activities in ORR and CRR.[108,109] Given a smaller electronegativity of B (2.04) compared with C (2.55), an efficient redistribution of electron density would be observed on the B-doped carbon ring structure. Positively charged B atoms are favorable for N_2

adsorption, serving as excellent catalytic centers to form the B−N bonds for the subsequent NH_3 production. Meanwhile, the prohibited binding toward excessive H^+ will promote the FE via the suppression of HER. In this regard, Zheng and Ma et al. proposed an electrocatalyst of B-doped graphene (BG) with a typical 2D layer morphology for the efficient NRR (Figure 7d).[107] Containing four B−C structures of B_4C, BC_3, BC_2O, and BCO_2 (Figure 7e), the doping of B enhanced the chemisorption capability toward N_2 molecules (Figure 7f). Among different B−C structures, G-like BC_3-type structure presented the most favorable binding capability and highest catalytic activity, serving as major electrocatalytic sites in the NRR (Figure 7g). In view of a preferable energy profile, a lower reaction energy barrier of 0.43 eV was estimated in the limiting step ($NH^* \rightarrow NH_2^*$) on BC_3 with the theoretical calculations (Figure 7h), compared with those of BCO_2 (1.04 eV) and BC_2O (1.30 eV) for the $N^* \rightarrow NH^*$ process. Accordingly, the resultant BG-1 catalyst with a high percentage of BC_3 displayed excellent catalytic performance, with NH_3 yield rate of 9.8 $\mu g\ h^{-1}\ cm^{-2}$ and a FE of 10.8% (−0.5 V vs RHE).

In addition to familiar doping with N and B, a recent study proved that doping of S atom also strengthened the NRR performance of carbon nanospheres (S-CNS).[110] With a comparable behavior of N and B atoms, the presence of S atoms improved the capability for physisorption and chemisorption toward N_2. Accordingly, designed catalyst achieved a high NH_3 yield rate of 19.07 $\mu g\ h^{-1}\ mg^{-1}$ with a high FE of 7.47% at −0.7 V (vs RHE, ∼ 3.70 $\mu g\ h^{-1}\ mg^{-1}$ and FE of 1.45% of CNS). More importantly, employing the earth-abundant sucrose as the carbon source, this work offers a new avenue to fabricate low-cost and easy-available NRR catalysts.

Furthermore, the codoping strategy with diverse heteroatoms, such as N/B, N/S and N/P, has been extensively utilized to design efficient ORR, HER, and NRR catalysts.[111−113] Inspired by these pioneering N and B doping works, Wang and co-workers demonstrated that codoping of both atoms into the carbon NSs significantly enhanced the NRR performance via the synergetic effect.[114] On the one hand, a lower free-energy change (ΔG = 1.72 eV) was achieved on the codoped catalyst in the protonation step ($^*N_2 \rightarrow {}^*N_2H$) than those of single B (2.24 eV) or N (1.99 eV) doping, indicating a favorable N_2H bonding and excellent activity after the codoping. On the other hand, a high adsorption free energy of $^*H$ species (0.65 eV) confirmed that the N/B codoping significantly retarded the HER activity. Serving as the active triggers, the formed B−N pairs activated near edge C atoms as the catalytic centers for N_2 reduction, exhibiting a high NH_3 yield rate of 7.75 $\mu g\ h^{-1}\ mg^{-1}$ with an enhanced FE of 13.79% at −0.3 V (vs RHE).

The doping of nonmetal elements into metal oxides (e.g., B-doped MnO_2 NSs, F-doped SnO_2 NSs) or oxide-hydroxides (e.g., F-doped β-FeOOH) has also received enormous attention in NRR recently.[115−117] In addition to those familiar merits, such as effective regulation on the electronic structures, improved conductivity, and reduced energy barriers for N_2 reduction, the nonmetal doping into metal oxides could exceptionally induce the desirable OVs. It was confirmed that B doping into the MnO_2 NSs created abundant OVs, through preferentially replacing the O atom instead of the Mn atom.[115] The combination of B-dopants and OVs resulted in an enhanced NRR activity, displaying an ultrahigh NH_3 yield rate

of 54.2 $\mu g\ h^{-1}\ mg^{-1}$ (−0.4 V vs RHE) with a FE of 16.8% (−0.2 V vs RHE).

3.2.2. Metal Doping. As the active sites in nitrogenase enzymes, the FeMo-cofactor catalyzes the reduction reaction to produce NH_3 with solvated protons, electrons, and atmospheric N_2 at ambient conditions. Triggered by this discovery, the doping of Mo has received great interests for the development of promising NRR catalysts.[118,119] To this end, Xiong and coauthors first confirmed the feasibility of Mo doping into $W_{18}O_{49}$ lattice for the development of an efficient NRR catalyst.[119] With a low substitution of W atoms with 1 mol % Mo (MWO-1), ultrathin nanowires (Figure 8a) with sufficient exposed active sites grow along the [010] direction with ordered lattice fringes (Figure 8b). The Mo doping offered active sites for N_2 adsorption, and two N atoms were more easily polarized on the Mo−W center, with a substantially increased charge difference of 0.58e (0.45e on the W−W site, Figure 8c,d). Accordingly, a larger adsorption energy of N_2 (−2.48 eV) was induced after the Mo doping, in contrast to the −1.65 eV of pristine $W_{18}O_{49}$. Meanwhile, the Mo doping facilitated the electron transfer from metal sites to captured N_2, showing a higher peak at 533 eV with the enhanced metal−oxygen (M−O) covalency (Figure 8e). Moreover, the doped Mo sites elevated the defect-band center toward the Fermi level, accumulating more active electrons for N_2 reduction. All of these merits synergetically accelerated the N_2 adsorption and activation on MWO-1, achieving a high yield rate of 195.5 $\mu mol\ h^{-1}\ g^{-1}$ (∼7-fold that of $W_{18}O_{49}$, Figure 8f), with an AQE of 0.33% at 400 nm.

As another critical metal element in the cofactors, Fe was also extensively applied as the dopant to improve the photo/electrocatalytic performance in NRR. For instance, via homogeneously substituting Ti^{4+} sites in the TiO_2 lattice, the doped Fe^{3+} effectively inhibited the e−h recombination and substantially improved the concentration of charge carriers.[121] The resultant catalyst showed an enhanced quantum yield of 0.1827 m^{-2} under UV light irradiation (∼3.84 times compared with pristine TiO_2). Inspired by this research work, the doping of Fe^{3+} into g-C_3N_4 was proposed to realize an outstanding N_2 photofixation performance under visible light.[122] To this end, Fe^{3+} was anchored at the interstitial sites and stabilized via the Fe−N bonds in the electron enriched g-C_3N_4. The doping with Fe^{3+} sites not only effectively promoted the chemisorption and activation of N_2 molecules but also remarkably enhanced the specific area of the catalyst to 45.5 $m^2\ g^{-1}$ (∼7.7 $m^2\ g^{-1}$ of g-C_3N_4), providing sufficient active sites for N_2 reduction. Thus, a significantly boosted NH_3 production rate of 5.40 $mg\ L^{-1}\ h^{-1}\ g^{-1}$ was acquired (∼13.5-fold that of g-C_3N_4). Lately, Sun et al. first demonstrated the Fe doped TiO_2 as an effective electrocatalyst for boosting the N_2 reduction activity.[123] On account of the charge compensation between the lattice defects and metal dopants, the introduction of Fe into TiO_2 substantially increased the concentration of OVs. Meanwhile, the observed Ti^{3+} active species were generated after the Ti^{4+} receiving electrons from adjacent OVs. As revealed in the theoretical calculations, the presence of a pair of Ti^{3+} sites (bi-Ti^{3+}) and OVs synergistically enhanced the back-donation of electrons to N_2 and promoted the key conversion of $^*NH_2NH_2 \rightarrow {}^*NH_2 + {}^*NH_3$, contributing to an excellent performance with a high NH_3 yield rate of 25.47 $\mu g\ h^{-1}\ mg^{-1}$ and an impressive FE of 25.6% (−0.40 V vs RHE). Comparably, the incorporation of Fe into CeO_2 not only introduced rich OVs but also produced active $Ce^{3+}-Ce^{3+}$ pairs
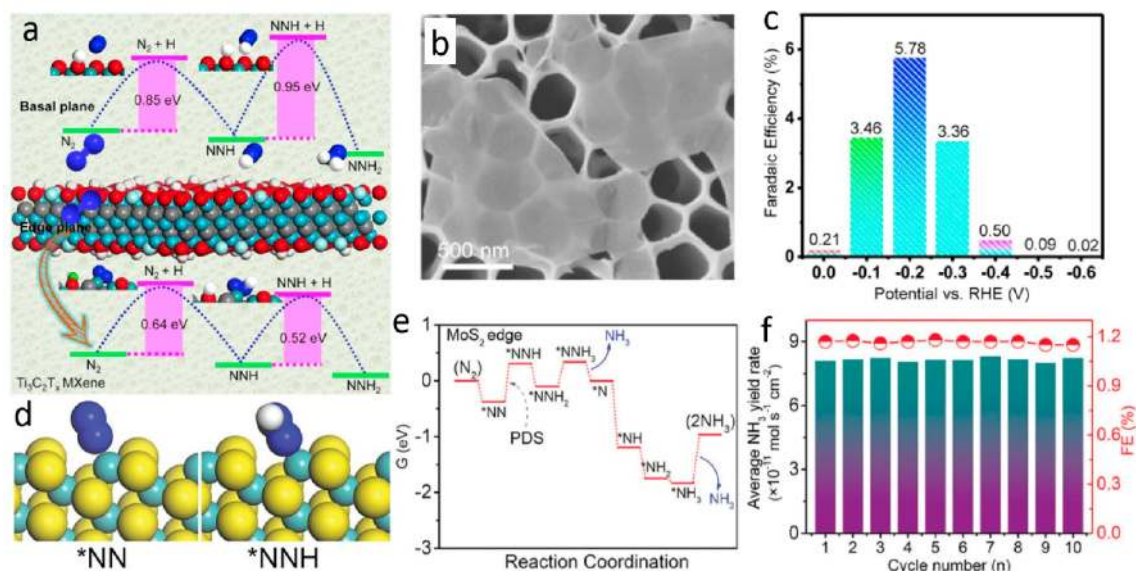
Figure 9. (a) Schematic structures and energies of the intermediates and transition states for NRR on the basal and edge planes. (b) SEM of ultrathin $Ti_3C_2T_x$ NSs. (c) FEs obtained at various potentials. Reproduced with permission from ref 138. Copyright 2018 Elsevier. (d) The structures of *NN and *NNH on Mo-edge. (e) Free-energy profile for NRR at MoS_2 edge site. (f) Stability evaluation with 10 successive tests. Reproduced with permission from ref 139. Copyright 2018 Wiley-VCH Verlag GmbH & Co. KGaA, Weinheim.

to improve the selectivity of NRR over HER.[124] Moreover, Fe doping induced the morphology evolution from CeO_2 nanoparticles ($\sim$38.5 m^2 g^{-1}) to nanosheets with a larger surface area ($\sim$73.2 m^2 g^{-1}). Ascribed to these synergetic effects, a remarkably enhanced NH_3 yield of 26.2 μg h^{-1} mg^{-1} was realized on the Fe-CeO_2 ($\sim$7.6 μg h^{-1} mg^{-1} on CeO_2).

Enlightened by these doping researches with Mo and Fe, Zhao and Liu et al. designed a novel photocatalyst of Fe doped $SrMoO_4$ for solar N_2 reduction.[125] On the one hand, the Fe doping effectively regulated the bandgaps of doped $SrMoO_4$ (from 3.98 to 2.93 eV), thus extending the light responses from UV to visible light region. On the other hand, Fe doping induced the formation of surface defects (e.g., OVs), which were beneficial for the N_2 adsorption and interfacial electron migration. Under the light illumination, the photoexcited electrons from the CB of photocatalyst were migrated to these active sites (e.g., surface defects or Fe–Mo centers) for the reduction of adsorbed N_2. Owing to the wide light absorption range and newly created active centers, an improved photocatalytic NH_3 production rate of 93.1 μM h^{-1} g^{-1} was acquired ($\sim$66.7 μM h^{-1} g^{-1} of undoped $SrMoO_4$).

On account of its comparable d-electron configuration, similar oxide structure, and suitable atom size, Zr^{4+} was first doped into TiO_2 for the design of a novel NRR electrocatalyst (Zr-TiO_2).[120] Different from the familiar low-valence metal dopants utilized in the formation of OVs, the doping with stable Zr^{4+} introduced the tensile and compressive strain, facilitating the generation of abundant OVs associated with adjacent bi-Ti^{3+} sites. As revealed in the theoretical calculations, these bi-Ti^{3+} sites on anatase (101) surfaces effectively enhanced the chemisorption of N_2 following a lying-down manner (Figure 8g), realizing a significantly elongated N/N bond length of 1.18 Å (1.13 Å in single Ti^{3+} site) coupling with a lower reaction free energy ($\Delta G = 0.24$ eV) for the first hydrogenation step (0.50 eV in single Ti^{3+} site). The successful occupation of original Ti^{4+} sites with Zr^{4+} was confirmed with the HAADF-STEM (Figure 8h,i), with a

homogeneous distribution of Zr^{4+} ions highlighted in red circles. Besides, the Zr^{4+} incorporation elevated the content of the unoccupied Ti 3d state and distorted Ti^{3+} coordination, resulting in the peak shifts to lower energy at 457.5 (Ti-L_3) and 462.7 eV (Ti-L_2) (Figure 8j). With a significantly enhanced Ti^{3+} ratio of 29.1% (8.5% of undoped TiO_2), the designed Zr-TiO_2 showed a remarkably boosted performance in NRR, with the NH_3 production rate of 8.90 μg h^{-1} cm^{-2} and a high FE of 17.3% at −0.45 V (vs RHE).

According to the above discussions, the doping strategy offers an efficient pathway to regulate the properties of various catalysts, making them qualified candidates for achieving high-performance N_2 reduction at ambient conditions.[126] Although reported FEs are far below the desired value ($\sim$90%) proposed by the U.S. Department of Energy's ARPA-E REFUEL Program,[127] some representative catalysts showed impressive activities with FEs over 10%, exhibiting a great potential for further investigations. However, several issues still exist in the doping strategy. First, the precise manipulation on the doping type of heteroatoms is a huge challenge. The regulation of specific doping types (e.g., N type of pyridinic-N and B type of BC_3) is highly demanded for catalysis applications, and the correlation between the activity and element type is required to be explored and identified. Second, achieving controllable doping at the desired positions and regulation of doping level is unresolved. Third, a reliable approach for the mass production of doped catalysts is still lacking, and developing an appropriate route is urgently required. Finally, for some N-doped or N-containing catalysts, their chemical and structural stability should be carefully investigated to avoid any ambiguous results arising from the exogenous contamination or the catalyst decomposition.[128]

In addition to these challenges, some aspects deserve further efforts in the following research. To design efficient NRR catalysts, particular attention can be paid on the metal-free carbon nanomaterials. As a comparison to metal-based catalysts, carbon nanomaterials have several distinct character-

istics, such as large specific areas, abundant natural resources, tailorable structures, excellent stability, and environmental friendliness.[129,130] Nonetheless, because of the easy contamination with NH_3 or other chemicals containing $-NH_2$ groups on the carbon surface, it is necessary to properly store or thoroughly wash such catalysts prior to measurements. Besides, stimulated by the impressive performance achieved via the codoping, it is highly desired to develop many other fascinating catalysts via multicomponent doping strategy. Utilizing the synergistic effect from different heteroatoms, it will open new horizons for the development of promising NRR catalysts. Moreover, advanced theoretical investigations are required to provide further guidance on the doping strategy for rational material design, via figuring out the doping types and anchoring sites of heteroatoms.

3.3. Edge Engineering. Edge engineering plays a crucial role in adjusting the growth kinetics and morphological evolution in 2D materials, such as typical graphene, transition-metal carbides, nitrides, or carbonitrides (MXenes) and transition-metal dichalcogenides (TMDs), affording a diversity of edge structures and endowing different electronic structures and functionalities.[131,132] For example, possessing higher charge densities, the edge C atoms of graphene was confirmed to offer more active sites than the basal-plane C, showing an efficient electrocatalytic activity in ORR.[133] Therefore, realizing the edge evolution in 2D materials is highly desired for designing ideal and functional NRR catalysts.

MXenes have been extensively used in separation, energy storage, and catalysis.[134−136] A recent theoretical investigation revealed that MXenes (e.g., V_3C_2 and Nb_3C_2) with M atoms composing the terminal surface were able to activate N_2 molecules, exhibiting great potentials in NH_3 synthesis.[137] Unfortunately, when terminated with oxygen-containing groups (e.g., OH* and O*) that directly bound with surface M atoms, the basal plane of 2D MXene exhibited weak binding ability to N_2, resulting in a limited catalytic efficiency in NRR compared with the competitive HER.[138] Alternatively, through intentionally exposing sufficient active sites at the edge plane, an MXene of $Ti_3C_2T_x$ (T = O, F) with T−Ti−C−Ti−C−Ti−T structure was demonstrated as an efficient NRR electrocatalyst. As revealed in DFT calculations, the N_2 molecules were preferably interacted with the middle Ti on the edge plane, achieving low energy barriers (0.64 eV in $*N_2 \rightarrow *NNH$ and 0.52 eV in $*NNH \rightarrow *NNH_2$) for NH_3 formation (Figure 9a). Unfavorably, higher energy barriers of 0.85 and 0.95 eV were required on the basal plane terminated with oxygens. Treated in the LiF-HCl solution, the Al from Ti_3AlC_2 particles was successfully extracted, resulting in a reduced interaction between formed $Ti_3C_2T_x$ layers. To achieve the maximized exposure of edge sites, ultrathin $Ti_3C_2T_x$ NSs (~1.5 nm in thickness) with smaller sizes were acquired with a further sonication-assisted exfoliation (Figure 9b). When applying a vertically aligned FeOOH with sluggish activity toward HER to host $Ti_3C_2T_x$ NSs, a high FE of 5.78% was observed at −0.2 V (vs RHE) for NH_3 synthesis (Figure 9c).

Analogously, the edges of MoS_2 were demonstrated as the critical sites to polarize and activate the N_2 molecules, while the basal plane was inert for NRR.[139] The positively charged Mo-edge facilitated the formation of the Mo−N bond and significantly elongated the N/N bond length from 1.129 Å in $*N_2$ to 1.221 Å in $*NNH$ (Figure 9d). As confirmed in the free-energy profile (Figure 9e), a lower barrier of 0.68 eV was estimated in the potential-determining step (PDS) of the protonation of adsorbed N_2 ($*NN \rightarrow *NNH$), compared with those of flat surfaces on the common metals (usually 1−1.5 eV). The favorable barrier in the PDS observed on the Mo-edge enabled MoS_2 a potential catalyst toward NRR, achieving a FE of 1.17% with NH_3 yield rate of 80.8 pmol s^{-1} cm^{-2} at −0.5 V (vs RHE). More importantly, the designed catalyst exhibited an excellent stability, showing no obvious changes in the yield rate and FE within successive 10 times tests (Figure 9f). These pioneering investigations elucidate the significance of edge sites in the improvement of the activity for NH_3 synthesis. The edge engineering strategy can be readily extended to other 2D catalysts to regulate their catalytic properties, opening a new opportunity to design promising catalysts for high-performance N_2 reduction at ambient conditions.

4. STRUCTURAL MANIPULATION

4.1. Single-Atom Site. In view of the size of catalysts, numerous metal nanoparticles/nanoclusters/nanocrystals and metal-oxide quantum dots (QDs) have been synthesized for NRR applications. For instance, utilizing the special interaction between the N 2p orbitals and the Bi 6p band, an ultrahigh NH_3 yield rate of 200 mmol h^{-1} g^{-1} with an impressive FE of 66% was obtained on the Bi nanocrystal catalyst in a high concentration K^+ electrolyte, which stabilized key N_2 reduction intermediates and regulated proton transfer.[140] Besides, on account of the unique property of balanced hydrogen evolution and the reduced free-energy barrier for the rate-limiting step (N_2 hydrogenation to $*N_2H$) following the Grotthuss-like hydride transfer mechanism on α-PdH, an efficient NRR catalyst of Pd nanoparticles (NPs) was proposed for the N_2 reduction in phosphate buffer solution (PBS).[141] The prepared catalyst displayed an excellent activity with the NH_3 yield rate of ~4.5 μg h^{-1} mg_{Pd}^{-1} and a FE of 8.2% at 0.1 V (vs RHE), outperforming other catalysts of Au and Pt NPs. Compared with the large nanoparticles, quantum dots with smaller sizes could provide larger specific area and sufficient active sites to facilitate N_2 adsorption and reduction. Via a universal self-propagating combustion approach, Chu et al. reported several quantum-dot-based electrocatalysts (e.g., CoO QDs and SnO_2 QDs modified reduced graphene oxide) for highly efficient N_2 reduction.[142,143] As a paradigm, benefiting from the homogeneously anchored CoO QDs with considerable exposed catalytic sites, superior NRR activities with significantly enhanced NH_3 yield rate (21.5 μg h^{-1} mg^{-1}, over 2-fold than that of CoO NPs) and a high FE (8.3%) were achieved.

At present, most advanced electrocatalytic systems heavily rely on the utilization of noble-metal based catalysts.[144,145] For NRR by mentioned solid nanoparticles, the catalytic reactions only occur on the outer surface with limited active sites. Improving their utilization efficiency is an attractive approach to reduce the metal consumption, which is critically important for lowering the catalyst cost, improving the available active atoms and promoting sustainability.[146] In the past few years, increasing studies have been focusing on the catalyst preparation with smaller dimensions from the nanoparticle, subnanosized cluster to single-atom (SA).[147] Ascribed to their maximized atom utilization efficiency, unsaturated active sites and unique size quantum effect, single-atom catalysts (SACs) have received particular interests and emerged as the most attractive candidates in heterogeneous catalytic reactions.[148−152] With isolated metal atoms dispersed on different
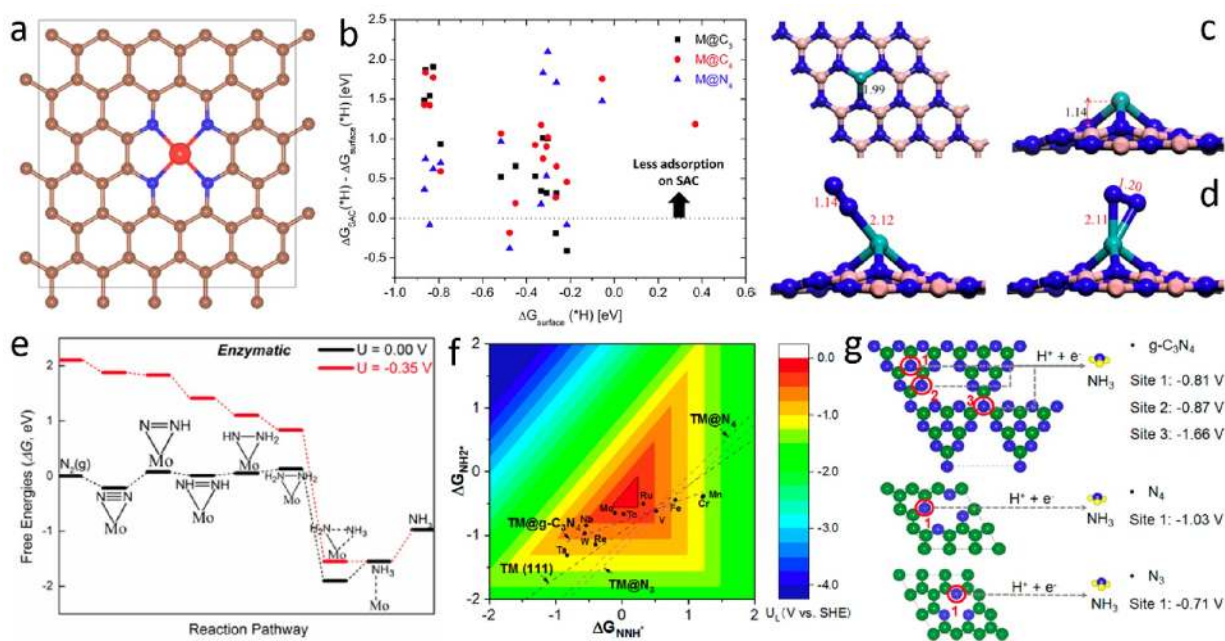
Figure 10. (a) M@N_4 calculation model for SACs. (b) Difference between H adsorption free energy on the SAC (ΔG_{SAC}(*H)) and on the metal surface ($\Delta G_{surface}$(*H)). Reproduced with permission from ref 155. Copyright 2018 American Chemical Society. (c) Optimized structure of Mo@ BN with a bond length of Å. (d) End-on and side-on configurations of N_2 adsorption on Mo@BN with bond length of Å. (e) Free-energy diagrams for the NRR on Mo@BN via the enzymatic mechanism. Reproduced with permission from ref 158. Copyright 2017 American Chemical Society. (f) The color contour plots of the limiting potential vs ΔG_{NNH*} and ΔG_{NH_2*}. (g) Decomposition energies of N-containing supports. Reproduced with permission from ref 160. Copyright 2019 American Chemical Society.

supports, SACs exhibit remarkably boosted catalytic activity compared with conventional catalysts.

To date, a mass of theoretical models of SACs have been initially studied for NRR procedures.[153,154] For example, on account of the electronic effects and the lack of ensemble effects, Jung et al. proposed that SAs anchored on defective graphene derivatives could be acted as promising NRR catalysts by DFT calculations (Figure 10a).[155] The H adsorption was sufficiently suppressed on SACs, in view of that ΔG_{SAC}(*H) − $\Delta G_{surface}$(*H) was positive for most metals and highly delocalized in the positive region (Figure 10b). Among a series of SACs, Ti@N_4 (0.69 eV) and V@N_4 (0.87 eV) with lower free energies were recommended, ascribed to an intensive back-bonding within the hybridized d-orbital metal atom and the π* orbital in *N_2. Notably, the metal/ support interaction was confirmed to play an important role in heterogeneous catalysis, via altering the charge densities on SAs and further affecting the binding affinity toward N_2. It suggested that both suitable SAs and an appropriate support were necessary to obtain satisfactory SACs.

Apart from the graphene, some other experimentally available 2D materials (e.g., MoSSe,[156] MoS_2,[157] boron nitride (BN),[158] and g-C_3N_4[159]) were also employed as supports for theoretical calculations because of their unique properties of large specific area, excellent mechanical, and thermal stability. Comparably, the catalytic activity of a series of SAs toward N_2 fixation was explored on BN monolayer and g-C_3N_4. For the BN, the anchored Mo SAs with a newly formed Mo−N_3 moiety exhibited the superior activity toward N_2 fixation (Figure 10c).[158] Two configurations of end-on and side-on were energetically favorable for NRR via the formation of Mo− N bonds (Figure 10d), in which the N/N bond length in the side-on was significantly elongated to be 1.20 Å compared with

that of end-on configuration (1.14 Å). Following the associative enzymatic mechanism, a smaller energy barrier of 0.35 eV for the protonation step (NH_2* + H^+ + e^- ↔ NH_3*) and a lower overpotential (0.19 V) were calculated (Figure 10e), demonstrating that the anchored Mo atom on the BN monolayer was a very promising SAC for the NRR. While following the distal pathway, Ru instead of Mo on the g-C_3N_4 near to the ideal region was predicted to be the most promising candidate for NRR (Figure 10f), with a more positive limiting potential (−0.33 V) and an enhanced NRR selectivity.[160] Furthermore, the durability investigation of N-containing supports was first taken into consideration to avoid risks of contaminations from the support decomposition. With a decomposition potential of −0.81 V (vs SHE) observed on the relatively stable g-C_3N_4 (Figure 10g), the desired SACs should possess more positive limiting potentials for reliable tests. These evidence not only provide a solid theoretical guidance on future development and preparation of SACs for NRR, but reveal the importance of selecting proper substrates for anchoring SAs.

In experimental progress, numerous achievements have been observed in the fabrication of various SACs, mainly focused on the noble-metal atoms of Ru@nitrogen-doped carbon (NC),[161] Ru@ZrO_2/NC,[162] Au@NPC,[163] and Au@g-C_3N_4,[164] and the rare-metal atom of Mo@NPC,[165] and Mo@PCN.[166] For example, Zeng and Si et al. prepared the Ru@NC via pyrolyzing the Ru-containing derivative of ZIF-8, and isolated Ru atoms were highly dispersed on NC via the formation of Ru−N bonds.[161] In addition to the abundant active sites provided with Ru SAs, it was also demonstrated that Ru@NC exhibited a stronger affinity toward N_2 compared with that of Ru NPs/NC, thus remarkably improving both the activity and selectivity in NRR. Impressively, an ultrahigh FE of
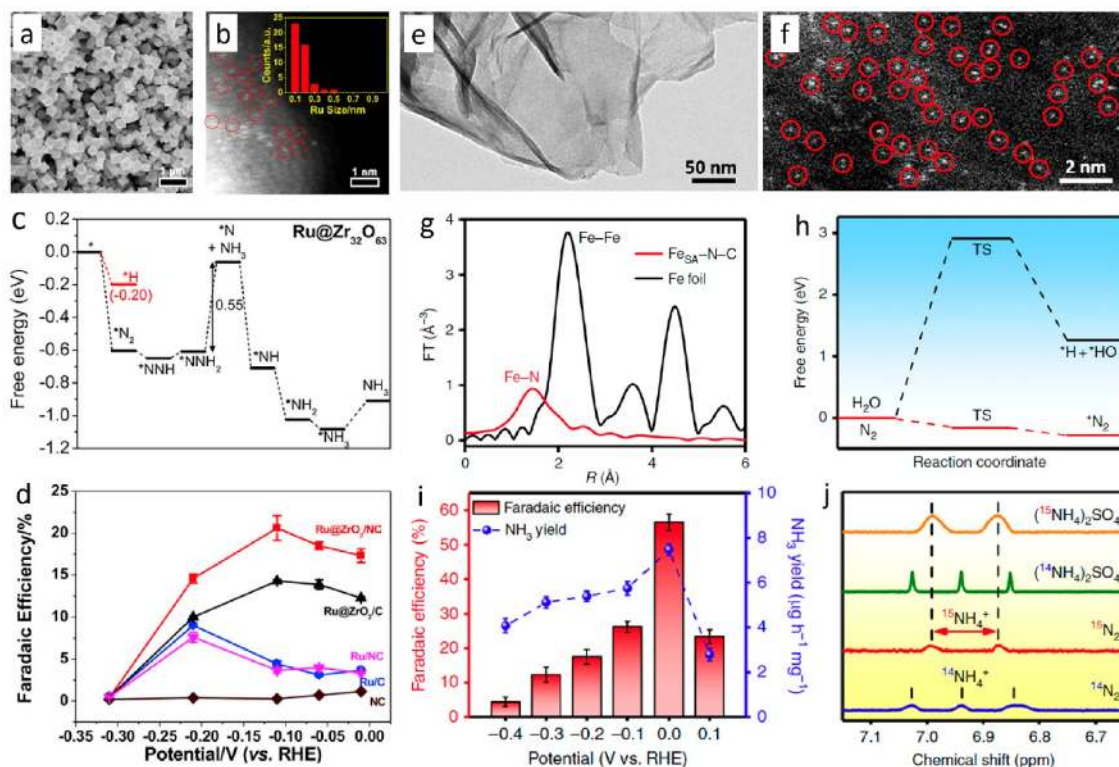
Figure 11. (a) SEM, and (b) HAADF-STEM images of Ru@ZrO$_2$/NC. (c) Free-energy diagram on Ru@Zr$_{32}$O$_{63}$ for NRR. (d) The FEs of different catalysts. Reproduced with permission from ref 162. Copyright 2018 Elsevier. (e) TEM and (f) HAADF-STEM images of Fe@NC catalyst. (g) Fourier transform spectra at the Fe K-edge of Fe@NC and Fe foil. (h) Calculated energy barriers of the adsorption of hydrogen and nitrogen. (i) FEs and NH$_3$ yield rates of Fe@NC at given potentials. (j) Isotope labeling experiments with ^{14}N$_2$ and ^{15}N$_2$. Reproduced with permission from ref 173. Copyright 2019 Springer Nature.

29.6% with an impressive NH$_3$ yield rate of 120.9 μg h^{-1} mg^{-1} was realized on Ru@NC at −0.2 V (vs RHE). Similarly, utilizing UiO-66-NH$_2$ as the hosting matrix, Sun and co-workers reported novel NRR catalysts of Ru@NC and Ru@ZrO$_2$/NC prepared via a coordination-assisted strategy.[162] The abundant −NH$_2$ in organic ligands effectively stabilized Ru precursor and inhibited Ru assembling during pyrolysis. Retaining the pristine octahedron morphology (Figure 11a), the obtained Ru@ZrO$_2$/NC displayed uniform distribution of single Ru sites (0.1−0.2 nm) on the NC (Figure 11b), accompanying with the OV-enriched ZrO$_2$ as the byproduct. Playing an indispensable role in efficient NRR, the Ru@NC$_2$ sites were theoretically confirmed as the active centers of Ru@NC and Ru@ZrO$_2$/NC. More importantly, serving as a promising catalyst support and promoter, as well as the active specie, ZrO$_2$ induced synergy has widely contributed to the exceptional performance in the many catalysis applications (e.g., CRR), due to its versatile properties and weak hydrophilic character.[167,168] As demonstrated in DFT calculations, the H adsorption was significantly suppressed on Ru@Zr$_{32}$O$_{63}$ with a lower free-energy change (ΔG(*H) = −0.20 eV) (Figure 11c), and a smaller difference of ΔG(*N$_2$) − ΔG(*H) (−0.40 eV) indicated a favorable N$_2$ adsorption on Ru@Zr$_{32}$O$_{63}$. Accordingly, an ultrahigh NH$_3$ production rate up to 3.665 mg h^{-1} mg$_{Ru}^{-1}$ was achieved on the Ru@NC at −0.21 V (vs RHE), while the presence of ZrO$_2$ remarkably enhanced the FE (~21%) on Ru@ZrO$_2$/NC at a low potential of −0.11 V (vs RHE, Figure 11d). As for Au based SACs, a Au@g-C$_3$N$_4$ catalyst with the +1 valent Au homogeneously dispersed on g-C$_3$N$_4$ NSs was reported to catalyze the N$_2$

reduction under ambient conditions.[164] Following a favorable alternating mechanism, a lower free-energy change (ΔG = 1.33 eV) in the rate-determining step (N$_2$ reduction to *NNH) was estimated on the designed catalyst, showing a better catalytic performance over Au (211) with a higher ΔG of 2.01 eV. Benefiting from atomically dispersed Au SAs, an impressive NH$_3$ yield rate of 1,305 μg h^{-1} mg$_{Au}^{-1}$ was achieved with a FE of 11.1%. Compared with the performance of Ru NPs (NH$_3$ yield rate of 5.5 mg h^{-1} m^{-2}, FE of ~5.4%) and Au subnanoclusters (NH$_3$ yield rate of 21.4 μg h^{-1} mg^{-1}, FE of ~8.11%),[169,170] the significantly enhanced yield rates or FEs confirmed that SACs could not only utmost utilize the available sites of catalyst but also improve the conversion selectivity.

Besides noble-metal and rare-metal based SACs, earth-abundant Fe- and Cu-based SACs have also received great attention in the catalytic N$_2$ reduction.[171,172] For instance, a novel Fe$_{SA}$−N−C (Fe@NC) catalyst exhibited an impressive conversion efficiency in the NH$_3$ synthesis.[173] Synthesized by the calcination of a polypyrrole-iron complex, Fe SAs (bright dots) were homogeneously isolated on the NC with a graphene-like morphology (Figure 11e,f). These Fe SAs were stabilized by N atoms with one unique peak corresponding to Fe−N scattering paths at ~1.44 Å (Figure 11g). Strikingly, the proposed Fe@NC showed a sluggish HER kinetics with a high energy barrier of 2.91 eV toward H$_2$O dissociation to produce *H (Figure 11h). While the N$_2$ adsorption exhibited a desirable exothermic process, undergoing a downhill process with the Gibbs free energy of −0.28 eV toward *N$_2$ binding. Following a more feasible alternative pathway, a favorable first

Table 2. Performance of Representative 2D Photo/Electrocatalysts in NRR

electrocatalyst	electrolyte	potential (vs RHE)	NH_3 yield rate ($\mu g\ h^{-1}\ mg^{-1}$)	FE	ref
MoO_2 NSs	0.1 M HCl	−0.15 V	12.20	8.2%	41
W_2N_3 NSs	0.1 M KOH	−0.20 V	11.66	11.67%	74
Rh NSs	0.1 M KOH	−0.20 V	23.88	0.217%	186
B NSs	0.1 M Na_2SO_4	−0.8 V	13.22	4.04%	187
B_4C NSs	0.1 M HCl	−0.75 V	26.57	15.95%	188
MoO_3 NSs	0.1 M HCl	−0.5/−0.3 V	29.43 (−0.5 V)	1.9% (−0.3 V)	189
Bi NSs	0.1 M Na_2SO_4	−0.8 V	13.23	10.46%	190
h-BN NSs	0.1 M HCl	−0.75 V	22.4	4.7%	191
black phosphorus NSs	0.01 M HCl	−0.7/−0.6 V	31.37 (−0.7 V)	5.07% (−0.6 V)	192

photocatalyst	reaction medium	scavenger	light source	NH_3 yield rate ($\mu mol\ h^{-1}\ g^{-1}$)	ref
CuCr-LDH NSs	N_2/H_2O	none	UV−vis	73.9 (UV−vis)/57.1 (vis)	23
SmOCl NSs	N_2/H_2O	none	UV−vis	426 (UV−vis)/291 (vis)	193
BiOBr NSs	N_2/H_2O	none	UV−vis	54.70 (UV−vis)/49.04 (vis)	194
Bi_3O_4Br NSs	N_2/H_2O	none	UV−vis	50.8	195

hydrogenation step and dramatically reduced overall reaction barrier were revealed. By virtue of these remarkable merits, a striking FE of 56.55% with a yield rate of 7.48 $\mu g\ h^{-1}\ mg^{-1}$ was achieved (Figure 11i), and the NH_3 generation was conclusively originated from the N_2 reduction as confirmed in ^{15}N isotope test (Figure 11j).

For Fe-based SACs, the Fe coordination states played critical roles in their NRR performance. According to the theoretical calculations, highly spin-polarized FeN_3 active center on graphene with a local magnetic moment could remarkably promote N_2 reduction than that of FeN_4, due to the facilitated N_2 adsorption and activation.[174] As a proof-of-concept paradigm, Zheng and Cui et al. proposed the Fe−N/C− carbon nanotube with favorable FeN_3 species for the electrocatalytic NRR.[175] Besides a larger spin moment of FeN_3 species (3.16 μB) than that of 1.18 μB on FeN_4, the lower free energy (ΔG = −0.75 eV) for the spontaneous chemisorption of N_2 on the FeN_3 species (∼0.35 eV on FeN_4) indicated both a high adsorption and activation ability for N_2 on FeN_3. Despite the presence of trace Fe_3C or metallic Fe species in the catalyst, both experimental explorations and theoretical calculations confirmed that FeN_3 species contributed to an effective NH_3 synthesis, achieving the high NH_3 yield rate of 34.83 $\mu g\ h^{-1}\ mg^{-1}$ with a FE of 9.28% (−0.2 V vs RHE). Nevertheless, recent studies identified that FeN_4 also acted as an efficient active center for N_2 fixation.[176,177] For instance, Liu and co-workers demonstrated homogeneously dispersed active FeN_4 sites anchored on the NPC for an efficient NRR.[176] In a neutral aqueous electrolyte of 0.1 M PBS, a high FE of 18.6% and NH_3 production rate of 62.9 $\mu g\ h^{-1}\ mg^{-1}$ were achieved at −0.4 V (vs RHE). Despite the present controversy, both FeN_3 and FeN_4 displayed excellent activities in NRR, and the FeN_4 even demonstrated a better performance than that of FeN_3. In addition to chemical coordination states of Fe atoms, other underlying factors such as supporting substrates and adopted electrolytes, should be taken into consideration in theoretical studies to more accurately estimate the overall performance of SACs. For instance, because of the nonuniformity and unpredictable defects of different supports, not all of the Fe SAs were equally available or active. Thus, future studies will need to explicitly explore the actual active centers, with the assistance of advanced theoretical approaches and characterization techniques.

In spite of the rapid development of SACs and their unique advantages in catalysis, several problems and challenges are remaining in the current study to meet the ever-increasing demand in basic research and practical applications with SACs.[178] First, some catalytic procedures occur at the surrounding support atoms instead of SAs alone. Thus, an effective characterization approach is highly required to fully reveal the true active sites in the vast majority of SACs. Second, precisely regulating the coordination environment of SAs (e.g., FeN_3 and FeN_4) is extremely desirable, which occupies a great promise to optimize and enhance the catalytic properties of SACs. Third, achieving the facile approaches and increasing the loading content of SAs are also critical challenges in the synthesis of SACs. Last, with the help of theoretical calculations, more attentions should be focused on the exploration of the structure−function relationship, as well as catalytic mechanisms at the atom-scale. Through effectively tackling these fundamental challenges, specific SACs would be rationally designed for the NRR, achieving high NH_3 yields and FEs.

4.2. Morphological Regulation. In addition to the size consideration of designed catalysts, another effective strategy to enhance the exposed active sites is the controllable regulation of desired morphologies (e.g., 1D ultrafine nano-wires/nanofibers/nanorods, 2D ultrathin nanosheets, and 3D porous/hollow structures). Among these micronano structures, 1D nanostructures have received extensive attentions in catalysis fields, owing to their unique physicochemical properties.[179] For example, 1D nanostructures could offer direct transfer pathways and facilitate electron transport. With large specific areas, they enable sufficient interactions at the interface of the N_2-electrolyte-catalyst, thus improving the interfacial mass transport. In this aspect, Sun and co-workers first demonstrated the superior performance of Nb_2O_5 nanofiber for NRR at ambient conditions.[180] With the charge exchange and transfer occurred between the Nb-edge atoms and N_2, a high polarization and activation of adsorbed N_2 molecules were realized. Accordingly, an extraordinary catalytic performance with the NH_3 yield rate of 43.6 $\mu g\ h^{-1}\ mg^{-1}$ (FE of 9.26%) was achieved at −0.55 V (vs RHE). Moreover, through in situ growth of vertically aligned arrays with such 1D nanostructures on the conductive substrates, the redundant treatments involved in the catalyst loading with ex situ prepared catalysts, such as the ultrasonic dispersion and postdropping, could be avoided.[181,182] Besides, the in situ array
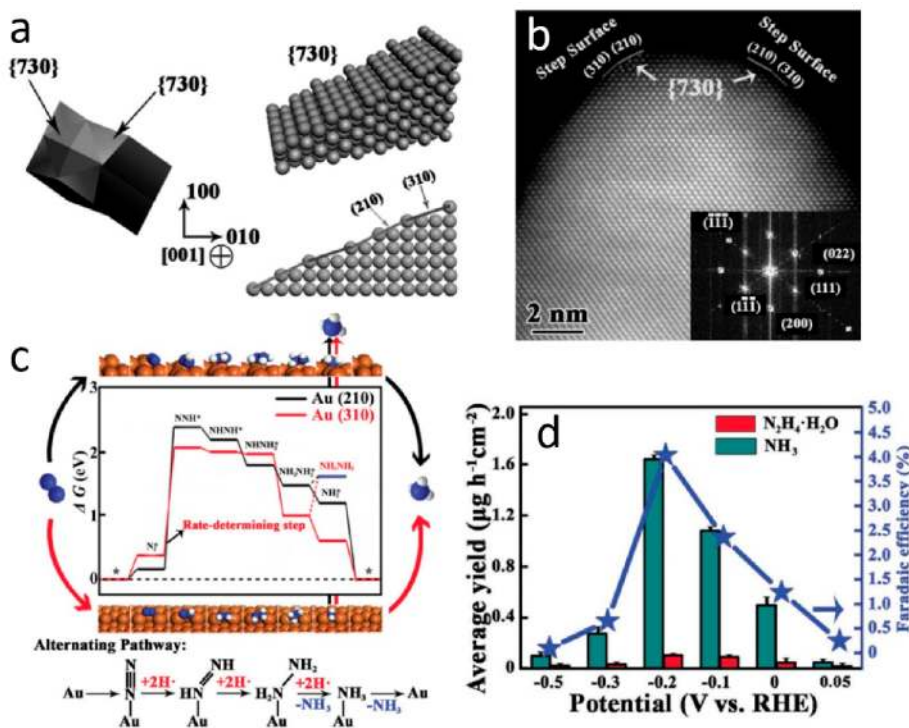
Figure 12. (a) Geometric models of the THH Au NRs with active {730} facet, consisting of subfacets of (210) and (310). (b) Spherical aberration corrected TEM image of the THH Au NRs with stepped subfacets. Inset: the fast Fourier transform pattern. (c) Free-energy diagrams and alternating pathway on Au (210) and (310) facets. (d) Yield rates of NH_3 and $N_2H_4 \cdot H_2O$ and related FEs at applied potentials. Reproduced with permission from ref 213. Copyright 2016 Wiley-VCH Verlag GmbH & Co. KGaA, Weinheim.

growth is favorable to supply more available active sites, maintain the intrinsic morphology, and enhance the binding strength on the substrates. For instance, MacFarlane et al. reported novel α-Fe nanorod arrays for NRR, which were prepared with the thermal reduction of β-FeOOH in situ grown on carbon fiber.[183] The α-Fe(110) was confirmed as the active surface for N_2 reduction, exhibiting a smaller reaction free energy ($\Delta G = 0.15$ eV) in the *N_2H formation (*N_2 + H^{+} + e[−] $\leftrightarrow$ *N_2H). Together with introducing a mixture electrolyte consisting of the aprotic fluorinated solvent and ionic liquid that effectively suppressed the HER, a substantially improved performance in the NH_3 synthesis was acquired at ambient conditions.

Compared with its counterparts, ultrathin 2D nanosheets show many unique advantages and numerous unprecedented physical, electronic, chemical, and optical properties.[184] The large lateral size with few layers endows them with ultrahigh specific area, which is extremely attractive for surface-related catalysis applications. Meanwhile, a high exposure of surface atoms makes them appropriate for surface modifications and functionalization (e.g., through element doping and vacancy engineering). As discussed before, these strategies will facilitate the N_2 adsorption and activation on the catalysts. Furthermore, the atomic thickness and robust in-plane covalent bond could achieve excellent flexibility, good mechanical strength, and optical transparency. Lastly, the distinct changes in electronic structures of 2D nanomaterials, especially in comparison with their 3D structures, would offer new opportunities to use such materials as catalysts in many chemical reactions.[185] On the basis of these merits, great efforts have been focused on the investigations of catalytic performance of 2D catalysts in the NRR (Table 2). Especially in the case of Rh NSs, its NH_3 yield

rate (23.88 μg h^{−1} mg^{−1}) was significantly enhanced compared with that of Rh NPs ($\sim$11.45 μg h^{−1} mg^{−1}), confirming the superiority of 2D ultrathin structures in NRR.[186] Despite the considerable potential in NRR catalysis, the application-oriented research in 2D nanomaterials is only just beginning. On the basis of further explorations on the catalytic behaviors of 2D nanomaterials and coupling with the development of advanced preparation technology for mass production, the researchers would be able to provide new directions of these materials in the catalytic N_2 reduction.

As for catalysts with porous/hollow micronano structures, several advantages are highly anticipated in their favorable roles in expediting N_2 reduction rate and efficiency. For instance, the porous/hollow structures could accelerate the diffusion and transfer of the reactants and provide highly active areas at inner and outer surfaces.[196,197] Meanwhile, owing to the cage effect, the reaction intermediates could be confined in the hollow cavity, increasing the steady-state concentrations of pivotal intermediates in rate-determining steps.[198] Further-more, avoiding the excessive coverage of capping agents on the outer surface, the less-capped inner surface might be more active for N_2 reduction. As a paradigm, Au nanomaterials with different morphologies (e.g., Au hollow nanocages, nanorods, nanocubes, and nanospheres) were tested for evaluating their NRR performance under ambient conditions.[199] Compared with a high NH_3 production rate of 3.9 μg h^{−1} cm^{−2} (-0.5 V vs RHE) and an impressive FE of 30.2% (-0.4 V vs RHE) obtained on the Au nanocages, significantly reduced yield rates and FEs were observed on other morphologies, demonstrating the advantages of porous/hollow structures in the NRR. To reveal structure−activity interdependency, further explorations on the inner Ag content, pore size/density, and available
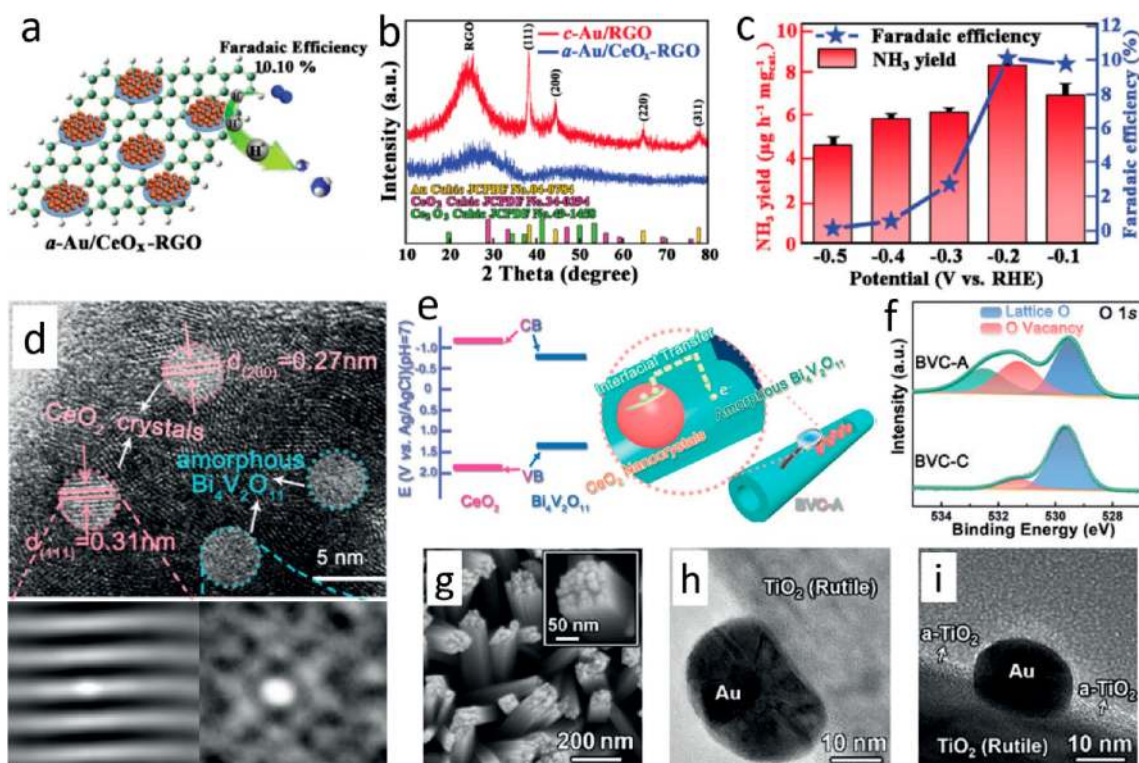
Figure 13. (a) Schematic illustration for the electrocatalytic N_2 reduction by a-Au/CeO$_x$-RGO. (b) XRD patterns of prepared a-Au/CeO$_x$-RGO and c-Au/RGO. (c) NH$_3$ yield rates and related FEs at given potentials. Reproduced with permission from ref 220. Copyright 2017 Wiley-VCH Verlag GmbH & Co. KGaA, Weinheim. (d) HRTEM image and corresponding autocorrelation images of BVC-A. (e) Band alignment of Bi$_4$V$_2$O$_{11}$ and CeO$_2$, and illustrated interfacial charge migration. (f) XPS spectra of BVC-A and BVC-C. Reproduced with permission from ref 223. Copyright 2018 Wiley-VCH Verlag GmbH & Co. KGaA, Weinheim. (g) SEM images of TiO$_2$ nanorods. HRTEM images of (h) Au-TiO$_2$ and (i) a-TiO$_2$/Au-TiO$_2$. Reproduced with permission from ref 224. Copyright 2018 Wiley-VCH Verlag GmbH & Co. KGaA, Weinheim.

surface area of Au nanocages were performed.[200] Playing a favorable role in HER, the presence of Ag in the cavity reduced the NRR activity. Meanwhile, increasing the pore size was not beneficial for enhancing the NH$_3$ yield rates and FEs, on account of the adversely reduced active surface area, as well as an inefficient confinement of reactants in the hollow cavity. Apart from the noble-metal catalysts, noble-metal-free electrocatalysts with porous/hollow structures, such as Cr$_2$O$_3$ microspheres and CoP nanocages, also showed impressive activities in NRR.[201,202] For instance, owing to the charge transfer from Co to P on the steeped surface of CoP nanocages, dissolved N$_2$ was captured on the positively charged Co sites.[202] Meanwhile, protons from H$_2$O were anchored on negatively charged P sites, resulting in the generation of stable N—H bonds and eventual breakage of N≡N bonds. Designed hollow CoP nanocages exhibited exciting performance with a high FE of 7.36% (0 V vs RHE) and NH$_3$ production rate of 10.78 μg h^{-1} mg^{-1} (−0.4 V vs RHE). In spite of significant superiority achieved on the porous/hollow catalysts in NRR applications, there are still many issues. On the one hand, it is challenging to prepare porous/hollow structures with desired structural and compositional complexity. For example, hollow structures with ultrathin shells are highly required to provide tremendous inner space and abundant active sites, which are usually important for catalysis and energy storage.[203] On the other hand, to meet the great demands for practical applications, future investigations should pay more attention to several aspects, such as the synthesis method, production cost, and safety issues. Although most of the present methods involving various hard and soft templates

have been proven to be very useful for preparing porous/hollow structures, direct synthesis with template-free or self-template methods is more preferred, because of the significantly reduced production cost and the ease of large-scale production.[204]

5. CRYSTALLOGRAPHIC TAILORING

5.1. Crystal Facet Control. Through precisely and rationally exposing specific facets, the manipulation of crystals with desired faces at the atom-scale is crucial for enhancing their catalytic performances.[205] Such crystal facet effect inherently results from the atomic arrangement on different exposed crystal facets. In this regard, high-quality anatase TiO$_2$ single-crystal dominated by active {001} facets, BiOCl NSs with (001) facets, Pt nanocrystals having {411} facets, and octahedral Pd NPs dominated by Pd(111) facets displayed outstanding photo/electrocatalytic activities.[206−209] As revealed in previous theoretical studies, favorable active sites on catalysts mostly existed on the stepped facets instead of flat terraces,[210] and different selectivity limitations in N$_2$ reduction were also observed on the (111) and (211) facets.[211] Using these trends and predictions, a new strategy of crystal facet engineering is introduced for guiding the NRR catalyst design with specific facets.

To this end, several paradigms focusing on the Mo-(110) nanofilm, tetrahexahedral gold-{730} nanorods (THH Au NRs), and Bi$_5$O$_7$I-{001} NSs were reported for NRR tests.[212−214] For instance, using THH Au NRs enclosed by multifaceted surfaces, Yan et al. demonstrated a feasible electrocatalytic NRR at ambient conditions (Figure 12a).[213]

Composed of the active (210) and (310) subfacets (Figure 12b), the multistep facet of {730} significantly facilitated the proceeding of NRR. As demonstrated in DFT calculations, N_2 was preferentially adsorbed on stepped facets on the basis of the unsaturated coordination, resulting in the formation of Au−N bonds (Figure 12c). The subsequent generation of stable N−H with the activated H effectively broke the N≡N bonds. Following the alternating pathway on THH Au NRs, both NH_3 and $N_2H_4·H_2O$ were simultaneously observed after NRR, achieving average production rates of 1.648 and 0.102 $\mu g\ h^{-1}\ cm^{-2}$, respectively (Figure 12d).

Previous investigations have widely demonstrated that BiOX exposed with {001} facets possessed an excellent photoactivity.[215,216] Enlighted by these discoveries, a recent study explored the facet-dependent photocatalytic performance of Bi_5O_7I NSs for N_2 fixation.[214] Bi_5O_7I NSs with different dominant exposure of {100} and {001} facets (Bi_5O_7I-100 and Bi_5O_7I-001) were controllably fabricated with hydrolysis and calcination methods. Ascribed to a more negative CB position with a higher reduction ability and a facilitated separation efficiency of the photoinduced carriers, Bi_5O_7I-001 exhibited a higher activity for N_2 fixation than Bi_5O_7I-100. Upon the light irradiation at 365 nm, a high AQE of 5.1% was realized on Bi_5O_7I-001, which was ∼2.2 times larger than that of Bi_5O_7I-100 (∼2.3%). Undoubtedly, crystal facet engineering not only sheds light on deeper explorations toward the relationship of surface property−catalytic performance but also offers more opportunities to develop and prepare highly active catalysts.

5.2. Amorphous Engineering. With respect to their crystalline counterparts, amorphous nanomaterials with disordered atomic arrangement possess a greater number of active sites due to the "dangling bonds" in amorphous phases, and have received much attentions in oxygen evolution reaction (OER) and HER applications.[217−219] It was also observed that amorphous catalysts with unsaturated coordination sites could significantly improve the NRR activity under ambient conditions.

For instance, Yan et al. first reported amorphous Au NPs anchored on bisubstrate of CeO_x-reduced graphene oxide (a-Au/CeO_x-RGO) for the electrocatalytic N_2 reduction (Figure 13a).[220] On the one hand, 2D RGO sheets facilitated the homogeneous dispersion of nanoparticles, improved the metallic utilization and avoided the aggregation due to the high surface energy. On the other hand, the incorporation of CeO_x into the crystalline structure of Au, as well as the strain around $Ce^{3+/4+}$ sites induced the disorder of Au, transforming the crystalline Au (c-Au) into the amorphous phase (Figure 13b). As anticipated, the prepared hybrid catalyst achieved a higher FE (10.10%, 3.67% of c-Au/RGO) and NH_3 yield rate (8.3 $\mu g\ h^{-1}\ mg^{-1}$, 3.5 $\mu g\ h^{-1}\ mg^{-1}$ of c-Au/RGO) at −0.2 V (vs RHE, Figure 13c). Furthermore, the same group reported an amorphous PdCu nanocluster dispersed on RGO for NRR.[221] The introduction of Cu not only accelerated the hydrogen desorption on the metal surface thus effectively suppressing the HER but also altered the electronic structures of bimetallic components.[222] Coupling with RGO as a support for ultrafine nanocluster dispersion and continuous pathway for rapid electron transfer, the prepared a-$Pd_{0.2}Cu_{0.8}$/RGO catalyst showed an improved NH_3 yield rate of 2.80 $\mu g\ h^{-1}\ mg^{-1}$ (−0.2 V vs RHE), which was much higher than Pd/RGO (1.34 $\mu g\ h^{-1}\ mg^{-1}$) and Cu/RGO (1.17 $\mu g\ h^{-1}\ mg^{-1}$).

Although exhibiting an energetic efficiency for NRR, the low abundance and high cost of noble Au or Pd would greatly restrict the large-scale applications of such heterogeneous catalysts. To address this problem, Chen and Yu et al. designed a noble-metal free hybrid catalyst of $Bi_4V_2O_{11}$/CeO_2 with amorphous $Bi_4V_2O_{11}$ (BVC-A) for electrocatalytic NRR (Figure 13d).[223] With a similar function in the preparation of a-Au, the introduction of CeO_2 nanocrystals retarded the heat transfer thus inducing the amorphization of $Bi_4V_2O_{11}$. Besides, the presence of CeO_2 established the band alignment with $Bi_4V_2O_{11}$ to realize a prompt interfacial charge transfer (Figure 13e). Compared with its crystalline counterpart (BVC-C), abundant OVs were simultaneously introduced with removing oxygen ions from $[VO_{3.5}]^{2-}$ layers in the amorphization process, as verified by the increased peak intensity in O 1s XPS spectra (Figure 13f). Attributed to these merits, localized electrons in BVC-A were enhanced for π-back-donation, contributing to an efficient N_2 activation and N≡N cleavage. Remarkably, BVC-A showed outstanding NRR performance, with a high NH_3 formation rate of 23.21 $\mu g\ h^{-1}\ mg^{-1}$ and FE of 10.16% at ambient conditions.

Comparably, another promising amorphous catalyst of SmOCl NSs was proposed for the photocatalytic N_2 reduction recently.[193] Accompanying with the amorphization, sufficient OVs were successfully engineered into the nanosheets, substantially facilitating the chemisorption and activation of N_2 molecules. Moreover, the observed Sm−O covalency with an enhanced intensity demonstrated a favorable electron migration from active sites to the surface bound N_2. On account of the attractive synergistic effect, an excellent photocatalytic activity was realized on the amorphous SmOCl NSs, achieving an impressive NH_3 formation rate of 426 $\mu mol\ h^{-1}\ g^{-1}$ under light irradiation and an AQE of 0.32% at 420 nm.

In spite of the prominent property of amorphous phase in the enhancement of NRR performance, challenges still remain to controllably and precisely prepare the amorphous phase without affecting bulk properties. To address this issue, Gong et al. described a fine-tuning on a thin layer of amorphous TiO_2 (a-TiO_2) on the plasmon-enhanced Au-TiO_2 nanorods (Figure 13g−i), utilizing the atomic layer deposition (ALD) technique.[224] ALD has been extensively applied as an efficient technique for depositing thin films.[225,226] It is regarded as a precise approach that meets the needs for atomic layer control at the Angstrom.[227] Meanwhile, the conformal deposition through the sequential and self-limiting reactions of ALD enables a satisfactory step coverage especially on high-aspect-ratio structures, such as arrays of nanorods, nanowires, and nanotubes. Along with the formation of a-TiO_2, abundant OVs were uniformly deposited onto the surface of hybrid catalyst. As well-known, the surface OVs are extremely desirable for the catalysis, while bulk vacancies serving as carrier traps are detrimental for the charge separation. Accordingly, the NH_3 production rate on a-TiO_2/Au-TiO_2 electrode was synergistically enhanced, achieving a yield rate of 13.4 $nmol\ h^{-1}\ cm^{-2}$ (∼2.6 times that of bare TiO_2).

Amorphization induces several excellent properties into the designed NRR catalysts, realizing enhanced conversion efficiency in NH_3 production. Nevertheless, there is much advancement needed for improving catalyst performance through amorphous engineering. Easily suffering from chemical corrosion, the poor chemical stability of amorphous materials severely hinders their further development. In particular, long-term stability is a key indicator for evaluating the potency of designed catalysts in real applications.

Meanwhile, there is still a lack of depth in the mechanistic investigation on amorphous catalysts at an atomic level, which in turn could provide theoretical instructions on the fabrication of proper catalysts. Moreover, considering the high operation cost of ALD, developing new and facile approaches to fabricate amorphous structures is tremendously required in the near future.

6. INTERFACE REGULATION

To improve the competitiveness of the NRR over HER, another attractive strategy for catalyst design is the interface regulation, which is dedicated to effectively mitigating H_2O splitting, while simultaneously promoting interactions between solid catalysts and N_2 molecules. Via controlling the hydrophobic/hydrophilic or anaerobic/aerophilic properties of catalysts, the manageable interactions among gas/electrolyte/catalyst could be rationally regulated at the interfaces, achieving superior performances in CRR and ORR.[228−230] Lately, a qualitative calculation model of electrochemical NRR with approximate production rates of NH_3 (r_N) and H_2 (r_H) was proposed by Nørskov et al.[231] It was revealed that r_N was first-order in surface N_2 concentration, while r_H was first-order in both the proton and electron concentrations. Accordingly, reducing the availability of electrons or protons, while increasing the N_2 solubility was regarded as an efficient strategy to substantially enhance the NH_3 selectivity.

These pioneering studies stimulate greater interests toward developing novel NRR catalysts with interface engineering. In view of this point, Ling et al. first reported a promising NRR system, via introducing a hydrophobic functional layer to inhibit the HER and improve N_2/catalyst interactions.[232] Possessing the merits of superhydrophobicity and high gas adsorption capacity, zeolitic imidazolate framework-71 (ZIF-71) layer with a thickness of ∼320 nm was homogeneously coated on Ag nanocubes (∼120 nm) modified Au substrate (Ag−Au@ZIF). This ingenious configuration not only inhibited the access of H_2O but also enriched N_2 concentrations toward encapsulated Ag active sites. Tested in the organic electrolyte containing the ethanol as the proton source, N_2 was effectively reduced at the interface with an obvious reduction peak, which was absent in Ar atmosphere. On the advantage of this exquisite interfacial design, significantly boosted average NH_3 generation rate (∼10 pmol s^{-1} cm^{-2}, 4-fold that of Ag−Au) and FE (∼18%, 2-fold that of Ag−Au) were achieved on the Ag−Au@ZIF, as well as an excellent selectivity toward NRR (∼90%, 14-fold that of Ag−Au).

Considering H_2O is the frequently used solvent and environmentally friendly source of protons, developing a water-based NRR system is of critical importance in practical applications. For this purpose, an attractive aerophilic−hydrophilic interface of Si-based photocathode catalyst was proposed for N_2 reduction.[233] The functional interface was composed of Si coated with a thin Ti layer (TS), poly-(tetrafluoroethylene) (PTFE) framework, and deposited Au NPs (Au-PTFE/TS, Figure 14a). The Au NPs with diameters around 2−10 nm were homogeneously dispersed on the 3D porous PTFE structure (Figure 14b). On the one hand, the hydrophobic PTFE could significantly accelerate the N_2-diffusion process based on a gas molecular-concentrating effect. Accordingly, a smaller contact angle of gas-bubble (CA$_g$, ∼ 88°) was observed on the Au-PTFE/TS surface (Figure 14c), in stark contrast to a high CA$_g$ of ∼111° on Au/TS
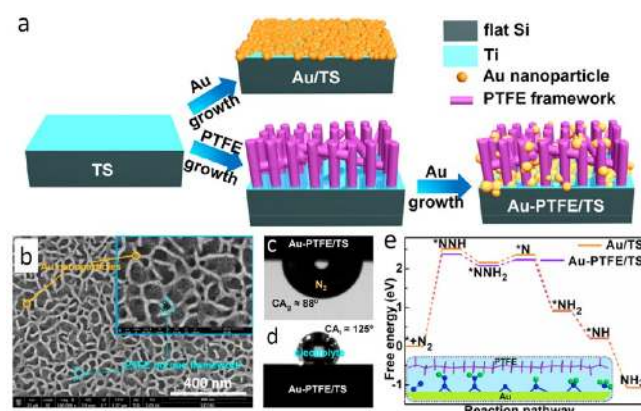

Figure 14. (a) Schematic illustration of the preparation process of Au-PTFE/TS. (b) Top view FESEM images of Au-PTFE/TS. Shapes of (c) N_2 bubble and (d) liquid on the surface of Au-PTFE/TS. (e) Free-energy profile of NRR on Au/TS and Au-PTFE/TS. Reproduced with permission from ref 233. Copyright 2018 Elsevier.

surface. On the other hand, free-stacked Au NPs highly dispersed on the PTFE framework not only provided an intimate connection for electron transport but also improved the hydrophilic property of the interface. Compared with a higher liquid contact angle of pure PTFE/TS (CA$_l$, ∼ 133°), a slightly reduced CA$_l$ of ∼125° on Au-PTFE/TS ensured the proton supply for N_2 reduction (Figure 14d). Attributed to the unique aerophilic−hydrophilic interface of Au-PTFE/TS, a smaller free-energy change (ΔG = 2.37 eV) was achieved in the rate-determining step of N_2 hydrogenation to *NNH (2.52 eV on Au/TS, Figure 14e), implying a facile generation of *NNH on Au-PTFE/TS. On account of the synergetic effect, a high NH_3 yield rate of 18.9 μg h^{-1} cm^{-2} with a significantly enhanced FE of 37.8% was achieved on Au-PTEE at −0.2 V (vs RHE).

Via deliberately designing the hydrophobic/hydrophilic or anaerobic/aerophilic interfaces, originally unfavored NRR processes exhibited impressive competitiveness over dominant HER. Inspired by these innovative discoveries, desirable catalytic interfaces for water-sensitive reactions (such as NRR), could be rationally established, even with intrinsically active catalysts widely employed in HER (e.g., Ag nanocubes).

7. SUMMARY AND PERSPECTIVES

The great achievements in NRR have demonstrated the feasibility of catalytic N_2 reduction on heterogeneous catalyst surfaces under ambient conditions. To substantially improve the energy utilization efficiency and suppress hydrogen evolution (the major side reaction competing for protons and electrons), versatile strategies for rational catalyst design have been extensively introduced to improve the NRR performance. Despite the remarkable progress observed in the field, the research in this area is still faced with some fundamental challenges, and tremendous efforts are required to realize catalytic NH_3 production at practical levels.

7.1. Insights into N_2 Reduction Mechanisms and Pathways. Theoretical simulations and calculations have been demonstrated as powerful approaches to investigate the underlying reaction mechanisms and pathways, which in turn open attractive avenues for the rational design of promising catalysts. On the strength of theoretical explorations, the potential active sites of catalysts, free-energy changes of rate-

limiting steps, and possible reaction pathways accompanying with lower onset potentials or energy barriers could be efficiently revealed. Nevertheless, present computational studies still encounter several limitations, such as the available theoretical method, model accuracy, and computational strategy. For instance, (i) the electron transfer in the N_2 reduction processes may follow different pathways, such as the concerted/sequential proton–electron transfer (CPET/SPET). Playing a critical role in predicting the thermodynamics of CPET steps, the widely employed computational hydrogen electrode (CHE) methodology could not account for the SPET pathway.[234] Therefore, it is highly demanded to establish novel theoretical methods to describe possible SPET pathways. (ii) Meanwhile, the simplified models are generally adopted in the theoretical explorations, while the imperative considerations into the medium effects (e.g., pH, temperature, proton source, N_2 transfer rate, and the cations/anions) are neglected. In view of the significance of these factors, as well as possible surface reconstruction of catalysts, novel guiding principles and models are extremely anticipated in future. (iii) Moreover, the large-scale screening of highly active catalysts usually requires huge computational resource; therefore an efficient screening strategy with simple descriptors is desirable to enhance the screening efficiency. As an attempt, a general two-step strategy was proposed for high-throughput screening of 10 promising electrocatalysts out from 540 systems for N_2 reduction, utilizing the descriptors of adsorption energy of N_2 (ΔE_{N_2}) and free-energy change of $\Delta G_{N_2-N_2H}$ to exclude low-active systems in the first step and the $\Delta G_{NH_3\text{-desorption}}$ and $\Delta G_{NH_2-NH_3}$ in the second step to seek highly active catalysts.[235]

7.2. Advanced In Situ/Operando Characterization Techniques for NRR.

To comprehensively investigate the reaction procedures under practical operation conditions, it is far from enough to probe the catalytic behaviors only based on the theoretical calculations. As well-known, the reconstruction of the surface structure, the changes in element valence state, and the exposed active centers are difficult to be accurately predicted by the theoretical simulations. For this sake, the development of advanced characterizations, especially in situ/operando techniques, is of critical importance to monitor the transformations of reactive intermediates and changes in textural properties on the catalyst surface. For instance, in situ DRIFTS and quasi in situ XPS measurements have been gradually introduced for the determination of reaction intermediates, as well as their interactions with catalysts in the NRR.[119,193] Extensively applied for the direct observation of critical reaction intermediates in many catalytic reactions, the surface-enhanced infrared absorption spectroscopy (SEIRAS) and high-resolution electron energy loss spectroscopy (HREELS) also hold great potentials for the deeper understanding of NRR pathways because of the high surface sensitivities.[236,237] Recently, in situ SEIRAS was successfully employed to explore N_2 reduction mechanisms on Au and Ru surfaces by Shao et al.[238,239] For instance, with the confirmation of N_2H_y species, an associative reaction mechanism was established on the Au surface, and N≡N bond tended to break simultaneously in the hydrogenation, offering new routes for exploring the underlying mechanisms on metal surfaces.

Considering the potential variations of the local environment, electronic property, and structural information on catalysts under reaction conditions, it is highly demanded to

reveal the critical active phase formation and transformation in NRR with in situ monitoring techniques, such as the in situ XRD and XAS widely performed in the CRR.[240,241] Recently, Yan et al. observed the crystallinity change on the catalyst from crystalline to amorphous phase associated with the NRR via in situ XRD characterization.[242]

Through the efficient combination of theoretical calculations and experimental observations, deeper understanding into the reaction processes and correlations between structures and performance are highly anticipated to be realized, which will enable researchers to precisely design various catalysts with significantly improved activity and selectivity.

7.3. Benchmarking Protocols for NRR Measurements.

7.3.1. Elimination of Exogenous Contaminations.
In addition to the development of versatile catalysts, the reliable experimental operations in the NRR are essential to accurately assess their performance, which are currently encountered with considerable scientific and technical challenges. For example, NH_3 is ubiquitous in the air, experimental consumables (e.g., nitrile gloves), N-containing catalysts, and even from human breath.[243] Because most reported studies only achieved low conversion efficiencies and selectivities, it is difficult to determine whether the detected NH_3 is produced in NRR or stemmed from the exogenous contaminations. In addition to the instability of the catalyst itself, the easy decomposition of common capping reagents adopted in the catalyst preparation, such as thioacetamide (TAA) and hexamethylenetetramine (HMTA), would lead to NH_3 contaminations under the irradiation.[244] Therefore, the indispensable blank/control experiments (e.g., in the Ar/$^{15}N_2$ streams) are highly recommended to confirm that the detected NH_3 is actually stemmed from the N_2 reduction.[245] Especially for the N-containing catalysts, the isotope measurements with $^{15}N_2$ are essential to tracing the N-source in the generated NH_3.

7.3.2. Reliable NH₃ Determination Approaches.
Up to now, several analysis approaches including the spectrophotometric assay, ion chromatography, ion-selective electrode, and ^{1}H NMR spectroscopy have been extensively used in the NH_3 determination. The spectrophotometric methods containing the Nessler's reagent and indophenol blue approaches are most popular because of the low cost, easy operation process, and high sensitivity. Nevertheless, the accuracy of these spectrophotometric approaches would be disturbed with several interference factors, such as the pH, ion strength, and sacrificial reagents (e.g., methanol, ethanol, and isopropanol), severely affecting the reliability of the reporting data. To this end, other quantitative methods, such as ion chromatography and ^{1}H NMR, are required to perform more rigorous measurements to eliminate potential interferences and achieve the accurate quantification of NH_3 concentration.[246]

7.3.3. Standardized Testing Procedures.
Furthermore, widely accepted standardized systems by the community are urgent to be established for the reproducible and credible evaluation of NRR performance.[247] First of all, the configurations of reaction cells, types of ion-exchange membranes, light sources and intensity, and operating conditions (temperature, pressure, gas flow rate, and stirring velocity) involved in the NRR experiments should be provided. Moreover, the currently reported NH_3 yield rates in the electrocatalytic NRR are generally normalized to the electrode geometric surface area (e.g., $\mu g\ h^{-1}\ cm^{-2}$) or catalyst mass (e.g., $\mu g\ h^{-1}\ mg^{-1}$). To eliminate the effects from the differences in the dimensions of substrate electrodes, specific

area of the catalysts and their loading amounts, the electrochemically active surface area (ECSA) is suggested to enable more meaningful comparisons of the results. Instead of the actual catalyst amount, the mass of active structures/compositions (e.g., single atoms in SACs) is sometimes applied in calculating per mass yield rate. In this case, identification of real active sites is critical to evaluate the performance, especially the highly active centers in low densities. Last but not least, to achieve meaningful results, appropriate benchmark catalysts are highly desirable in the NRR, just like these commercially available electrocatalysts of RuO_2, IrO_2, and Pt/C widely used in the OER, ORR, and HER. Testing these benchmark catalysts with the recommended experimental setup and operating conditions, the researchers could check whether the observed performance is in accord with the literature data.

7.4. Efficient Integration of Multiple Design Strategies. With preliminary achievements, an efficient integration of multiple design strategies, such as vacancy engineering and morphological regulation (e.g., ultrathin TiO_2 NSs with OVs), heteroatom doping and vacancy engineering (e.g., P-doped CN containing NVs), heteroatom doping and morphological regulation (e.g., Fe-doped CeO_2 NSs), and amorphization and vacancy engineering (e.g., amorphous BVC-A with OVs), sheds new light on the development of NRR catalysts. For instance, the controllable regulation on catalyst morphologies could expose more available active sites, facilitate the electron migration, and strengthen the accessibility of reactants. Meanwhile, an efficient introduction of heteroatom dopants or vacancies into the catalysts would enhance their adsorption and activation ability toward inert N_2. Utilizing the synergetic effects, tremendously promoted catalytic performance in NRR will be highly anticipated.

An efficient engineering of new catalysts relies heavily on the development of attractive methodologies. To this end, great efforts are still in huge demand to develop feasible and facile synthetic approaches and to realize the controllable fabrication and precise manipulation of catalysts. Furthermore, although many classical synthetic routes such as hydrothermal and calcination approaches have been extensively developed for the catalyst synthesis, they are not easy for large-scale production. To achieve a wide range of commercial applications, highly efficient and productive routes are imperative to be developed.

In summary, it is envisioned that rational catalyst design, coupled with reliable theoretical calculations, advanced in situ/operando characterization techniques, and rigorous NH_3 synthesis and measurement protocols, will greatly promote the rapid development of N_2 reduction under ambient conditions in the near future.

■ AUTHOR INFORMATION

Corresponding Authors
Lei Shi − *School of Engineering, Edith Cowan University, Joondalup, Western Australia 6027, Australia*; Email: l.shi@ecu.edu.au

Hongqi Sun − *School of Engineering, Edith Cowan University, Joondalup, Western Australia 6027, Australia*; orcid.org/0000-0003-0907-5626; Email: h.sun@ecu.edu.au

Authors
Yu Yin − *School of Engineering, Edith Cowan University, Joondalup, Western Australia 6027, Australia; School of Environmental and Chemical Engineering, Jiangsu University of Science and Technology, Zhenjiang 212003, P. R. China;* orcid.org/0000-0002-9891-4948

Shaobin Wang − *School of Chemical Engineering, The University of Adelaide, Adelaide, South Australia 5005, Australia;* orcid.org/0000-0002-1751-9162

Complete contact information is available at:
https://pubs.acs.org/10.1021/acscatal.0c01081

Notes
The authors declare no competing financial interest.

■ REFERENCES

(1) Suryanto, B. H. R.; Du, H. L.; Wang, D. B.; Chen, J.; Simonov, A. N.; MacFarlane, D. R. Challenges and Prospects in the Catalysis of Electroreduction of Nitrogen to Ammonia. *Nat. Catal.* **2019**, *2*, 290−296.

(2) Foster, S. L.; Bakovic, S. I. P.; Duda, R. D.; Maheshwari, S.; Milton, R. D.; Minteer, S. D.; Janik, M. J.; Renner, J. N.; Greenlee, L. F. Catalysts for Nitrogen Reduction to Ammonia. *Nat. Catal.* **2018**, *1*, 490−500.

(3) Sippel, D.; Rohde, M.; Netzer, J.; Trncik, C.; Gies, J.; Grunau, K.; Djurdjevic, I.; Decamps, L.; Andrade, S. L. A.; Einsle, O. A Bound Reaction Intermediate Sheds Light on the Mechanism of Nitrogenase. *Science* **2018**, *359*, 1484−1489.

(4) Rodriguez, M. M.; Bill, E.; Brennessel, W. W.; Holland, P. L. N_2 Reduction and Hydrogenation to Ammonia by a Molecular Iron-Potassium Complex. *Science* **2011**, *334*, 780−783.

(5) Anderson, J. S.; Rittle, J.; Peters, J. C. Catalytic Conversion of Nitrogen to Ammonia by an Iron Model Complex. *Nature* **2013**, *501*, 84−87.

(6) Galloway, J. N.; Townsend, A. R.; Erisman, J. W.; Bekunda, M.; Cai, Z. C.; Freney, J. R.; Martinelli, L. A.; Seitzinger, S. P.; Sutton, M. A. Transformation of the Nitrogen Cycle: Recent Trends, Questions, and Potential Solutions. *Science* **2008**, *320*, 889−892.

(7) Chen, J. G.; Crooks, R. M.; Seefeldt, L. C.; Bren, K. L.; Bullock, R. M.; Darensbourg, M. Y.; Holland, P. L.; Hoffman, B.; Janik, M. J.; Jones, A. K.; Kanatzidis, M. G.; King, P.; Lancaster, K. M.; Lymar, S. V.; Pfromm, P.; Schneider, W. F.; Schrock, R. R. Beyond Fossil Fuel-Driven Nitrogen Transformations. *Science* **2018**, *360*, eaar6611.

(8) Deng, J.; Iniguez, J. A.; Liu, C. Electrocatalytic Nitrogen Reduction at Low Temperature. *Joule* **2018**, *2*, 846−856.

(9) Huang, Y. W.; Zhang, N.; Wu, Z. J.; Xie, X. Q. Artificial Nitrogen Fixation over Bismuth-Based Photocatalysts: Fundamentals and Future Perspectives. *J. Mater. Chem. A* **2020**, *8*, 4978−4995.

(10) Zhang, S.; Zhao, Y.; Shi, R.; Waterhouse, G. I. N.; Zhang, T. Photocatalytic Ammonia Synthesis: Recent Progress and Future. *EnergyChem.* **2019**, *1*, 100013.

(11) Cui, X. Y.; Tang, C.; Zhang, Q. A Review of Electrocatalytic Reduction of Dinitrogen to Ammonia under Ambient Conditions. *Adv. Energy Mater.* **2018**, *8*, 1800369.

(12) Ling, C. Y.; Niu, X. H.; Li, Q.; Du, A. J.; Wang, J. L. Metal-Free Single Atom Catalyst for N_2 Fixation Driven by Visible Light. *J. Am. Chem. Soc.* **2018**, *140*, 14161−14168.

(13) van der Ham, C. J. M.; Koper, M. T. M.; Hetterscheid, D. G. H. Challenges in Reduction of Dinitrogen by Proton and Electron Transfer. *Chem. Soc. Rev.* **2014**, *43*, 5183−5191.

(14) Bazhenova, T. A.; Shilov, A. E. Nitrogen Fixation in Solution. *Coord. Chem. Rev.* **1995**, *144*, 69−145.

(15) Yandulov, D. V.; Schrock, R. R. Catalytic Reduction of Dinitrogen to Ammonia at a Single Molybdenum Center. *Science* **2003**, *301*, 76−78.

(16) Liu, C. W.; Li, Q. Y.; Zhang, J.; Jin, Y. G.; MacFarlane, D. R.; Sun, C. H. Conversion of Dinitrogen to Ammonia on Ru Atoms Supported on Boron Sheets: A DFT Study. *J. Mater. Chem. A* **2019**, *7*, 4771−4776.

(17) Legare, M. A.; Belanger-Chabot, G.; Dewhurst, R. D.; Welz, E.; Krummenacher, I.; Engels, B.; Braunschweig, H. Nitrogen Fixation and Reduction at Boron. *Science* **2018**, *359*, 896−899.

(18) Abghoui, Y.; Garden, A. L.; Howalt, J. G.; Vegge, T.; Skulason, E. Electroreduction of N₂ to Ammonia at Ambient Conditions on Mononitrides of Zr, Nb, Cr, and V: A DFT Guide for Experiments. *ACS Catal.* **2016**, *6*, 635−646.

(19) Abghoui, Y.; Skulason, E. Electrochemical Synthesis of Ammonia Via Mars-Van Krevelen Mechanism on the (111) Facets of Group III-VII Transition Metal Mononitrides. *Catal. Today* **2017**, *286*, 78−84.

(20) Abghoui, Y.; Skulason, E. Computational Predictions of Catalytic Activity of Zincblende (110) Surfaces of Metal Nitrides for Electrochemical Ammonia Synthesis. *J. Phys. Chem. C* **2017**, *121*, 6141−6151.

(21) Li, J.; Li, H.; Zhan, G. M.; Zhang, L. Z. Solar Water Splitting and Nitrogen Fixation with Layered Bismuth Oxyhalides. *Acc. Chem. Res.* **2017**, *50*, 112−121.

(22) Wang, S. Y.; Hai, X.; Ding, X.; Chang, K.; Xiang, Y. G.; Meng, X. G.; Yang, Z. X.; Chen, H.; Ye, J. H. Light-Switchable Oxygen Vacancies in Ultrafine Bi₅O₇Br Nanotubes for Boosting Solar-Driven Nitrogen Fixation in Pure Water. *Adv. Mater.* **2017**, *29*, 1701774.

(23) Zhao, Y. F.; Zhao, Y. X.; Waterhouse, G. I. N.; Zheng, L. R.; Cao, X. Z.; Teng, F.; Wu, L. Z.; Tung, C. H.; O'Hare, D.; Zhang, T. R. Layered-Double-Hydroxide Nanosheets as Efficient Visible-Light-Driven Photocatalysts for Dinitrogen Fixation. *Adv. Mater.* **2017**, *29*, 1703828.

(24) Zhao, Y. X.; Zhao, Y. F.; Shi, R.; Wang, B.; Waterhouse, G. I. N.; Wu, L. Z.; Tung, C. H.; Zhang, T. R. Tuning Oxygen Vacancies in Ultrathin TiO₂ Nanosheets to Boost Photocatalytic Nitrogen Fixation up to 700 nm. *Adv. Mater.* **2019**, *31*, 1806482.

(25) Li, H.; Mao, C. L.; Shang, H.; Yang, Z. P.; Ai, Z. H.; Zhang, L. Z. New Opportunities for Efficient N₂ Fixation by Nanosheet Photocatalysts. *Nanoscale* **2018**, *10*, 15429−15435.

(26) Liu, Y. W.; Cheng, M.; He, Z. H.; Gu, B. C.; Xiao, C.; Zhou, T. F.; Guo, Z. P.; Liu, J. D.; He, H. Y.; Ye, B. J.; Pan, B. C.; Xie, Y. Pothole-Rich Ultrathin WO₃ Nanosheets That Trigger N≡N Bond Activation of Nitrogen for Direct Nitrate Photosynthesis. *Angew. Chem., Int. Ed.* **2019**, *58*, 731−735.

(27) Yuan, S. J.; Chen, J. J.; Lin, Z. Q.; Li, W. W.; Sheng, G. P.; Yu, H. Q. Nitrate Formation from Atmospheric Nitrogen and Oxygen Photocatalysed by Nano-Sized Titanium Dioxide. *Nat. Commun.* **2013**, *4*, 2249.

(28) Cheng, M.; Xiao, C.; Xie, Y. Photocatalytic Nitrogen Fixation: The Role of Defects in Photocatalysts. *J. Mater. Chem. A* **2019**, *7*, 19616−19633.

(29) Tong, N.; Wang, Y.; Liu, Y.; Li, M. B.; Zhang, Z. Z.; Huang, H. J.; Sun, T.; Yang, J. X.; Li, F. Y.; Wang, X. X. PdSn/NiO/NaTaO₃:La for Photocatalytic Ammonia Synthesis by Reduction of NO₃⁻ with Formic Acid in Aqueous Solution. *J. Catal.* **2018**, *361*, 303−312.

(30) Hirakawa, H.; Hashimoto, M.; Shiraishi, Y.; Hirai, T. Selective Nitrate-to-Ammonia Transformation on Surface Defects of Titanium Dioxide Photocatalysts. *ACS Catal.* **2017**, *7*, 3713−3720.

(31) Medford, A. J.; Hatzell, M. C. Photon-Driven Nitrogen Fixation: Current Progress, Thermodynamic Considerations, and Future Outlook. *ACS Catal.* **2017**, *7*, 2624−2643.

(32) Habisreutinger, S. N.; Schmidt-Mende, L.; Stolarczyk, J. K. Photocatalytic Reduction of CO₂ on TiO₂ and Other Semiconductors. *Angew. Chem., Int. Ed.* **2013**, *52*, 7372−7408.

(33) Zhu, D.; Zhang, L. H.; Ruther, R. E.; Hamers, R. J. Photo-Illuminated Diamond as a Solid-State Source of Solvated Electrons in Water for Nitrogen Reduction. *Nat. Mater.* **2013**, *12*, 836−841.

(34) Ali, M.; Zhou, F. L.; Chen, K.; Kotzur, C.; Xiao, C. L.; Bourgeois, L.; Zhang, X. Y.; MacFarlane, D. R. Nanostructured

(35) Zhou, M.; Lou, X. W.; Xie, Y. Two-Dimensional Nanosheets for Photoelectrochemical Water Splitting: Possibilities and Opportunities. *Nano Today* **2013**, *8*, 598−618.

(36) Shen, S. H.; Lindley, S. A.; Chen, X. Y.; Zhang, J. Z. Hematite Heterostructures for Photoelectrochemical Water Splitting: Rational Materials Design and Charge Carrier Dynamics. *Energy Environ. Sci.* **2016**, *9*, 2744−2775.

(37) Kumar, B.; Llorente, M.; Froehlich, J.; Dang, T.; Sathrum, A.; Kubiak, C. P. Photochemical and Photoelectrochemical Reduction of CO₂. *Annu. Rev. Phys. Chem.* **2012**, *63*, 541−569.

(38) Jia, H. L.; Du, A. X.; Zhang, H.; Yang, J. H.; Jiang, R. B.; Wang, J. F.; Zhang, C. Y. Site-Selective Growth of Crystalline Ceria with Oxygen Vacancies on Gold Nanocrystals for near-Infrared Nitrogen Photofixation. *J. Am. Chem. Soc.* **2019**, *141*, 5083−5086.

(39) Wang, Y.; Shi, M. M.; Bao, D.; Meng, F. L.; Zhang, Q.; Zhou, Y. T.; Liu, K. H.; Zhang, Y.; Wang, J. Z.; Chen, Z. W.; Liu, D. P.; Jiang, Z.; Luo, M.; Gu, L.; Zhang, Q. H.; Cao, X. Z.; Yao, Y.; Shao, M. H.; Zhang, Y.; Zhang, X. B.; Chen, J. G. G.; Yan, J. M.; Jiang, Q. Generating Defect-Rich Bismuth for Enhancing the Rate of Nitrogen Electroreduction to Ammonia. *Angew. Chem., Int. Ed.* **2019**, *58*, 9464−9469.

(40) Li, L.; Wang, Y. C.; Vanka, S.; Mu, X. Y.; Mi, Z. T.; Li, C. J. Nitrogen Photofixation over III-Nitride Nanowires Assisted by Ruthenium Clusters of Low Atomicity. *Angew. Chem., Int. Ed.* **2017**, *56*, 8701−8705.

(41) Zhang, G.; Ji, Q. H.; Zhang, K.; Chen, Y.; Li, Z. H.; Liu, H. J.; Li, J. H.; Qu, J. H. Triggering Surface Oxygen Vacancies on Atomic Layered Molybdenum Dioxide for a Low Energy Consumption Path toward Nitrogen Fixation. *Nano Energy* **2019**, *59*, 10−16.

(42) Liu, Y. Y.; Han, M. M.; Xiong, Q. Z.; Zhang, S. B.; Zhao, C. J.; Gong, W. B.; Wang, G. Z.; Zhang, H. M.; Zhao, H. J. Dramatically Enhanced Ambient Ammonia Electrosynthesis Performance by in-Operando Created Li-S Interactions on MoS₂ Electrocatalyst. *Adv. Energy Mater.* **2019**, *9*, 1803935.

(43) Chen, S. M.; Perathoner, S.; Ampelli, C.; Mebrahtu, C.; Su, D. S.; Centi, G. Electrocatalytic Synthesis of Ammonia at Room Temperature and Atmospheric Pressure from Water and Nitrogen on a Carbon-Nanotube-Based Electrocatalyst. *Angew. Chem., Int. Ed.* **2017**, *56*, 2699−2703.

(44) Hawtof, R.; Ghosh, S.; Guarr, E.; Xu, C. Y.; Sankaran, R. M.; Renner, J. N. Catalyst-Free, Highly Selective Synthesis of Ammonia from Nitrogen and Water by a Plasma Electrolytic System. *Sci. Adv.* **2019**, *5*, eaat5778.

(45) McEnaney, J. M.; Singh, A. R.; Schwalbe, J. A.; Kibsgaard, J.; Lin, J. C.; Cargnello, M.; Jaramillo, T. F.; Norskov, J. K. Ammonia Synthesis from N₂ and H₂O Using a Lithium Cycling Electrification Strategy at Atmospheric Pressure. *Energy Environ. Sci.* **2017**, *10*, 1621−1630.

(46) Ma, J. L.; Bao, D.; Shi, M. M.; Yan, J. M.; Zhang, X. B. Reversible Nitrogen Fixation Based on a Rechargeable Lithium-Nitrogen Battery for Energy Storage. *Chem.* **2017**, *2*, 525−532.

(47) Lazouski, N.; Schiffer, Z. J.; Williams, K.; Manthiram, K. Understanding Continuous Lithium-Mediated Electrochemical Nitrogen Reduction. *Joule* **2019**, *3*, 1127−1139.

(48) Zhou, F. L.; Azofra, L. M.; Ali, M.; Kar, M.; Simonov, A. N.; McDonnell-Worth, C.; Sun, C. H.; Zhang, X. Y.; MacFarlane, D. R. Electro-Synthesis of Ammonia from Nitrogen at Ambient Temperature and Pressure in Ionic Liquids. *Energy Environ. Sci.* **2017**, *10*, 2516−2520.

(49) Jia, H. P.; Quadrelli, E. A. Mechanistic Aspects of Dinitrogen Cleavage and Hydrogenation to Produce Ammonia in Catalysis and Organometallic Chemistry: Relevance of Metal Hydride Bonds and Dihydrogen. *Chem. Soc. Rev.* **2014**, *43*, 547−564.

(50) Chen, X. Z.; Li, N.; Kong, Z. Z.; Ong, W. J.; Zhao, X. J. Photocatalytic Fixation of Nitrogen to Ammonia: State-of-the-Art Advancements and Future Prospects. *Mater. Horiz.* **2018**, *5*, 9−27.

(51) Zhao, S. L.; Lu, X. Y.; Wang, L. Z.; Gale, J.; Amal, R. Carbon-Based Metal-Free Catalysts for Electrocatalytic Reduction of Nitrogen for Synthesis of Ammonia at Ambient Conditions. *Adv. Mater.* **2019**, *31*, 1805367.

(52) Chen, G.-F.; Ren, S.; Zhang, L.; Cheng, H.; Luo, Y.; Zhu, K.; Ding, L.-X.; Wang, H. Advances in Electrocatalytic N_2 Reduction—Strategies to Tackle the Selectivity Challenge. *Small Methods* **2019**, *3*, 1800337.

(53) Wan, Y.; Xu, J.; Lv, R. Heterogeneous Electrocatalysts Design for Nitrogen Reduction Reaction under Ambient Conditions. *Mater. Today* **2019**, *27*, 69–90.

(54) Yan, D.; Li, H.; Chen, C.; Zou, Y.; Wang, S. Defect Engineering Strategies for Nitrogen Reduction Reactions under Ambient Conditions. *Small Methods* **2019**, *3*, 1800331.

(55) Shi, R.; Zhao, Y. X.; Waterhouse, G. I. N.; Zhang, S.; Zhang, T. R. Defect Engineering in Photocatalytic Nitrogen Fixation. *ACS Catal.* **2019**, *9*, 9739–9750.

(56) Mao, C. L.; Wang, J. X.; Zou, Y. J.; Li, H.; Zhan, G. M.; Li, J.; Zhao, J. C.; Zhang, L. Z. Anion (O, N, C, and S) Vacancies Promoted Photocatalytic Nitrogen Fixation. *Green Chem.* **2019**, *21*, 2852–2867.

(57) Xu, L.; Jiang, Q. Q.; Xiao, Z. H.; Li, X. Y.; Huo, J.; Wang, S. Y.; Dai, L. M. Plasma-Engraved Co_3O_4 Nanosheets with Oxygen Vacancies and High Surface Area for the Oxygen Evolution Reaction. *Angew. Chem., Int. Ed.* **2016**, *55*, 5277–5281.

(58) Li, H.; Tsai, C.; Koh, A. L.; Cai, L. L.; Contryman, A. W.; Fragapane, A. H.; Zhao, J. H.; Han, H. S.; Manoharan, H. C.; Abild-Pedersen, F.; Norskov, J. K.; Zheng, X. L. Activating and Optimizing MoS_2 Basal Planes for Hydrogen Evolution through the Formation of Strained Sulphur Vacancies. *Nat. Mater.* **2016**, *15*, 48–53.

(59) Li, H.; Li, J.; Ai, Z. H.; Jia, F. L.; Zhang, L. Z. Oxygen Vacancy-Mediated Photocatalysis of BiOCl: Reactivity, Selectivity, and Perspectives. *Angew. Chem., Int. Ed.* **2018**, *57*, 122–138.

(60) Cheng, F. Y.; Zhang, T. R.; Zhang, Y.; Du, J.; Han, X. P.; Chen, J. Enhancing Electrocatalytic Oxygen Reduction on MnO_2 with Vacancies. *Angew. Chem., Int. Ed.* **2013**, *52*, 2474–2477.

(61) Liu, L. J.; Zhao, H. L.; Andino, J. M.; Li, Y. Photocatalytic CO_2 Reduction with H_2O on TiO_2 Nanocrystals: Comparison of Anatase, Rutile, and Brookite Polymorphs and Exploration of Surface Chemistry. *ACS Catal.* **2012**, *2*, 1817–1828.

(62) Liu, L. J.; Jiang, Y. Q.; Zhao, H. L.; Chen, J. T.; Cheng, J. L.; Yang, K. S.; Li, Y. Engineering Coexposed {001} and {101} Facets in Oxygen-Deficient TiO_2 Nanocrystals for Enhanced CO_2 Photo-reduction under Visible Light. *ACS Catal.* **2016**, *6*, 1097–1108.

(63) Fang, Y. F.; Liu, Z. C.; Han, J. R.; Jin, Z. Y.; Han, Y. Q.; Wang, F. X.; Niu, Y. S.; Wu, Y. P.; Xu, Y. H. High-Performance Electrocatalytic Conversion of N_2 to NH_3 Using Oxygen-Vacancy-Rich TiO_2 in Situ Grown on $Ti_3C_2T_x$ Mxene. *Adv. Energy Mater.* **2019**, *9*, 1803406.

(64) Yao, J.-X.; Bao, D.; Zhang, Q.; Shi, M.-M.; Wang, Y.; Gao, R.; Yan, J.-M.; Jiang, Q. Tailoring Oxygen Vacancies of $BiVO_4$ toward Highly Efficient Noble-Metal-Free Electrocatalyst for Artificial N_2 Fixation under Ambient Conditions. *Small Methods* **2019**, *3*, 1800333.

(65) Han, Z. S.; Choi, C.; Hong, S.; Wu, T. S.; Soo, Y. L.; Jung, Y.; Qiu, J. S.; Sun, Z. Y. Activated TiO_2 with Tuned Vacancy for Efficient Electrochemical Nitrogen Reduction. *Appl. Catal., B* **2019**, *257*, 117896.

(66) Liu, Y.; Kong, X.; Guo, X.; Li, Q.; Ke, J.; Wang, R.; Li, Q.; Geng, Z.; Zeng, J. Enhanced N_2 Electroreduction over $LaCoO_3$ by Introducing Oxygen Vacancies. *ACS Catal.* **2020**, *10*, 1077–1085.

(67) Li, H.; Shang, J.; Ai, Z. H.; Zhang, L. Z. Efficient Visible Light Nitrogen Fixation with BiOBr Nanosheets of Oxygen Vacancies on the Exposed {001} Facets. *J. Am. Chem. Soc.* **2015**, *137*, 6393–6399.

(68) Hou, T. T.; Xiao, Y.; Cui, P. X.; Huang, Y. N.; Tan, X. P.; Zheng, X. S.; Zou, Y.; Liu, C. X.; Zhu, W. K.; Liang, S. Q.; Wang, L. B. Operando Oxygen Vacancies for Enhanced Activity and Stability toward Nitrogen Photofixation. *Adv. Energy Mater.* **2019**, *9*, 1902319.

(69) Yang, J. H.; Guo, Y. Z.; Jiang, R. B.; Qin, F.; Zhang, H.; Lu, W. Z.; Wang, J. F.; Yu, J. C. High-Efficiency "Working-in-Tandem" Nitrogen Photofixation Achieved by Assembling Plasmonic Gold Nanocrystals on Ultrathin Titania Nanosheets. *J. Am. Chem. Soc.* **2018**, *140*, 8497–8508.

(70) Fan, G. L.; Li, F.; Evans, D. G.; Duan, X. Catalytic Applications of Layered Double Hydroxides: Recent Advances and Perspectives. *Chem. Soc. Rev.* **2014**, *43*, 7040–7066.

(71) Zhao, Y. F.; Chen, G. B.; Bian, T.; Zhou, C.; Waterhouse, G. I. N.; Wu, L. Z.; Tung, C. H.; Smith, L. J.; O'Hare, D.; Zhang, T. R. Defect-Rich Ultrathin ZnAl-Layered Double Hydroxide Nanosheets for Efficient Photoreduction of CO_2 to CO with Water. *Adv. Mater.* **2015**, *27*, 7824–7831.

(72) Li, X. H.; Li, T. S.; Ma, Y. J.; Wei, Q.; Qiu, W. B.; Guo, H. R.; Shi, X. F.; Zhang, P.; Asiri, A. M.; Chen, L.; Tang, B.; Sun, X. P. Boosted Electrocatalytic N_2 Reduction to NH_3 by Defect-Rich MoS_2 Nanoflower. *Adv. Energy Mater.* **2018**, *8*, 1801357.

(73) Hirakawa, H.; Hashimoto, M.; Shiraishi, Y.; Hirai, T. Photocatalytic Conversion of Nitrogen to Ammonia with Water on Surface Oxygen Vacancies of Titanium Dioxide. *J. Am. Chem. Soc.* **2017**, *139*, 10929–10936.

(74) Jin, H.; Li, L.; Liu, X.; Tang, C.; Xu, W.; Chen, S.; Song, L.; Zheng, Y.; Qiao, S.-Z. Nitrogen Vacancies on 2D Layered W_2N_3: A Stable and Efficient Active Site for Nitrogen Reduction Reaction. *Adv. Mater.* **2019**, *31*, 1902709.

(75) Dong, G. H.; Ho, W. K.; Wang, C. Y. Selective Photocatalytic N_2 Fixation Dependent on g-C_3N_4 Induced by Nitrogen Vacancies. *J. Mater. Chem. A* **2015**, *3*, 23435–23441.

(76) Niu, P.; Yin, L. C.; Yang, Y. Q.; Liu, G.; Cheng, H. M. Increasing the Visible Light Absorption of Graphitic Carbon Nitride (Melon) Photocatalysts by Homogeneous Self-Modification with Nitrogen Vacancies. *Adv. Mater.* **2014**, *26*, 8046–8052.

(77) Yu, H. J.; Shi, R.; Zhao, Y. X.; Bian, T.; Zhao, Y. F.; Zhou, C.; Waterhouse, G. I. N.; Wu, L. Z.; Tung, C. H.; Zhang, T. R. Alkali-Assisted Synthesis of Nitrogen Deficient Graphitic Carbon Nitride with Tunable Band Structures for Efficient Visible-Light-Driven Hydrogen Evolution. *Adv. Mater.* **2017**, *29*, 1605148.

(78) Lv, C.; Qian, Y. M.; Yan, C. S.; Ding, Y.; Liu, Y. Y.; Chen, G.; Yu, G. H. Defect Engineering Metal-Free Polymeric Carbon Nitride Electrocatalyst for Effective Nitrogen Fixation under Ambient Conditions. *Angew. Chem., Int. Ed.* **2018**, *57*, 10246–10250.

(79) Li, X.; Sun, X.; Zhang, L.; Sun, S.; Wang, W. Efficient Photocatalytic Fixation of N_2 by KOH-Treated g-C_3N_4. *J. Mater. Chem. A* **2018**, *6*, 3005–3011.

(80) Shiraishi, Y.; Shiota, S.; Kofuji, Y.; Hashimoto, M.; Chishiro, K.; Hirakawa, H.; Tanaka, S.; Ichikawa, S.; Hirai, T. Nitrogen Fixation with Water on Carbon-Nitride-Based Metal-Free Photocatalysts with 0.1% Solar-to-Ammonia Energy Conversion Efficiency. *ACS Appl. Energy Mater.* **2018**, *1*, 4169–4177.

(81) Nash, J.; Yang, X.; Anibal, J.; Dunwell, M.; Yao, S. Y.; Attenkofer, K.; Chen, J. G. G.; Yan, Y. S.; Xu, B. J. Elucidation of the Active Phase and Deactivation Mechanisms of Chromium Nitride in the Electrochemical Nitrogen Reduction Reaction. *J. Phys. Chem. C* **2019**, *123*, 23967–23975.

(82) Yang, X.; Nash, J.; Anibal, J.; Dunwell, M.; Kattel, S.; Stavitski, E.; Attenkofer, K.; Chen, J. G. G.; Yan, Y. S.; Xu, B. J. Mechanistic Insights into Electrochemical Nitrogen Reduction Reaction on Vanadium Nitride Nanoparticles. *J. Am. Chem. Soc.* **2018**, *140*, 13387–13391.

(83) Yang, X.; Kattel, S.; Nash, J.; Chang, X. X.; Lee, J. H.; Yan, Y. S.; Chen, J. G. G.; Xu, B. J. Quantification of Active Sites and Elucidation of the Reaction Mechanism of the Electrochemical Nitrogen Reduction Reaction on Vanadium Nitride. *Angew. Chem., Int. Ed.* **2019**, *58*, 13768–13772.

(84) Hu, S.; Li, Y. M.; Li, F. Y.; Fan, Z. P.; Ma, H. F.; Li, W.; Kang, X. X. Construction of g-C_3N_4/$Zn_{0.11}Sn_{0.12}Cd_{0.88}S_{1.12}$ Hybrid Heterojunction Catalyst with Outstanding Nitrogen Photofixation Performance Induced by Sulfur Vacancies. *ACS Sustainable Chem. Eng.* **2016**, *4*, 2269–2278.

(85) Yin, Y.; Han, J. C.; Zhang, Y. M.; Zhang, X. H.; Xu, P.; Yuan, Q.; Samad, L.; Wang, X. J.; Wang, Y.; Zhang, Z. H.; Zhang, P.; Cao, X. Z.; Song, B.; Jin, S. Contributions of Phase, Sulfur Vacancies, and

Edges to the Hydrogen Evolution Reaction Catalytic Activity of Porous Molybdenum Disulfide Nanosheets. *J. Am. Chem. Soc.* **2016**, *138*, 7965−7972.

(86) Ding, Q.; Song, B.; Xu, P.; Jin, S. Efficient Electrocatalytic and Photoelectrochemical Hydrogen Generation Using MoS$_2$ and Related Compounds. *Chem.* **2016**, *1*, 699−726.

(87) Sun, S. M.; Li, X. M.; Wang, W. Z.; Zhang, L.; Sun, X. Photocatalytic Robust Solar Energy Reduction of Dinitrogen to Ammonia on Ultrathin MoS$_2$. *Appl. Catal., B* **2017**, *200*, 323−329.

(88) Suryanto, B. H. R.; Wang, D. B.; Azofra, L. M.; Harb, M.; Cavallo, L.; Jalili, R.; Mitchell, D. R. G.; Chatti, M.; MacFarlane, D. R. MoS$_2$ Polymorphic Engineering Enhances Selectivity in the Electrochemical Reduction of Nitrogen to Ammonia. *ACS Energy Lett.* **2019**, *4*, 430−435.

(89) Feng, H.; Xu, Z.; Ren, L.; Liu, C.; Zhuang, J.; Hu, Z.; Xu, X.; Chen, J.; Wang, J.; Hao, W.; Du, Y.; Dou, S. X. Activating Titania for Efficient Electrocatalysis by Vacancy Engineering. *ACS Catal.* **2018**, *8*, 4288−4293.

(90) Xiao, Z.; Wang, Y.; Huang, Y.-C.; Wei, Z.; Dong, C.-L.; Ma, J.; Shen, S.; Li, Y.; Wang, S. Filling the Oxygen Vacancies in Co$_3$O$_4$ with Phosphorus: An Ultra-Efficient Electrocatalyst for Overall Water Splitting. *Energy Environ. Sci.* **2017**, *10*, 2563−2569.

(91) Chu, K.; Li, Q. Q.; Liu, Y. P.; Wang, J.; Cheng, Y. H. Filling the Nitrogen Vacancies with Sulphur Dopants in Graphitic C$_3$N$_4$ for Efficient and Robust Electrocatalytic Nitrogen Reduction. *Appl. Catal., B* **2020**, *267*, 118693.

(92) Rao, C. N. R.; Gopalakrishnan, K.; Govindaraj, A. Synthesis, Properties and Applications of Graphene Doped with Boron, Nitrogen and Other Elements. *Nano Today* **2014**, *9*, 324−343.

(93) Wang, X. W.; Sun, G. Z.; Routh, P.; Kim, D. H.; Huang, W.; Chen, P. Heteroatom-Doped Graphene Materials: Syntheses, Properties and Applications. *Chem. Soc. Rev.* **2014**, *43*, 7067−7098.

(94) Jiao, Y.; Zheng, Y.; Davey, K.; Qiao, S. Z. Activity Origin and Catalyst Design Principles for Electrocatalytic Hydrogen Evolution on Heteroatom-Doped Graphene. *Nat. Energy* **2016**, *1*, 16130.

(95) Zou, H.; Rong, W.; Long, B.; Ji, Y.; Duan, L. Corrosion-Induced Cl-Doped Ultrathin Graphdiyne toward Electrocatalytic Nitrogen Reduction at Ambient Conditions. *ACS Catal.* **2019**, *9*, 10649−10655.

(96) Liu, M.; Qiu, X. Q.; Miyauchi, M.; Hashimoto, K. Energy-Level Matching of Fe(III) Ions Grafted at Surface and Doped in Bulk for Efficient Visible-Light Photocatalysts. *J. Am. Chem. Soc.* **2013**, *135*, 10064−10072.

(97) Inturi, S. N. R.; Boningari, T.; Suidan, M.; Smirniotis, P. G. Visible-Light-Induced Photodegradation of Gas Phase Acetonitrile Using Aerosol-Made Transition Metal (V, Cr, Fe, Co, Mn, Mo, Ni, Cu, Y, Ce, and Zr) Doped TiO$_2$. *Appl. Catal., B* **2014**, *144*, 333−342.

(98) Wei, J.; Zhou, D. D.; Sun, Z. K.; Deng, Y. H.; Xia, Y. Y.; Zhao, D. Y. A Controllable Synthesis of Rich Nitrogen-Doped Ordered Mesoporous Carbon for CO$_2$ Capture and Supercapacitors. *Adv. Funct. Mater.* **2013**, *23*, 2322−2328.

(99) Li, B.; Dai, F.; Xiao, Q. F.; Yang, L.; Shen, J. M.; Zhang, C. M.; Cai, M. Nitrogen-Doped Activated Carbon for a High Energy Hybrid Supercapacitor. *Energy Environ. Sci.* **2016**, *9*, 102−106.

(100) Zhu, Z. Q.; Wang, S. W.; Du, J.; Jin, Q.; Zhang, T. R.; Cheng, F. Y.; Chen, J. Ultrasmall Sn Nanoparticles Embedded in Nitrogen-Doped Porous Carbon as High-Performance Anode for Lithium-Ion Batteries. *Nano Lett.* **2014**, *14*, 153−157.

(101) Zhang, P.; Sun, F.; Xiang, Z. H.; Shen, Z. G.; Yun, J.; Cao, D. P. ZIF-Derived in Situ Nitrogen-Doped Porous Carbons as Efficient Metal-Free Electrocatalysts for Oxygen Reduction Reaction. *Energy Environ. Sci.* **2014**, *7*, 442−450.

(102) Song, Y.; Johnson, D.; Peng, R.; Hensley, D. K.; Bonnesen, P. V.; Liang, L. B.; Huang, J. S.; Yang, F. C.; Zhang, F.; Qiao, R.; Baddorf, A. P.; Tschaplinski, T. J.; Engle, N. L.; Hatzell, M. C.; Wu, Z. L.; Cullen, D. A.; Meyer, H. M.; Sumpter, B. G.; Rondinone, A. J. A Physical Catalyst for the Electrolysis of Nitrogen to Ammonia. *Sci. Adv.* **2018**, *4*, e1700336.

(103) Liu, Y.; Su, Y.; Quan, X.; Fan, X.; Chen, S.; Yu, H.; Zhao, H.; Zhang, Y.; Zhao, J. Facile Ammonia Synthesis from Electrocatalytic N$_2$ Reduction under Ambient Conditions on N-Doped Porous Carbon. *ACS Catal.* **2018**, *8*, 1186−1191.

(104) Aijaz, A.; Fujiwara, N.; Xu, Q. From Metal-Organic Framework to Nitrogen-Decorated Nanoporous Carbons: High CO$_2$ Uptake and Efficient Catalytic Oxygen Reduction. *J. Am. Chem. Soc.* **2014**, *136*, 6790−6793.

(105) Mukherjee, S.; Cullen, D. A.; Karakalos, S.; Liu, K. X.; Zhang, H.; Zhao, S.; Xu, H.; More, K. L.; Wang, G. F.; Wu, G. Metal-Organic Framework-Derived Nitrogen-Doped Highly Disordered Carbon for Electrochemical Ammonia Synthesis Using N$_2$ and H$_2$O in Alkaline Electrolytes. *Nano Energy* **2018**, *48*, 217−226.

(106) Zhao, C. J.; Zhang, S. B.; Han, M. M.; Zhang, X.; Liu, Y. Y.; Li, W. Y.; Chen, C.; Wang, G. Z.; Zhang, H. M.; Zhao, H. J. Ambient Electrosynthesis of Ammonia on a Biomass-Derived Nitrogen-Doped Porous Carbon Electrocatalyst: Contribution of Pyridinic Nitrogen. *ACS Energy Lett.* **2019**, *4*, 377−383.

(107) Yu, X.; Han, P.; Wei, Z.; Huang, L.; Gu, Z.; Peng, S.; Ma, J.; Zheng, G. Boron-Doped Graphene for Electrocatalytic N$_2$ Reduction. *Joule* **2018**, *2*, 1610−1622.

(108) Yang, L. J.; Jiang, S. J.; Zhao, Y.; Zhu, L.; Chen, S.; Wang, X. Z.; Wu, Q.; Ma, J.; Ma, Y. W.; Hu, Z. Boron-Doped Carbon Nanotubes as Metal-Free Electrocatalysts for the Oxygen Reduction Reaction. *Angew. Chem., Int. Ed.* **2011**, *50*, 7132−7135.

(109) Nakata, K.; Ozaki, T.; Terashima, C.; Fujishima, A.; Einaga, Y. High-Yield Electrochemical Production of Formaldehyde from CO$_2$ and Seawater. *Angew. Chem., Int. Ed.* **2014**, *53*, 871−874.

(110) Xia, L.; Wu, X.; Wang, Y.; Niu, Z.; Liu, Q.; Li, T.; Shi, X.; Asiri, A. M.; Sun, X. S-Doped Carbon Nanospheres: An Efficient Electrocatalyst toward Artificial N$_2$ Fixation to NH$_3$. *Small Methods* **2019**, *3*, 1800251.

(111) Wang, S. Y.; Iyyamperumal, E.; Roy, A.; Xue, Y. H.; Yu, D. S.; Dai, L. M. Vertically Aligned BCN Nanotubes as Efficient Metal-Free Electrocatalysts for the Oxygen Reduction Reaction: A Synergetic Effect by Co-Doping with Boron and Nitrogen. *Angew. Chem., Int. Ed.* **2011**, *50*, 11756−11760.

(112) Ito, Y.; Cong, W. T.; Fujita, T.; Tang, Z.; Chen, M. W. High Catalytic Activity of Nitrogen and Sulfur Co-Doped Nanoporous Graphene in the Hydrogen Evolution Reaction. *Angew. Chem., Int. Ed.* **2015**, *54*, 2131−2136.

(113) Song, P. F.; Wang, H.; Kang, L.; Ran, B. C.; Song, H. H.; Wang, R. M. Electrochemical Nitrogen Reduction to Ammonia at Ambient Conditions on Nitrogen and Phosphorus Co-Doped Porous Carbon. *Chem. Commun.* **2019**, *55*, 687−690.

(114) Chen, C.; Yan, D. F.; Wang, Y.; Zhou, Y. Y.; Zou, Y. Q.; Li, Y. F.; Wang, S. Y. B-N Pairs Enriched Defective Carbon Nanosheets for Ammonia Synthesis with High Efficiency. *Small* **2019**, *15*, 1805029.

(115) Chu, K.; Liu, Y. P.; Cheng, Y. H.; Li, Q. Q. Synergistic Boron-Dopants and Boron-Induced Oxygen Vacancies in MnO$_2$ Nanosheets to Promote Electrocatalytic Nitrogen Reduction. *J. Mater. Chem. A* **2020**, *8*, 5200−5208.

(116) Liu, Y. P.; Li, Y. B.; Zhang, H.; Chu, K. Boosted Electrocatalytic N$_2$ Reduction on Fluorine-Doped SnO$_2$ Mesoporous Nanosheets. *Inorg. Chem.* **2019**, *58*, 10424−10431.

(117) Zhu, X. J.; Liu, Z. C.; Wang, H. B.; Zhao, R. B.; Chen, H. Y.; Wang, T.; Wang, F. X.; Luo, Y. L.; Wu, Y. P.; Sun, X. P. Boosting Electrocatalytic N$_2$ Reduction to NH$_3$ on β-FeOOH by Fluorine Doping. *Chem. Commun.* **2019**, *55*, 3987−3990.

(118) Chu, K.; Liu, Y. P.; Li, Y. B.; Guo, Y. L.; Tian, Y.; Zhang, H. Multi-Functional Mo-Doping in MnO$_2$ Nanoflowers toward Efficient and Robust Electrocatalytic Nitrogen Fixation. *Appl. Catal., B* **2020**, *264*, 118525.

(119) Zhang, N.; Jalil, A.; Wu, D. X.; Chen, S. M.; Liu, Y. F.; Gao, C.; Ye, W.; Qi, Z. M.; Ju, H. X.; Wang, C. M.; Wu, X. J.; Song, L.; Zhu, J. F.; Xiong, Y. J. Refining Defect States in W$_{18}$O$_{49}$ by Mo Doping: A Strategy for Tuning N$_2$ Activation Towards Solar-Driven Nitrogen Fixation. *J. Am. Chem. Soc.* **2018**, *140*, 9434−9443.

(120) Cao, N.; Chen, Z.; Zang, K. T.; Xu, J.; Zhong, J.; Luo, J.; Xu, X.; Zheng, G. F. Doping Strain Induced bi-Ti^{3+} Pairs for Efficient N$_2$ Activation and Electrocatalytic Fixation. *Nat. Commun.* **2019**, *10*, 2877.

(121) Zhao, W. R.; Zhang, J.; Zhu, X.; Zhang, M.; Tang, J.; Tan, M.; Wang, Y. Enhanced Nitrogen Photofixation on Fe-Doped TiO$_2$ with Highly Exposed (101) Facets in the Presence of Ethanol as Scavenger. *Appl. Catal., B* **2014**, *144*, 468−477.

(122) Hu, S.; Chen, X.; Li, Q.; Li, F.; Fan, Z.; Wang, H.; Wang, Y.; Zheng, B.; Wu, G. Fe^{3+} Doping Promoted N$_2$ Photofixation Ability of Honeycombed Graphitic Carbon Nitride: The Experimental and Density Functional Theory Simulation Analysis. *Appl. Catal., B* **2017**, *201*, 58−69.

(123) Wu, T.; Zhu, X.; Xing, Z.; Mou, S.; Li, C.; Qiao, Y.; Liu, Q.; Luo, Y.; Shi, X.; Zhang, Y.; Sun, X. Greatly Improving Electrochemical N$_2$ Reduction over TiO$_2$ Nanoparticles by Iron Doping. *Angew. Chem., Int. Ed.* **2019**, *58*, 18449−18453.

(124) Chu, K.; Cheng, Y. H.; Li, Q. Q.; Liu, Y. P.; Tian, Y. Fe-Doping Induced Morphological Changes, Oxygen Vacancies and Ce^{3+}−Ce^{3+} Pairs in CeO$_2$ for Promoting Electrocatalytic Nitrogen Fixation. *J. Mater. Chem. A* **2020**, *8*, 5865−5873.

(125) Luo, J.; Bai, X.; Li, Q.; Yu, X.; Li, C.; Wang, Z.; Wu, W.; Liang, Y.; Zhao, Z.; Liu, H. Band Structure Engineering of Bioinspired Fe Doped SrMoO$_4$ for Enhanced Photocatalytic Nitrogen Reduction Performance. *Nano Energy* **2019**, *66*, 104187.

(126) Zhang, S.; Zhao, Y.; Shi, R.; Zhou, C.; Waterhouse, G. I. N.; Wu, L.-Z.; Tung, C.-H.; Zhang, T. Efficient Photocatalytic Nitrogen Fixation over Cu$^{δ+}$-Modified Defective ZnAl-Layered Double Hydroxide Nanosheets. *Adv. Energy Mater.* **2020**, *10*, 1901973.

(127) Tang, C.; Qiao, S.-Z. How to Explore Ambient Electro-catalytic Nitrogen Reduction Reliably and Insightfully. *Chem. Soc. Rev.* **2019**, *48*, 3166−3180.

(128) Hu, B.; Hu, M.; Seefeldt, L.; Liu, T. L. Electrochemical Dinitrogen Reduction to Ammonia by Mo$_2$N: Catalysis or Decomposition? *ACS Energy Lett.* **2019**, *4*, 1053−1054.

(129) Zhu, C. Z.; Li, H.; Fu, S. F.; Du, D.; Lin, Y. H. Highly Efficient Nonprecious Metal Catalysts Towards Oxygen Reduction Reaction Based on Three-Dimensional Porous Carbon Nanostructures. *Chem. Soc. Rev.* **2016**, *45*, 517−531.

(130) Dutta, S.; Bhaumik, A.; Wu, K. C. W. Hierarchically Porous Carbon Derived from Polymers and Biomass: Effect of Interconnected Pores on Energy Applications. *Energy Environ. Sci.* **2014**, *7*, 3574−3592.

(131) Zhao, X. X.; Sun, W. W.; Geng, D. C.; Fu, W.; Dan, J. D.; Xie, Y.; Kent, P. R. C.; Zhou, W.; Pennycook, S. J.; Loh, K. P. Edge Segregated Polymorphism in 2D Molybdenum Carbide. *Adv. Mater.* **2019**, *31*, 1808343.

(132) Kibsgaard, J.; Chen, Z. B.; Reinecke, B. N.; Jaramillo, T. F. Engineering the Surface Structure of MoS$_2$ to Preferentially Expose Active Edge Sites for Electrocatalysis. *Nat. Mater.* **2012**, *11*, 963−969.

(133) Shen, A. L.; Zou, Y. Q.; Wang, Q.; Dryfe, R. A. W.; Huang, X. B.; Dou, S.; Dai, L. M.; Wang, S. Y. Oxygen Reduction Reaction in a Droplet on Graphite: Direct Evidence That the Edge Is More Active Than the Basal Plane. *Angew. Chem., Int. Ed.* **2014**, *53*, 10804−10808.

(134) Ding, L.; Wei, Y. Y.; Li, L. B.; Zhang, T.; Wang, H. H.; Xue, J.; Ding, L. X.; Wang, S. Q.; Caro, J.; Gogotsi, Y. Mxene Molecular Sieving Membranes for Highly Efficient Gas Separation. *Nat. Commun.* **2018**, *9*, 155.

(135) Anasori, B.; Lukatskaya, M. R.; Gogotsi, Y. 2D Metal Carbides and Nitrides (Mxenes) for Energy Storage. *Nat. Rev. Mater.* **2017**, *2*, 16098.

(136) Peng, J. H.; Chen, X. Z.; Ong, W. J.; Zhao, X. J.; Li, N. Surface and Heterointerface Engineering of 2D Mxenes and Their Nano-composites: Insights into Electro- and Photocatalysis. *Chem.* **2019**, *5*, 18−50.

(137) Azofra, L. M.; Li, N.; MacFarlane, D. R.; Sun, C. H. Promising Prospects for 2D d^2-d^4 M$_3$C$_2$ Transition Metal Carbides (Mxenes) in N$_2$ Capture and Conversion into Ammonia. *Energy Environ. Sci.* **2016**, *9*, 2545−2549.

(138) Luo, Y. R.; Chen, G. F.; Ding, L.; Chen, X. Z.; Ding, L. X.; Wang, H. H. Efficient Electrocatalytic N$_2$ Fixation with Mxene under Ambient Conditions. *Joule* **2019**, *3*, 279−289.

(139) Zhang, L.; Ji, X. Q.; Ren, X.; Ma, Y. J.; Shi, X. F.; Tian, Z. Q.; Asiri, A. M.; Chen, L.; Tang, B.; Sun, X. P. Electrochemical Ammonia Synthesis Via Nitrogen Reduction Reaction on a MoS$_2$ Catalyst: Theoretical and Experimental Studies. *Adv. Mater.* **2018**, *30*, 1800191.

(140) Hao, Y. C.; Guo, Y.; Chen, L. W.; Shu, M.; Wang, X. Y.; Bu, T. A.; Gao, W. Y.; Zhang, N.; Su, X.; Feng, X.; Zhou, J. W.; Wang, B.; Hu, C. W.; Yin, A. X.; Si, R.; Zhang, Y. W.; Yan, C. H. Promoting Nitrogen Electroreduction to Ammonia with Bismuth Nanocrystals and Potassium Cations in Water. *Nat. Catal.* **2019**, *2*, 448−456.

(141) Wang, J.; Yu, L.; Hu, L.; Chen, G.; Xin, H. L.; Feng, X. F. Ambient Ammonia Synthesis Via Palladium-Catalyzed Electro-hydrogenation of Dinitrogen at Low Overpotential. *Nat. Commun.* **2018**, *9*, 1795.

(142) Chu, K.; Liu, Y. P.; Li, Y. B.; Zhang, H.; Tian, Y. Efficient Electrocatalytic N$_2$ Reduction on CoO Quantum Dots. *J. Mater. Chem. A* **2019**, *7*, 4389−4394.

(143) Chu, K.; Liu, Y. P.; Li, Y. B.; Wang, J.; Zhang, H. Electronically Coupled SnO$_2$ Quantum Dots and Graphene for Efficient Nitrogen Reduction Reaction. *ACS Appl. Mater. Interfaces* **2019**, *11*, 31806−31815.

(144) Du, R.; Jin, X. Y.; Hubner, R.; Fan, X. L.; Hu, Y.; Eychmuller, A. Engineering Self-Supported Noble Metal Foams toward Electro-catalysis and Beyond. *Adv. Energy Mater.* **2020**, *10*, 1901945.

(145) Zhang, J. W.; Kuang, Q.; Jiang, Y. Q.; Xie, Z. X. Engineering High-Energy Surfaces of Noble Metal Nanocrystals with Enhanced Catalytic Performances. *Nano Today* **2016**, *11*, 661−677.

(146) Chen, Y. J.; Ji, S. F.; Chen, C.; Peng, Q.; Wang, D. S.; Li, Y. D. Single-Atom Catalysts: Synthetic Strategies and Electrochemical Applications. *Joule* **2018**, *2*, 1242−1264.

(147) Liu, L. C.; Corma, A. Metal Catalysts for Heterogeneous Catalysis: From Single Atoms to Nanoclusters and Nanoparticles. *Chem. Rev.* **2018**, *118*, 4981−5079.

(148) Zhang, L. L.; Ren, Y. J.; Liu, W. G.; Wang, A. Q.; Zhang, T. Single-Atom Catalyst: A Rising Star for Green Synthesis of Fine Chemicals. *Natl. Sci. Rev.* **2018**, *5*, 653−672.

(149) Zhang, H. B.; Liu, G. G.; Shi, L.; Ye, J. H. Single-Atom Catalysts: Emerging Multifunctional Materials in Heterogeneous Catalysis. *Adv. Energy Mater.* **2018**, *8*, 1701343.

(150) He, Q.; Liu, D. B.; Lee, J. H.; Liu, Y. M.; Xie, Z. H.; Hwang, S.; Kattel, S.; Song, L.; Chen, J. G. G. Electrochemical Conversion of CO$_2$ to Syngas with Controllable CO/H$_2$ Ratios over Co and Ni Single-Atom Catalysts. *Angew. Chem., Int. Ed.* **2020**, *59*, 3033−3037.

(151) Chen, J. G. Electrochemical CO$_2$ Reduction Via Low-Valent Nickel Single-Atom Catalyst. *Joule* **2018**, *2*, 587−589.

(152) Yin, Y.; Shi, L.; Li, W.; Li, X.; Wu, H.; Ao, Z.; Tian, W.; Liu, S.; Wang, S.; Sun, H. Boosting Fenton-Like Reactions Via Single Atom Fe Catalysis. *Environ. Sci. Technol.* **2019**, *53*, 11391−11400.

(153) Wang, Y.; Tang, Y. J.; Zhou, K. Self-Adjusting Activity Induced by Intrinsic Reaction Intermediate in Fe-N-C Single-Atom Catalysts. *J. Am. Chem. Soc.* **2019**, *141*, 14115−14119.

(154) Zhao, W. H.; Zhang, L. F.; Luo, Q. Q.; Hu, Z. P.; Zhang, W. H.; Smith, S.; Yang, J. L. Single Mo$_1$(Cr$_1$) Atom on Nitrogen-Doped Graphene Enables Highly Selective Electroreduction of Nitrogen into Ammonia. *ACS Catal.* **2019**, *9*, 3419−3425.

(155) Choi, C.; Back, S.; Kim, N. Y.; Lim, J.; Kim, Y. H.; Jung, Y. Suppression of Hydrogen Evolution Reaction in Electrochemical N$_2$ Reduction Using Single-Atom Catalysts: A Computational Guideline. *ACS Catal.* **2018**, *8*, 7517−7525.

(156) Li, L.; Li, B. H.; Guo, Q. Y.; Li, B. Theoretical Screening of Single-Atom-Embedded MoSSe Nanosheets for Electrocatalytic N$_2$ Fixation. *J. Phys. Chem. C* **2019**, *123*, 14501−14507.

(157) Yang, T.; Song, T. T.; Zhou, J.; Wang, S.; Chi, D.; Shen, L.; Yang, M.; Feng, Y. P. High-Throughput Screening of Transition Metal Single Atom Catalysts Anchored on Molybdenum Disulfide for Nitrogen Fixation. *Nano Energy* **2020**, *68*, 104304.

(158) Zhao, J. X.; Chen, Z. F. Single Mo Atom Supported on Defective Boron Nitride Monolayer as an Efficient Electrocatalyst for Nitrogen Fixation: A Computational Study. *J. Am. Chem. Soc.* **2017**, *139*, 12480−12487.

(159) Chen, Z.; Zhao, J.; Cabrera, C. R.; Chen, Z. Computational Screening of Efficient Single-Atom Catalysts Based on Graphitic Carbon Nitride (g-C$_3$N$_4$) for Nitrogen Electroreduction. *Small Methods* **2019**, *3*, 1800368.

(160) Liu, X.; Jiao, Y.; Zheng, Y.; Jaroniec, M.; Qiao, S. Z. Building up a Picture of the Electrocatalytic Nitrogen Reduction Activity of Transition Metal Single-Atom Catalysts. *J. Am. Chem. Soc.* **2019**, *141*, 9664−9672.

(161) Geng, Z. G.; Liu, Y.; Kong, X. D.; Li, P.; Li, K.; Liu, Z. Y.; Du, J. J.; Shu, M.; Si, R.; Zeng, J. Achieving a Record-High Yield Rate of 120.9 μg_{NH_3} mg$_{cat.}^{-1}$ h^{-1} for N$_2$ Electrochemical Reduction over Ru Single-Atom Catalysts. *Adv. Mater.* **2018**, *30*, 1803498.

(162) Tao, H. C.; Choi, C.; Ding, L. X.; Jiang, Z.; Han, Z. S.; Jia, M. W.; Fan, Q.; Gao, Y. N.; Wang, H. H.; Robertson, A. W.; Hong, S.; Jung, Y. S.; Liu, S. Z.; Sun, Z. Y. Nitrogen Fixation by Ru Single-Atom Electrocatalytic Reduction. *Chem.* **2019**, *5*, 204−214.

(163) Qin, Q.; Heil, T.; Antonietti, M.; Oschatz, M. Single-Site Gold Catalysts on Hierarchical N-Doped Porous Noble Carbon for Enhanced Electrochemical Reduction of Nitrogen. *Small Methods* **2018**, *2*, 1800202.

(164) Wang, X. Q.; Wang, W. Y.; Qiao, M.; Wu, G.; Chen, W. X.; Yuan, T. W.; Xu, Q.; Chen, M.; Zhang, Y.; Wang, X.; Wang, J.; Ge, J. J.; Hong, X.; Li, Y. F.; Wu, Y.; Li, Y. D. Atomically Dispersed Au$_1$ Catalyst Towards Efficient Electrochemical Synthesis of Ammonia. *Sci. Bull.* **2018**, *63*, 1246−1253.

(165) Han, L. L.; Liu, X. J.; Chen, J. P.; Lin, R. Q.; Liu, H. X.; Lu, F.; Bak, S.; Liang, Z. X.; Zhao, S. Z.; Stavitski, E.; Luo, J.; Adzic, R. R.; Xin, H. L. L. Atomically Dispersed Molybdenum Catalysts for Efficient Ambient Nitrogen Fixation. *Angew. Chem., Int. Ed.* **2019**, *58*, 2321−2325.

(166) Guo, X. W.; Chen, S. M.; Wang, H. J.; Zhang, Z. M.; Lin, H.; Song, L.; Lu, T. B. Single-Atom Molybdenum Immobilized on Photoactive Carbon Nitride as Efficient Photocatalysts for Ambient Nitrogen Fixation in Pure Water. *J. Mater. Chem. A* **2019**, *7*, 19831−19837.

(167) Wang, Y.; Gao, W.; Li, K.; Zheng, Y.; Xie, Z.; Na, W.; Chen, J. G.; Wang, H. Strong Evidence of the Role of H$_2$O in Affecting Methanol Selectivity from CO$_2$ Hydrogenation over Cu-ZnO-ZrO$_2$. *Chem.* **2020**, *6*, 419−430.

(168) Li, K. Z.; Chen, J. G. G. CO$_2$ Hydrogenation to Methanol over ZrO$_2$-Containing Catalysts: Insights into ZrO$_2$ Induced Synergy. *ACS Catal.* **2019**, *9*, 7840−7861.

(169) Wang, D. B.; Azofra, L. M.; Harb, M.; Cavallo, L.; Zhang, X. Y.; Suryanto, B. H. R.; MacFarlane, D. R. Energy-Efficient Nitrogen Reduction to Ammonia at Low Overpotential in Aqueous Electrolyte under Ambient Conditions. *ChemSusChem* **2018**, *11*, 3416−3422.

(170) Shi, M. M.; Bao, D.; Wulan, B. R.; Li, Y. H.; Zhang, Y. F.; Yan, J. M.; Jiang, Q. Au Sub-Nanoclusters on TiO$_2$ toward Highly Efficient and Selective Electrocatalyst for N$_2$ Conversion to NH$_3$ at Ambient Conditions. *Adv. Mater.* **2017**, *29*, 1606550.

(171) Zang, W. J.; Yang, T.; Zou, H. Y.; Xi, S. B.; Zhang, H.; Liu, X. M.; Kou, Z. K.; Du, Y. H.; Feng, Y. P.; Shen, L.; Duan, L. L.; Wang, J.; Pennycook, S. J. Copper Single Atoms Anchored in Porous Nitrogen-Doped Carbon as Efficient pH-Universal Catalysts for the Nitrogen Reduction Reaction. *ACS Catal.* **2019**, *9*, 10166−10173.

(172) Huang, P. C.; Liu, W.; He, Z. H.; Xiao, C.; Yao, T.; Zou, Y. M.; Wang, C. M.; Qi, Z. M.; Tong, W.; Pan, B. C.; Wei, S. Q.; Xie, Y. Single Atom Accelerates Ammonia Photosynthesis. *Sci. China: Chem.* **2018**, *61*, 1187−1196.

(173) Wang, M. F.; Liu, S. S.; Qian, T.; Liu, J.; Zhou, J. Q.; Ji, H. Q.; Xiong, J.; Zhong, J.; Yan, C. L. Over 56.55% Faradaic Efficiency of Ambient Ammonia Synthesis Enabled by Positively Shifting the Reaction Potential. *Nat. Commun.* **2019**, *10*, 341.

(174) Li, X. F.; Li, Q. K.; Cheng, J.; Liu, L. L.; Yan, Q.; Wu, Y. C.; Zhang, X. H.; Wang, Z. Y.; Qiu, Q.; Luo, Y. Conversion of Dinitrogen

to Ammonia by FeN$_3$-Embedded Graphene. *J. Am. Chem. Soc.* **2016**, *138*, 8706−8709.

(175) Wang, Y.; Cui, X. Q.; Zhao, J. X.; Jia, G. R.; Gu, L.; Zhang, Q. H.; Meng, L. K.; Shi, Z.; Zheng, L. R.; Wang, C. Y.; Zhang, Z. W.; Zheng, W. T. Rational Design of Fe-N/C Hybrid for Enhanced Nitrogen Reduction Electrocatalysis under Ambient Conditions in Aqueous Solution. *ACS Catal.* **2019**, *9*, 336−344.

(176) Lü, F.; Zhao, S.; Guo, R.; He, J.; Peng, X.; Bao, H.; Fu, J.; Han, L.; Qi, G.; Luo, J.; Tang, X.; Liu, X. Nitrogen-Coordinated Single Fe Sites for Efficient Electrocatalytic N$_2$ Fixation in Neutral Media. *Nano Energy* **2019**, *61*, 420−427.

(177) He, C.; Wu, Z.-Y.; Zhao, L.; Ming, M.; Zhang, Y.; Yi, Y.; Hu, J.-S. Identification of FeN$_4$ as an Efficient Active Site for Electrochemical N$_2$ Reduction. *ACS Catal.* **2019**, *9*, 7311−7317.

(178) Wang, A. Q.; Li, J.; Zhang, T. Heterogeneous Single-Atom Catalysis. *Nat. Rev. Chem.* **2018**, *2*, 65−81.

(179) Li, J.; Zheng, G. F. One-Dimensional Earth-Abundant Nanomaterials for Water-Splitting Electrocatalysts. *Adv. Sci.* **2017**, *4*, 1600380.

(180) Han, J. R.; Liu, Z. C.; Ma, Y. J.; Cui, G. W.; Xie, F. Y.; Wang, F. X.; Wu, Y. P.; Gao, S. Y.; Xu, Y. H.; Sun, X. P. Ambient N$_2$ Fixation to NH$_3$ at Ambient Conditions: Using Nb$_2$O$_5$ Nanofiber as a High-Performance Electrocatalyst. *Nano Energy* **2018**, *52*, 264−270.

(181) Xu, K.; Cheng, H.; Lv, H. F.; Wang, J. Y.; Liu, L. Q.; Liu, S.; Wu, X. J.; Chu, W. S.; Wu, C. Z.; Xie, Y. Controllable Surface Reorganization Engineering on Cobalt Phosphide Nanowire Arrays for Efficient Alkaline Hydrogen Evolution Reaction. *Adv. Mater.* **2018**, *30*, 1703322.

(182) Jiang, P.; Liu, Q.; Liang, Y. H.; Tian, J. Q.; Asiri, A. M.; Sun, X. P. A Cost-Effective 3D Hydrogen Evolution Cathode with High Catalytic Activity: FeP Nanowire Array as the Active Phase. *Angew. Chem., Int. Ed.* **2014**, *53*, 12855−12859.

(183) Suryanto, B. H. R.; Kang, C. S. M.; Wang, D. B.; Xiao, C. L.; Zhou, F. L.; Azofra, L. M.; Cavallo, L.; Zhang, X. Y.; MacFarlane, D. R. Rational Electrode-Electrolyte Design for Efficient Ammonia Electrosynthesis under Ambient Conditions. *ACS Energy Lett.* **2018**, *3*, 1219−1224.

(184) Tan, C. L.; Cao, X. H.; Wu, X. J.; He, Q. Y.; Yang, J.; Zhang, X.; Chen, J. Z.; Zhao, W.; Han, S. K.; Nam, G. H.; Sindoro, M.; Zhang, H. Recent Advances in Ultrathin Two-Dimensional Nanomaterials. *Chem. Rev.* **2017**, *117*, 6225−6331.

(185) Deng, D. H.; Novoselov, K. S.; Fu, Q.; Zheng, N. F.; Tian, Z. Q.; Bao, X. H. Catalysis with Two-Dimensional Materials and Their Heterostructures. *Nat. Nanotechnol.* **2016**, *11*, 218−230.

(186) Liu, H. M.; Han, S. H.; Zhao, Y.; Zhu, Y. Y.; Tian, X. L.; Zeng, J. H.; Jiang, J. X.; Xia, B. Y.; Chen, Y. Surfactant-Free Atomically Ultrathin Rhodium Nanosheet Nanoassemblies for Efficient Nitrogen Electroreduction. *J. Mater. Chem. A* **2018**, *6*, 3211−3217.

(187) Zhang, X. X.; Wu, T. W.; Wang, H. B.; Zhao, R. B.; Chen, H. Y.; Wang, T.; Wei, P. P.; Luo, Y. L.; Zhang, Y. N.; Sun, X. P. Boron Nanosheet: An Elemental Two-Dimensional (2D) Material for Ambient Electrocatalytic N$_2$-to-NH$_3$ Fixation in Neutral Media. *ACS Catal.* **2019**, *9*, 4609−4615.

(188) Qiu, W. B.; Xie, X. Y.; Qiu, J. D.; Fang, W. H.; Liang, R. P.; Ren, X.; Ji, X. Q.; Cui, G. W.; Asiri, A. M.; Cui, G. L.; Tang, B.; Sun, X. P. High-Performance Artificial Nitrogen Fixation at Ambient Conditions Using a Metal-Free Electrocatalyst. *Nat. Commun.* **2018**, *9*, 3485.

(189) Han, J. R.; Ji, X. Q.; Ren, X.; Cui, G. W.; Li, L.; Xie, F. Y.; Wang, H.; Li, B. H.; Sun, X. P. MoO$_3$ Nanosheets for Efficient Electrocatalytic N$_2$ Fixation to NH$_3$. *J. Mater. Chem. A* **2018**, *6*, 12974−12977.

(190) Li, L. Q.; Tang, C.; Xia, B. Q.; Jin, H. Y.; Zheng, Y.; Qiao, S. Z. Two-Dimensional Mosaic Bismuth Nanosheets for Highly Selective Ambient Electrocatalytic Nitrogen Reduction. *ACS Catal.* **2019**, *9*, 2902−2908.

(191) Zhang, Y.; Du, H.; Ma, Y.; Ji, L.; Guo, H.; Tian, Z.; Chen, H.; Huang, H.; Cui, G.; Asiri, A. M.; Qu, F.; Chen, L.; Sun, X. Hexagonal

Boron Nitride Nanosheet for Effective Ambient N_2 Fixation to NH_3. *Nano Res.* **2019**, *12*, 919−924.

(192) Zhang, L. L.; Ding, L. X.; Chen, G. F.; Yang, X. F.; Wang, H. H. Ammonia Synthesis under Ambient Conditions: Selective Electroreduction of Dinitrogen to Ammonia on Black Phosphorus Nanosheets. *Angew. Chem., Int. Ed.* **2019**, *58*, 2612−2616.

(193) Hou, T. T.; Guo, R. H.; Chen, L. L.; Xie, Y. C. Z.; Guo, J. S.; Zhang, W. H.; Zheng, X. S.; Zhu, W. K.; Tan, X. P.; Wang, L. B. Atomic-Level Insights in Tuning Defective Structures for Nitrogen Photofixation over Amorphous SmOCl Nanosheets. *Nano Energy* **2019**, *65*, 104003.

(194) Xue, X. L.; Chen, R. P.; Chen, H. W.; Hu, Y.; Ding, Q. Q.; Liu, Z. T.; Ma, L. B.; Zhu, G. Y.; Zhang, W. J.; Yu, Q.; Liu, J.; Ma, J.; Jin, Z. Oxygen Vacancy Engineering Promoted Photocatalytic Ammonia Synthesis on Ultrathin Two-Dimensional Bismuth Oxybromide Nanosheets. *Nano Lett.* **2018**, *18*, 7372−7377.

(195) Di, J.; Xia, J. X.; Chisholm, M. F.; Zhong, J.; Chen, C.; Cao, X. Z.; Dong, F.; Chi, Z.; Chen, H. L.; Weng, Y. X.; Xiong, J.; Yang, S. Z.; Li, H. M.; Liu, Z.; Dai, S. Defect-Tailoring Mediated Electron-Hole Separation in Single-Unit-Cell Bi_3O_4Br Nanosheets for Boosting Photocatalytic Hydrogen Evolution and Nitrogen Fixation. *Adv. Mater.* **2019**, *31*, 1807576.

(196) Yin, Y.; Wu, H.; Shi, L.; Zhang, J.; Xu, X.; Zhang, H.; Wang, S.; Sillanpää, M.; Sun, H. Quasi Single Cobalt Sites in Nanopores for Superior Catalytic Oxidation of Organic Pollutants. *Environ. Sci.: Nano* **2018**, *5*, 2842−2852.

(197) Lu, Q.; Hutchings, G. S.; Yu, W. T.; Zhou, Y.; Forest, R. V.; Tao, R. Z.; Rosen, J.; Yonemoto, B. T.; Cao, Z. Y.; Zheng, H. M.; Xiao, J. Q.; Jiao, F.; Chen, J. G. G. Highly Porous Non-Precious Bimetallic Electrocatalysts for Efficient Hydrogen Evolution. *Nat. Commun.* **2015**, *6*, 6567.

(198) Nazemi, M.; El-Sayed, M. A. Plasmon-Enhanced Photo-(Electro)Chemical Nitrogen Fixation under Ambient Conditions Using Visible Light Responsive Hybrid Hollow $Au-Ag_2O$ Nanocages. *Nano Energy* **2019**, *63*, 103886.

(199) Nazemi, M.; Panikkanvalappil, S. R.; El-Sayed, M. A. Enhancing the Rate of Electrochemical Nitrogen Reduction Reaction for Ammonia Synthesis under Ambient Conditions Using Hollow Gold Nanocages. *Nano Energy* **2018**, *49*, 316−323.

(200) Nazemi, M.; El-Sayed, M. A. Electrochemical Synthesis of Ammonia from N_2 and H_2O under Ambient Conditions Using Pore-Size-Controlled Hollow Gold Nanocatalysts with Tunable Plasmonic Properties. *J. Phys. Chem. Lett.* **2018**, *9*, 5160−5166.

(201) Zhang, Y.; Qiu, W. B.; Ma, Y. J.; Luo, Y. L.; Tian, Z. Q.; Cui, G. W.; Xie, F. Y.; Chen, L.; Li, T. S.; Sun, X. P. High-Performance Electrohydrogenation of N_2 to NH_3 Catalyzed by Multishelled Hollow Cr_2O_3 Microspheres under Ambient Conditions. *ACS Catal.* **2018**, *8*, 8540−8544.

(202) Guo, W. H.; Liang, Z. B.; Zhao, J. L.; Zhu, B. J.; Cai, K. T.; Zou, R. Q.; Xu, Q. Hierarchical Cobalt Phosphide Hollow Nanocages toward Electrocatalytic Ammonia Synthesis under Ambient Pressure and Room Temperature. *Small Methods* **2018**, *2*, 1800204.

(203) Wang, X. J.; Feng, J.; Bai, Y. C.; Zhang, Q.; Yin, Y. D. Synthesis, Properties, and Applications of Hollow Micro-/Nanostructures. *Chem. Rev.* **2016**, *116*, 10983−11060.

(204) Zhang, Q.; Wang, W. S.; Goebl, J.; Yin, Y. D. Self-Templated Synthesis of Hollow Nanostructures. *Nano Today* **2009**, *4*, 494−507.

(205) Zhou, K. B.; Li, Y. D. Catalysis Based on Nanocrystals with Well-Defined Facets. *Angew. Chem., Int. Ed.* **2012**, *51*, 602−613.

(206) Yang, H. G.; Sun, C. H.; Qiao, S. Z.; Zou, J.; Liu, G.; Smith, S. C.; Cheng, H. M.; Lu, G. Q. Anatase TiO_2 Single Crystals with a Large Percentage of Reactive Facets. *Nature* **2008**, *453*, 638−641.

(207) Jiang, J.; Zhao, K.; Xiao, X. Y.; Zhang, L. Z. Synthesis and Facet-Dependent Photoreactivity of BiOCl Single-Crystalline Nanosheets. *J. Am. Chem. Soc.* **2012**, *134*, 4473−4476.

(208) Huang, X. Q.; Zhao, Z. P.; Fan, J. M.; Tan, Y. M.; Zheng, N. F. Amine-Assisted Synthesis of Concave Polyhedral Platinum Nanocrystals Having {411} High-Index Facets. *J. Am. Chem. Soc.* **2011**, *133*, 4718−4721.

(209) Zhu, W.; Kattel, S.; Jiao, F.; Chen, J. G. Shape-Controlled CO_2 Electrochemical Reduction on Nanosized Pd Hydride Cubes and Octahedra. *Adv. Energy Mater.* **2019**, *9*, 1802840.

(210) Skulason, E.; Bligaard, T.; Gudmundsdottir, S.; Studt, F.; Rossmeisl, J.; Abild-Pedersen, F.; Vegge, T.; Jonsson, H.; Norskov, J. K. A Theoretical Evaluation of Possible Transition Metal Electro-Catalysts for N_2 Reduction. *Phys. Chem. Chem. Phys.* **2012**, *14*, 1235−1245.

(211) Montoya, J. H.; Tsai, C.; Vojvodic, A.; Norskov, J. K. The Challenge of Electrochemical Ammonia Synthesis: A New Perspective on the Role of Nitrogen Scaling Relations. *ChemSusChem* **2015**, *8*, 2180−2186.

(212) Yang, D. S.; Chen, T.; Wang, Z. J. Electrochemical Reduction of Aqueous Nitrogen (N_2) at a Low Overpotential on (110)-Oriented Mo Nanofilm. *J. Mater. Chem. A* **2017**, *5*, 18967−18971.

(213) Bao, D.; Zhang, Q.; Meng, F. L.; Zhong, H. X.; Shi, M. M.; Zhang, Y.; Yan, J. M.; Jiang, Q.; Zhang, X. B. Electrochemical Reduction of N_2 under Ambient Conditions for Artificial N_2 Fixation and Renewable Energy Storage Using N_2/NH_3 Cycle. *Adv. Mater.* **2017**, *29*, 1604799.

(214) Bai, Y.; Ye, L. Q.; Chen, T.; Wang, L.; Shi, X.; Zhang, X.; Chen, D. Facet-Dependent Photocatalytic N_2 Fixation of Bismuth-Rich Bi_5O_7I Nanosheets. *ACS Appl. Mater. Interfaces* **2016**, *8*, 27661−27668.

(215) Guan, M. L.; Xiao, C.; Zhang, J.; Fan, S. J.; An, R.; Cheng, Q. M.; Xie, J. F.; Zhou, M.; Ye, B. J.; Xie, Y. Vacancy Associates Promoting Solar-Driven Photocatalytic Activity of Ultrathin Bismuth Oxychloride Nanosheets. *J. Am. Chem. Soc.* **2013**, *135*, 10411−10417.

(216) Mi, Y.; Wen, L. Y.; Wang, Z. J.; Cao, D. W.; Xu, R.; Fang, Y. G.; Zhou, Y. L.; Lei, Y. Fe(III) Modified BiOCl Ultrathin Nanosheet Towards High-Efficient Visible-Light Photocatalyst. *Nano Energy* **2016**, *30*, 109−117.

(217) Smith, R. D. L.; Prevot, M. S.; Fagan, R. D.; Zhang, Z. P.; Sedach, P. A.; Siu, M. K. J.; Trudel, S.; Berlinguette, C. P. Photochemical Route for Accessing Amorphous Metal Oxide Materials for Water Oxidation Catalysis. *Science* **2013**, *340*, 60−63.

(218) Masa, J.; Weide, P.; Peeters, D.; Sinev, I.; Xia, W.; Sun, Z. Y.; Somsen, C.; Muhler, M.; Schuhmann, W. Amorphous Cobalt Boride (Co_2B) as a Highly Efficient Nonprecious Catalyst for Electrochemical Water Splitting: Oxygen and Hydrogen Evolution. *Adv. Energy Mater.* **2016**, *6*, 1502313.

(219) Tran, P. D.; Tran, T. V.; Orio, M.; Torelli, S.; Truong, Q. D.; Nayuki, K.; Sasaki, Y.; Chiam, S. Y.; Yi, R.; Honma, I.; Barber, J.; Artero, V. Coordination Polymer Structure and Revisited Hydrogen Evolution Catalytic Mechanism for Amorphous Molybdenum Sulfide. *Nat. Mater.* **2016**, *15*, 640−646.

(220) Li, S. J.; Bao, D.; Shi, M. M.; Wulan, B. R.; Yan, J. M.; Jiang, Q. Amorphizing of Au Nanoparticles by CeO_x-RGO Hybrid Support Towards Highly Efficient Electrocatalyst for N_2 Reduction under Ambient Conditions. *Adv. Mater.* **2017**, *29*, 1700001.

(221) Shi, M. M.; Bao, D.; Li, S. J.; Wulan, B. R.; Yan, J. M.; Jiang, Q. Anchoring PdCu Amorphous Nanocluster on Graphene for Electrochemical Reduction of N_2 to NH_3 under Ambient Conditions in Aqueous Solution. *Adv. Energy Mater.* **2018**, *8*, 1800124.

(222) Pang, F. J.; Wang, Z. F.; Zhang, K.; He, J.; Zhang, W. Q.; Guo, C. X.; Ding, Y. Bimodal Nanoporous Pd_3Cu_1 Alloy with Restrained Hydrogen Evolution for Stable and High Yield Electrochemical Nitrogen Reduction. *Nano Energy* **2019**, *58*, 834−841.

(223) Lv, C. D.; Yan, C. S.; Chen, G.; Ding, Y.; Sun, J. X.; Zhou, Y. S.; Yu, G. H. An Amorphous Noble-Metal-Free Electrocatalyst That Enables Nitrogen Fixation under Ambient Conditions. *Angew. Chem., Int. Ed.* **2018**, *57*, 6073−6076.

(224) Li, C. C.; Wang, T.; Zhao, Z. J.; Yang, W. M.; Li, J. F.; Li, A.; Yang, Z. L.; Ozin, G. A.; Gong, J. L. Promoted Fixation of Molecular Nitrogen with Surface Oxygen Vacancies on Plasmon-Enhanced TiO_2 Photoelectrodes. *Angew. Chem., Int. Ed.* **2018**, *57*, 5278−5282.

(225) Marichy, C.; Bechelany, M.; Pinna, N. Atomic Layer Deposition of Nanostructured Materials for Energy and Environmental Applications. *Adv. Mater.* **2012**, *24*, 1017−1032.

(226) Lu, J. L.; Fu, B. S.; Kung, M. C.; Xiao, G. M.; Elam, J. W.; Kung, H. H.; Stair, P. C. Coking- and Sintering-Resistant Palladium Catalysts Achieved through Atomic Layer Deposition. *Science* **2012**, *335*, 1205−1208.

(227) George, S. M. Atomic Layer Deposition: An Overview. *Chem. Rev.* **2010**, *110*, 111−131.

(228) Dinh, C. T.; Burdyny, T.; Kibria, M. G.; Seifitokaldani, A.; Gabardo, C. M.; Garcia de Arquer, F. P.; Kiani, A.; Edwards, J. P.; De Luna, P.; Bushuyev, O. S.; Zou, C. Q.; Quintero-Bermudez, R.; Pang, Y. J.; Sinton, D.; Sargent, E. H. CO_2 Electroreduction to Ethylene Via Hydroxide-Mediated Copper Catalysis at an Abrupt Interface. *Science* **2018**, *360*, 783−787.

(229) Lv, K. L.; Teng, C.; Shi, M. H.; Yuan, Y.; Zhu, Y.; Wang, J. R.; Kong, Z.; Lu, X. Y.; Zhu, Y. Hydrophobic and Electronic Properties of the E-MoS_2 Nanosheets Induced by FAS for the CO_2 Electroreduction to Syngas with a Wide Range of CO/H_2 Ratios. *Adv. Funct. Mater.* **2018**, *28*, 1802339.

(230) Lu, Z. Y.; Xu, W. W.; Ma, J.; Li, Y. J.; Sun, X. M.; Jiang, L. Superaerophilic Carbon-Nanotube-Array Electrode for High-Performance Oxygen Reduction Reaction. *Adv. Mater.* **2016**, *28*, 7155−7161.

(231) Singh, A. R.; Rohr, B. A.; Schwalbe, J. A.; Cargnello, M.; Chan, K.; Jaramillo, T. F.; Chorkendorff, I.; Nørskov, J. K. Electrochemical Ammonia Synthesis—the Selectivity Challenge. *ACS Catal.* **2017**, *7*, 706−709.

(232) Lee, H. K.; Koh, C. S. L.; Lee, Y. H.; Liu, C.; Phang, I. Y.; Han, X. M.; Tsung, C. K.; Ling, X. Y. Favoring the Unfavored: Selective Electrochemical Nitrogen Fixation Using a Reticular Chemistry Approach. *Sci. Adv.* **2018**, *4*, eaar3208.

(233) Zheng, J. Y.; Lyu, Y. H.; Qiao, M.; Wang, R. L.; Zhou, Y. Y.; Li, H.; Chen, C.; Li, Y. F.; Zhou, H. J.; Jiang, S. P.; Wang, S. Y. Photoelectrochemical Synthesis of Ammonia on the Aerophilic-Hydrophilic Heterostructure with 37.8% Efficiency. *Chem.* **2019**, *5*, 617−633.

(234) Gottle, A. J.; Koper, M. T. M. Proton-Coupled Electron Transfer in the Electrocatalysis of CO_2 Reduction: Prediction of Sequential vs. Concerted Pathways Using DFT. *Chem. Sci.* **2017**, *8*, 458−465.

(235) Ling, C. Y.; Ouyang, Y. X.; Li, Q.; Bai, X. W.; Mao, X.; Du, A. J.; Wang, J. L. A General Two-Step Strategy-Based High-Throughput Screening of Single Atom Catalysts for Nitrogen Fixation. *Small Methods* **2019**, *3*, 1800376.

(236) Wuttig, A.; Yaguchi, M.; Motobayashi, K.; Osawa, M.; Surendranath, Y. Inhibited Proton Transfer Enhances Au-Catalyzed CO_2-to-Fuels Selectivity. *Proc. Natl. Acad. Sci. U. S. A.* **2016**, *113*, E4585−E4593.

(237) Jenness, G. R.; Wan, W. M.; Chen, J. G. G.; Vlachos, D. G. Reaction Pathways and Intermediates in Selective Ring Opening of Biomass-Derived Heterocyclic Compounds by Iridium. *ACS Catal.* **2016**, *6*, 7002−7009.

(238) Yao, Y.; Zhu, S. Q.; Wang, H. J.; Li, H.; Shao, M. H. A Spectroscopic Study on the Nitrogen Electrochemical Reduction Reaction on Gold and Platinum Surfaces. *J. Am. Chem. Soc.* **2018**, *140*, 1496−1501.

(239) Yao, Y.; Wang, H. J.; Yuan, X. Z.; Li, H.; Shao, M. H. Electrochemical Nitrogen Reduction Reaction on Ruthenium. *ACS Energy Lett.* **2019**, *4*, 1336−1341.

(240) Lee, J. H.; Kattel, S.; Jiang, Z.; Xie, Z.; Yao, S.; Tackett, B. M.; Xu, W.; Marinkovic, N. S.; Chen, J. G. Tuning the Activity and Selectivity of Electroreduction of CO_2 to Synthesis Gas Using Bimetallic Catalysts. *Nat. Commun.* **2019**, *10*, 3724.

(241) Yan, B. H.; Yao, S. Y.; Kattel, S.; Wu, Q. Y.; Xie, Z. H.; Gomez, E.; Liu, P.; Su, D.; Chen, J. G. G. Active Sites for Tandem Reactions of CO_2 Reduction and Ethane Dehydrogenation. *Proc. Natl. Acad. Sci. U. S. A.* **2018**, *115*, 8278−8283.

(242) Liu, S.; Wang, M.; Qian, T.; Ji, H.; Liu, J.; Yan, C. Facilitating Nitrogen Accessibility to Boron-Rich Covalent Organic Frameworks Via Electrochemical Excitation for Efficient Nitrogen Fixation. *Nat. Commun.* **2019**, *10*, 3898.

(243) Chen, G. F.; Ren, S. Y.; Zhang, L. L.; Cheng, H.; Luo, Y. R.; Zhu, K. H.; Ding, L. X.; Wang, H. H. Advances in Electrocatalytic N_2 Reduction-Strategies to Tackle the Selectivity Challenge. *Small Methods* **2019**, *3*, 1800337.

(244) Zhao, Y. X.; Shi, R.; Bian, X. A. N.; Zhou, C.; Zhao, Y. F.; Zhang, S.; Wu, F.; Waterhouse, G. I. N.; Wu, L. Z.; Tung, C. H.; Zhang, T. R. Ammonia Detection Methods in Photocatalytic and Electrocatalytic Experiments: How to Improve the Reliability of NH_3 Production Rates? *Adv. Sci.* **2019**, *6*, 1802109.

(245) Andersen, S. Z.; Čolić, V.; Yang, S.; Schwalbe, J. A.; Nielander, A. C.; McEnaney, J. M.; Enemark-Rasmussen, K.; Baker, J. G.; Singh, A. R.; Rohr, B. A.; Statt, M. J.; Blair, S. J.; Mezzavilla, S.; Kibsgaard, J.; Vesborg, P. C. K.; Cargnello, M.; Bent, S. F.; Jaramillo, T. F.; Stephens, I. E. L.; Nørskov, J. K.; Chorkendorff, I. A Rigorous Electrochemical Ammonia Synthesis Protocol with Quantitative Isotope Measurements. *Nature* **2019**, *570*, 504−508.

(246) Nielander, A. C.; McEnaney, J. M.; Schwalbe, J. A.; Baker, J. G.; Blair, S. J.; Wang, L.; Pelton, J. G.; Andersen, S. Z.; Enemark-Rasmussen, K.; Colic, V.; Yang, S.; Bent, S. F.; Cargnello, M.; Kibsgaard, J.; Vesborg, P. C. K.; Chorkendorff, I.; Jaramillo, T. F. A Versatile Method for Ammonia Detection in a Range of Relevant Electrolytes Via Direct Nuclear Magnetic Resonance Techniques. *ACS Catal.* **2019**, *9*, 5797−5802.

(247) Chen, J. G.; Jones, C. W.; Linic, S.; Stamenkovic, V. R. Best Practices in Pursuit of Topics in Heterogeneous Electrocatalysis. *ACS Catal.* **2017**, *7*, 6392−6393.